

Measurement of Local Gravity using Atom Interferometry

Development of Subcomponents

Diplomarbeit in Physik

Technische Universität Berlin
Fakultät II - Institut für Optik und Atomare Physik

carried out at
Humboldt-Universität zu Berlin
Department of Physics
Quantum Optics and Metrology

Christian Freier

August 2010

Supervisor: Prof. Dr. Möller (Technische Universität Berlin)
External Supervisor: Prof. A. Peters, PhD (Humboldt-Universität zu Berlin und
Ferdinand-Braun-Institut)

Declaration

I hereby truthfully and solemnly declare that I have carried out this thesis entirely myself and without the help of any third party and that all literal quotations and other authors' ideas have been completely accounted for.

Berlin, 9th of August 2010

Christian Freier

Die selbständige und eigenständige Anfertigung versichere ich an Eides statt.

Berlin, den 9. August 2010

Christian Freier

Summary

A method to measure local gravity using an atomic fountain gravimeter is presented. The system enables high sensitivity gravity measurements and combines them with a mobile setup which allows measurements to be taken at geographically interesting sites. This work is concerned with the development and design of interferometer subcomponents and a measurement of tidal gravity variations.

The accuracy of the existing setup has been improved significantly from 3×10^{-6} g to 5×10^{-8} g per single measurement with the implementation of an active vibration isolation system. Due to the increased sensitivity of the instruments, measurements of tidal gravity variations are now possible. These measurements have been compared to tidal predictions, which have been carried out using advanced geophysical models, over a period of six days.

Additionally, a new subsystem for more accurate detection has been designed which measures the atomic states after the interferometer sequence .

Deutsche Zusammenfassung

Ein Experiment zur Messung der lokalen Erdbeschleunigung g mittels Atominterferometrie wird vorgestellt. Am Anfang der Arbeit (Kapitel 2) werden das Experiment und die theoretischen Grundlagen des Experimentes erläutert und ein intuitives Verständnis des Messprozesses vermittelt.

Im Schwerpunkt dieser Diplomarbeit stehen verschiedene Subsysteme des Atominterferometers welche hinzugefügt und verbessert wurden. Insbesondere wurde eine aktive Schwingungsisolationsplattform entwickelt um eine Schlüsselkomponente des Aufbaus von mechanischen Vibrationen zu entkoppeln. Diese Vibrationen limitierten zuvor die Auflösung des Atominterferometers. Das Messrauschen des Interferometers aufgrund von Vibrationen vor und nach Implementierung der Schwingungsisolationsplattform wird theoretisch untersucht. Die Resultate der theoretischen Betrachtung werden daraufhin mit der gemessenen Empfindlichkeit verglichen.

Die Empfindlichkeit der g -Messung konnte durch die Implementierung des aktiven Schwingungsisolators von 3×10^{-6} g auf 5×10^{-8} g pro Einzelmessung gesteigert werden. Durch die gesteigerte Auflösung ist es nun möglich durch Gezeitenkräfte verursachte Variationen der Schwerkraft zu messen. Die gemessenen Variationen werden vorgestellt und mit einer theoretischen Gezeitenvorhersage verglichen. Das zugrundeliegende Gezeitenmodell basiert auf fortgeschrittenen geophysikalischen Modellen und wird ebenfalls kurz erläutert.

Das nächste Kapitel (Kapitel 3) stellt die Arbeitsweise und die theoretischen Grundlagen der Schwingungsisolierung ausführlich dar. Dies beinhaltet die Grundlagen der passiven Schwingungsisolierung und eine Behandlung der Regelschleife, welche zur Implementierung eines aktiven Systems führte und die Leistungsfähigkeit des Isolators stark steigerte. Am Ende des dritten Kapitels wird die Performance des aktiven Isolators anhand von Messungen charakterisiert und diskutiert.

Das vierte Kapitel stellt die Entwicklung eines neuartigen Detektionssystems vor. Das Detektionssystem misst die atomaren Zustände der Atome nach der Interferometersequenz, aus welcher unmittelbar die Phase des Interferometers ermittelt wird. Die theoretischen Grundlagen der Detektionsmessung werden im Kapitel vorgestellt. Das entwickelte System basiert auf einem rauscharmen Detektor aus [Gre09]. Durch diesen Detektor kann die Empfindlichkeit der Detektion potentiell bis an die Grenze des quantenmechanischen Projektionsrauschens gesteigert werden. Dies kann in Zukunft die Auflösung des Interferometers verbessern und die Analyse von systematischen Fehlern in Gravitationsmessungen vereinfachen.

Contents

Summary	V
Deutsche Zusammenfassung	VII
1 Introduction	1
2 Atomic Fountain Gravimeter using Atom Interferometry	5
2.1 Theory	5
2.1.1 Stimulated Raman Transitions	5
2.1.2 Interferometer Sequence	6
2.1.3 Summary	9
2.2 Experimental Setup	10
2.3 Vibration Noise in the Atom Interferometer	13
2.4 Prediction of tidal Gravity Variations	17
2.5 Measurement of Tidal Gravity Variations	20
2.6 Conclusion and Outlook	21
3 Very Low Frequency Vibration Isolation	23
3.1 Passive Vibration Isolator	23
3.1.1 Absolute Transmissibility	24
3.1.2 Tuning the Resonance Frequency with Negative Stiffness Elements .	27
3.1.3 Isolator Tilt Motions	28
3.1.4 Horizontal Vibration Isolator	29
3.2 Active Isolation Theory	30
3.2.1 Open-Loop and Closed-Loop Transfer Function	31
3.2.2 Frequency Response Design	32
3.2.3 Design of the Stable Feedback Filter	33
3.3 Active Isolation Setup	36
3.3.1 Internal Platform Modifications	36
Voice Coil Actuators	38

LVDT Displacement Transducer	38
3.3.2 Accelerometer	39
3.3.3 Voltage Controlled Voltage Source and Voice Coil Actuators	40
3.3.4 Feedback Filter Electronics	40
Implementation of the IIR Filters	40
Data Sampling and Logging	41
3.4 System Validation and Adjustment	42
3.4.1 Platform Excitation Response Measurement	42
3.4.2 Frequency Response of the Digital Feedback Filter	44
3.4.3 Nonlinearities and Hysteresis Effects	44
3.4.4 Position and Alignment of the Accelerometer	45
Sensor Alignment Measurement by Vertical DC Acceleration	46
Sensor Alignment Measurement by Direct Horizontal Excitation	47
Accelerometer Position and Tilt Coupling	49
3.5 Results and Discussion	50
3.5.1 Feedback Sensor Error Signal	50
3.5.2 Measurements by the Additional Sensor	52
3.5.3 Conclusion and Outlook	53
4 Detection System Development	55
4.1 Overview of common Detection Schemes	55
4.2 Detection Noise Sources	57
4.2.1 Quantum Projection Noise	58
4.2.2 Laser Noise	58
4.3 Double-Beam Absorption Spectroscopy	60
4.4 Predicted Performance of the Noise-canceling Absorption Detector	61
4.5 Implementation of the Balanced Absorption Detector System	63
4.6 Detection Sequence	64
4.7 Description of the Optical and Mechanical Design	65
4.7.1 General Remarks	66
4.7.2 Beam Paths	67
4.8 Conclusion and Outlook on the Detection System	68
A Light Force	73
B Voltage Controlled Current Source	75
C Self Noise of the CMG3 Accelerometer	77

Bibliography

83

Chapter 1

Introduction

The exact magnitude of the gravitation on the surface of the earth is subject to a variety of temporal and spacial fluctuations. The magnitude of these fluctuations ranges from $1 \times 10^{-6} g$ on a global scale to $1 \times 10^{-9} g$ on a regional scale, caused by changes in the local mass distribution around a site. Table 1.1 lists some of these variations.

Effect	Magnitude/ μgal
Geographical Gravity Variation	
global scale	1 gal
regional scale	1 mgal
Geological Effects	
tidal effects	200 μgal
tectonic plate movement	1 μgal
Environmental Effects	
atmospheric pressure	0.3 $\mu\text{gal}/\text{mbar}$
free air gravity gradient	3 $\mu\text{gal}/\text{cm}$
Man Made Changes	
trucks, people	1 μgal
buildings	10 μgal

Table 1.1: Gravitational Variations on the Earth and their magnitude in gal. The μgal is the preferred unit in gravimetry, the conversion is $1\mu\text{gal} = 10^{-8} \frac{m}{s^2} \approx 10^{-9}g$

Gravity fluctuation measurements are relevant for a number of scientific and non-scientific applications. Geodesists and geophysicists are interested in the exact value of g to verify and improve models of the earth's shape, composition and dynamic response to tidal forces. Precision force measurements exist to determine the mass of a body by supporting its weight using a very well known force [PSWR07]. The value of the determined mass can only be as accurate as the value of the gravitational acceleration.

The exploration of natural resources like oil and water also makes use of local gravity fluctuations.

Two types of instruments exist for measuring g ; relative and absolute gravimeters. The atomic-fountain gravimeter presented in this work belongs to the latter group. To appreciate the value of absolute measurements, however, it is beneficial to understand the principle of relative gravimeters.

Relative gravimeters need to be calibrated to a well known reference and measure a relative offset of g . Simple versions usually consist of a very well characterized spring which supports a constant weight against gravity. Monitoring the spring extension yields a value for the gravity fluctuations. A problem in these devices is drifts, which make frequent recalibration necessary and complicate comparing gravity readings taken at different times. The most precise relative gravimeters to date are cryogenic gravimeters which levitate a superconducting sphere in a magnetic field. A force-feedback mechanism counteracts gravity changes and yields the signal. Drift rates in these devices are much lower than in spring-type instruments, but vibration induced flux-jumps make readings taken at different places less comparable. Therefore they have to be calibrated for every measurement site using an absolute gravimeter.

Absolute gravimeters do not need a known reference and are required for applications which compare gravity values taken over long periods and distances. To date, the highest precision instruments of this type are falling corner cube gravimeters. They measure g by dropping a corner cube and monitoring its position during the fall with an interferometer. These instruments have existed since the 1950s and after many improvements have reached a sensitivity of about 2×10^{-9} g per single measurement [Pet98]. In the last twenty years this sensitivity has been limited by a number of systematic effects which are difficult to control. It has therefore not been significantly improved.

The first experiment which used cold atoms in a fountain to measure local gravity was set up in 1992 at Stanford University [KC92]. The basic principle is quite similar to a falling corner cube gravimeter. The position of a cloud of atoms during free fall is monitored and used to determine g . To reach the high accuracy needed for precision gravity measurements, the idea of matter-wave interferometry is employed. Common interferometers use the phase of electromagnetic radiation which has traveled along two different paths and is then recombined to deduce information about the difference in optical path length. Atom interferometers rest on the same principle. However, atoms are the medium carrying the phase information and the mirrors and beam-splitters are implemented by light pulses interacting with them. In effect, this approach works by measuring the atomic positions during free fall using the local phase of a coherent light field as a “meter stick”. The underlying physical mechanism is the atom-light interaction which imprints the local light phase into the phase of the atomic states during absorption or emission.

Atom interferometry can be used to build state of the art inertial sensors as well as to test fundamental physical theories. Experiments exploiting this technique quickly advanced from the first proofs of principle and were employed for precision measurements in which they challenged or exceeded the performance of the best available competing methods. This includes measurements of local gravity [Pet98], rotations [MGW⁺09] and gravity gradients [Mah09] as well as measurements of physical constants [WYC94], [FFMK07]. The principle can also be applied to tests of fundamental physical theories. This year the most precise test yet of the gravitational redshift was provided by reanalyzing the atom interferometer data taken at Stanford University by Achim Peters in the 1990s [MPC10].

This work is concerned with a transportable atom interferometer. Due to its mobile setup it can perform high precision gravity measurements at a number of interesting sites. It alleviates the shortcoming of most other atom interferometers to date which are confined to a laboratory and is therefore an exciting step towards establishing inertial sensors using atom interferometry in a broader scientific community.

The development and construction of subsystems of the interferometer has been carried out in the course of this work. To reach the required high sensitivity in g , an active low frequency vibration isolation system is needed to isolate one key component of the setup from ground motions. Such a vibration isolator has been constructed. The resulting measurements of tidal gravity variations have been compared to tidal predictions by using advanced geophysical models. Additionally, a new detection system for the interferometer setup has been designed.

Chapter 2

Atomic Fountain Gravimeter using Atom Interferometry

The first matter-wave interferometer using neutrons was realized in 1974 by Rauch and Bonse at the Österreichische Hochschule Vienna and the Universität Dortmund. It observed interference between neutron beams which were separated and then recombined using Si-crystals. In 1991 the first atom interferometers were realized using micro-fabricated slits [OJ91] and gratings [DCQD91]. The wider availability of atoms compared to neutrons opened up a wide range of possible applications. In the same year at Stanford University, light pulses interacting with atoms in an atomic fountain were used to build an atom interferometer [KC92]. This work was the first to use an atom interferometer as inertial sensor and set the basis for the setup described in this work.

2.1 Theory

2.1.1 Stimulated Raman Transitions

To coherently manipulate the atoms during an interferometer sequence, our setup uses a two photon process called stimulated Raman transition. During this process, the internal atomic state changes through excitation or de-excitation as well as the external state due to the associated momentum recoil. Exhaustive information about Raman transitions can be found in a variety of works [WYC94], [MWKC92]. The principle is illustrated in figure 2.1 and can be summarized as follows:

An atom is placed in two laser beams with the wave vectors \vec{k}_1 and \vec{k}_2 and with a frequency difference $\hbar\omega_{eff} = \hbar(\omega_1 - \omega_2)$ equal to the hyperfine splitting of the atom. A Raman transition occurs when the atom absorbs a photon from one light fields and adds a photon to the other light field by stimulated emission. The energy difference and

momentum absorbed or emitted during this process is given by:

$$\hbar\omega_{eff} = \pm\hbar(\omega_1 - \omega_2)$$

$$\hbar|\vec{k}_{eff}| = \hbar|\vec{k}_1 - \vec{k}_2|$$

It will be shown in the next section that the phase sensitivity of the atom interferometer is directly proportional to the effective wave number k_{eff} . Counter-propagating beams can be used to maximize the sensitivity, resulting in an effective wave number of $k_{eff} = k_1 + k_2$.

Our setup drives stimulated Raman transitions of ^{87}Rb between the $F = 1$ and $F = 2$ states of the D2 transition ground-state $5^2\text{S}_{1/2}$. The transition frequency between these two states is 6.8 GHz which belongs to the microwave range. Driving this transition directly using a microwave source transports a relatively small amount of momentum due to the small corresponding wave number. By driving stimulated Raman transition with two counter propagating optical beams, the effective k-vector in each transition is in the optical domain the order of $k_{eff} \approx 2\omega_1/c$ and about five orders of magnitude larger.

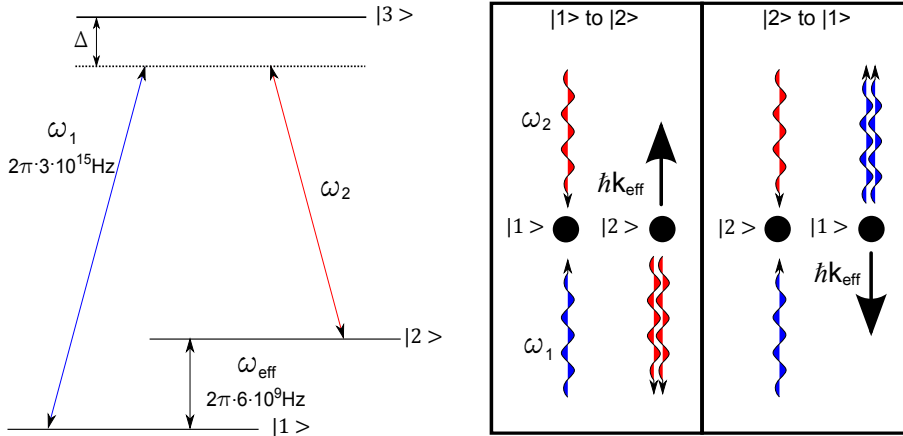


Figure 2.1: Raman transition atom between two hyperfine levels using counter-propagating beams.

2.1.2 Interferometer Sequence

Three Raman pulses are arranged in our setup to create a Mach-Zehnder type interferometry sequence which is illustrated and described in figure 2.2. Two $\pi/2$ pulses at the beginning and end of the sequence split and recombine the atoms. One π pulse in between acts as a mirror and switches the populations. Note that all movements and accelerations of the atoms are vertical and not horizontal as might be suggested at the first glance by the space-time diagram. Along the two paths of the interferometer, the internal state of the atoms evolves separately. A phase difference $\Delta\Phi$ between the two paths can therefore occur. Two main contributions exist during the interferometer sequence, one is caused by

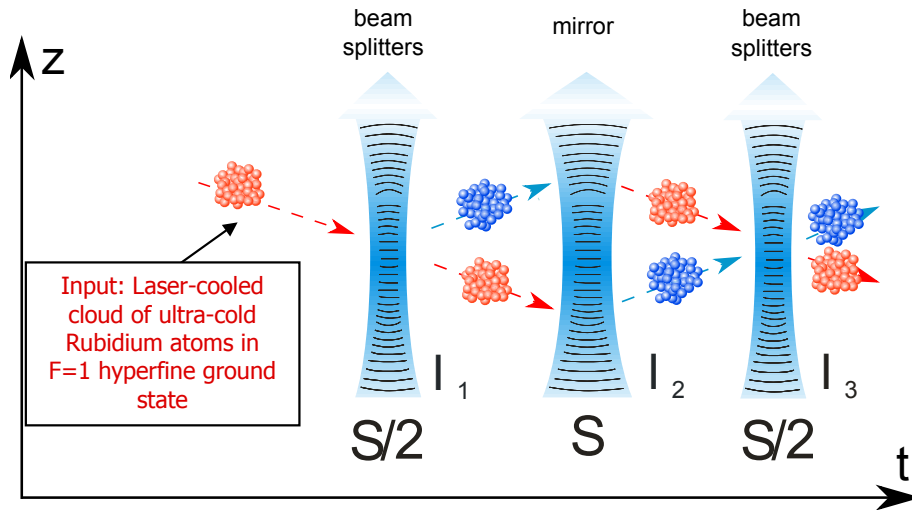


Figure 2.2: Interferometer sequence using light pulse to split and recombine a cloud of laser cooled ^{87}Rb atoms in a space-time diagram. The blue arrows represent the Raman pulses. The first pulse has an area of $\pi/2$ and transfers half of the population to the other state. Due to the associated momentum transfer the excited atoms separate from the ground state atoms. A π pulse then flips the atom populations from the excited into the ground state and vice versa, making the two clouds approach each other again. When they overlap, a second $\pi/2$ pulse transfers the excited population back to the ground state, depending on the phase difference between the two paths. Figure by IQO Hannover

the internal state evolution along the path $\Delta\Phi_{path}$ and the other one by the atom-light interaction with the Raman-pulses $\Delta\Phi_{light}$:

$$\Delta\phi = \Delta\phi_{path} + \Delta\phi_{light} \quad (2.1)$$

The first contribution $\Delta\Phi_{path}$ is due to the evolution of the atomic wave function $\Psi(z, t)$ along an interferometer arm. As shown in [SCT94], it acquires a phase shift during this evolution which depends on the classical action along the traversed path. The corresponding phase shift between the two interferometer arms can therefore be written as:

$$\Delta\phi_{path} = \frac{1}{\hbar} (S_{cl}^B - S_{cl}^A) = \frac{1}{\hbar} \int_0^{2T} \mathcal{L}(z_B, \dot{z}_B) - \mathcal{L}(z_A, \dot{z}_A) dt \quad (2.2)$$

When considering uniform gravity fields, $\Delta\phi_{path}$ can be shown to vanish [SCT94]. Note, however, that this is not the case when gravity gradients are taken into account.

The second contribution is due to the atom-light interaction. Every time the atom interacts with the Raman pulse and changes its state it acquires an additional phase that depends on the local phase of the light phase $\pm\phi_i$. The sign of this additional phase depends on the initial state of the atom. Since the Raman phase depends on the position, the atoms will acquire different phases in the two interferometer arms. When using the

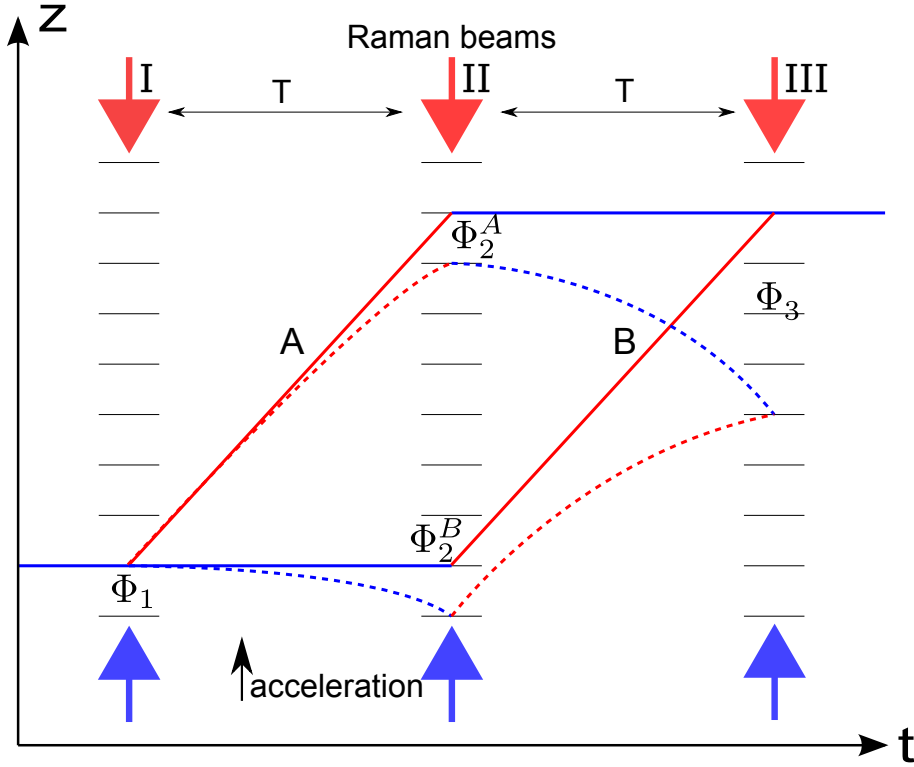


Figure 2.3: Space-time diagram of the interferometer paths with gravity (dashed line) and without gravity (solid line). Note that with gravity, the atoms fall 3 times as far in the second half of the sequence as in the first. The additional phase picked up by the atoms during the Raman pulses is denoted as Φ . The resulting phase shift between both arms is deduced in the text.

notation from figure 2.3, the resulting phase shift $\Delta\Phi$ at the end of the interferometer sequence is given by:

$$\Delta\Phi_{light} = (\Phi_1 - \Phi_2^A) - (\Phi_2^B - \Phi_3) \quad (2.3)$$

For atoms in free fall with a gravitational acceleration g , the phase Φ seen by an atom at time t is given by:

$$\Phi(t) = \vec{k}_{eff} \cdot \vec{z}(t) \quad (2.4)$$

$$= \vec{k}_{eff} \cdot \frac{\vec{g}}{2} t^2 \quad (2.5)$$

We will now deduce the individual phase shifts terms in equation 2.3 from the atomic positions throughout the interferometer sequence, as illustrated in figure 2.3. An additional phase offsets Φ_I, Φ_{II} and Φ_{III} due to an arbitrary initial phase of the Raman beams will

also be taken into the account.

$$\Phi_1 = \Phi_I \quad (2.6)$$

$$\Phi_2^A = \Phi_{II} + \vec{k}_{eff} \cdot \vec{v}_{rec}T - \vec{k}_{eff} \cdot \frac{\vec{g}}{2}T^2 \quad (2.7)$$

$$\Phi_2^B = \Phi_{II} - \vec{k}_{eff} \cdot \frac{\vec{g}}{2}T^2 \quad (2.8)$$

$$\Phi_3 = \Phi_{III} + \vec{k}_{eff} \cdot \vec{v}_{rec}T - \vec{k}_{eff} \cdot \frac{\vec{g}}{2}(2T)^2 \quad (2.9)$$

Combining equations 2.9 and 2.3 yields the result for the light induced phase shift. Together with equation 2.1 we have:

$$\Delta\Phi = -\vec{k}_{eff}\vec{g}T^2 + \underbrace{\Phi_I - 2\Phi_{II} + \Phi_{III}}_{\text{Raman laser phase}} \quad (2.10)$$

If the phase of the Raman lasers is known and stable, equation 2.10 can be used to determine the magnitude of g along the vector \vec{k}_{eff} . The equation describes the system very well and only has to be modified if gravity gradients and Raman pulses with a finite length are taken into account. [Pet05] and [Pet98] provide a detailed description of these effects.

$\Delta\Phi$ can be measured by determining the population of the two atomic states in the atom cloud. As shown in [Pet98] or [Pet05], the interferometer phase $\Delta\Phi$ is related to the population of the upper fine structure state through the following equation:

$$P_{|2\rangle} = \frac{1}{2} (1 + \cos(\Delta\Phi)) \quad (2.11)$$

2.1.3 Summary

A Mach-Zehnder type atom interferometer has been described. It uses stimulated Raman transitions to coherently manipulate the atoms in their internal state and their momentum. The phase difference between the atomic wave-functions in the two arms can be used to measure local gravity as shown by equation 2.10. It can be detected by measuring the population of the atomic states after the interferometer sequence as described by equation 2.11.

To estimate the expected uncertainty when measuring g we can use the known value for k_{eff} and a typical Raman pulse separation of $T = 150$ ms. With these parameters and an expected error of 0.10 rad in measuring the interferometer phase, the relative uncertainty in the determined gravity value for a single measurement would be:

$$\frac{\Delta g}{g} = 2.8 \times 10^{-8}$$

This is a very accurate value and competes with the best available absolute gravimeters available today based on different measurement principles. Phase noise introduced by

mechanical vibrations of optical elements, however, effectively reduce the sensitivity of the interferometer without vibration isolation to a much lower value of $\frac{\Delta g}{g} = 10^{-3}$. The active vibration isolation platform described in chapter 3 removes this limitation and allowed us to achieve an accuracy of $\frac{\Delta g}{g} = 7 \times 10^{-8}$ in a single measurement.

2.2 Experimental Setup

The atom interferometer works in pulsed operation. One operational sequence can be divided into preparation of the atom sample, the interferometer pulse sequence and the detection of the atoms afterwards. The entire procedure is carried out in a vacuum chamber with a pressure of 1×10^{-10} mbar.

In the first step about 10^8 ^{87}Rb atoms are loaded into a magneto-optical trap (MOT) from background vapor which is created by a heated dispenser. The atoms are cooled to a temperature of approximately $40 \mu\text{K}$ in the MOT. After loading time, the atoms are launched upwards using moving molasses by detuning the MOT-lasers. On their way to the interferometry zone, a state selection sequence is carried out by velocity-selective Raman pulses and optical pumping. It transfers the atoms in the hyperfine ground state $|F = 1, m_F = 0\rangle$ to make them insensitive to Zeeman shifts due to residual magnetic fields. The vertical velocity distribution of the atoms is also reduced to an effective temperature in the vertical direction of a few nanokelvin which is necessary to narrow the Doppler line-width of the atoms. After state selection, the atoms enter the magnetically shielded interferometry zone. The $\frac{\pi}{2}$ - π - $\frac{\pi}{2}$ Raman-pulse sequence which splits, flips and recombines the atom cloud is described in section 2.1.2.

Both Raman beams enter the vacuum chamber at the top of the interferometry zone and are retro-reflected by a mirror below the MOT-zone outside the vacuum. By chirping both Raman lasers according to the Doppler shift of the moving atoms it is possible to select one upward and one downward traveling beam for the Raman transition.

Retro-reflection is used to tackle the problem of phase noise between the two Raman beams introduced by mechanical vibrations of optical elements. This phase noise directly couples into the interferometer phase and completely washes out the interferometer fringes for longer pulse separations if not addressed. If both beams are guided into the vacuum chamber by separate optical elements, the whole apparatus needs to be isolated from vibrations. This is illustrated in figure 2.5. By using the same optical elements for both Raman beams and using retro-reflection, vibrations of most optical elements are common-mode and cancel out. Only vibrations of the retro-reflecting mirror at the bottom of the vacuum chamber induces phase noise as illustrated in figure 2.8. Therefore, only this mirror therefore has to be isolated against floor vibrations. Constructing a vibration isolation platform capable of delivering sufficient performance has been the main task of this work and is described extensively in chapter 3.

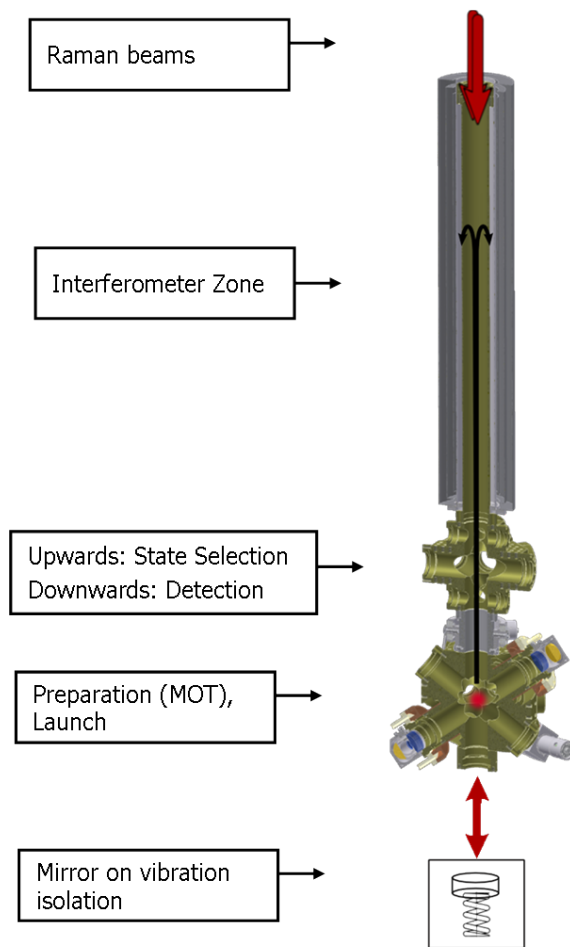


Figure 2.4: Functional elements of the vacuum chamber with a sketch of the atom trajectory during an interferometer sequence. Courtesy of A.Senger

After the interferometer sequence the atoms enter the detection zone. During detection, a resonant laser beam drives the $F = 2 \rightarrow F' = 3$ transition of the atoms. By measuring how much light is absorbed or emitted by the atoms, the population in the $F = 2$ state can be detected. The atoms in the hyperfine ground state $F = 1$ are then transferred to the $F = 2$ state using an additional laser beam. Another detection then measures the total number of atoms.

The mechanical part of the setup consists of the vacuum chamber in a mobile cart and the vibration isolation system which isolates the retro-reflection mirror against ground motions. The electronic and optic parts of the interferometer are mounted in two 19" racks. One rack houses the complete laser system and another has all the electronic and computer systems necessary for operation built in. All components are small enough to fit through a standard sized door. See figures 2.6 and 2.7 for an overview of the system.

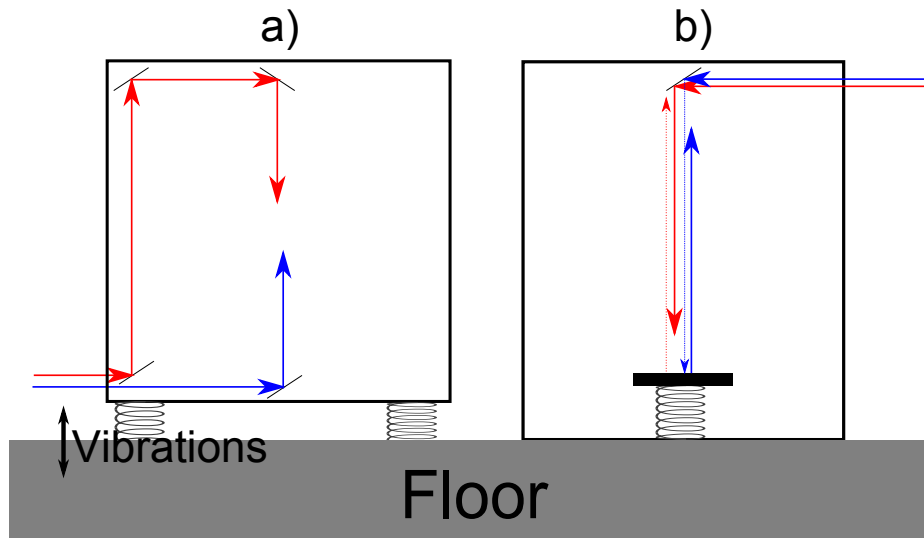


Figure 2.5: Different schemes for suppressing vibration induced Raman phase noise: a) without retro-reflection b) with retro-reflection. Two different frequency components (blue, red) drive Doppler-sensitive Raman transitions depending on their propagation direction,.

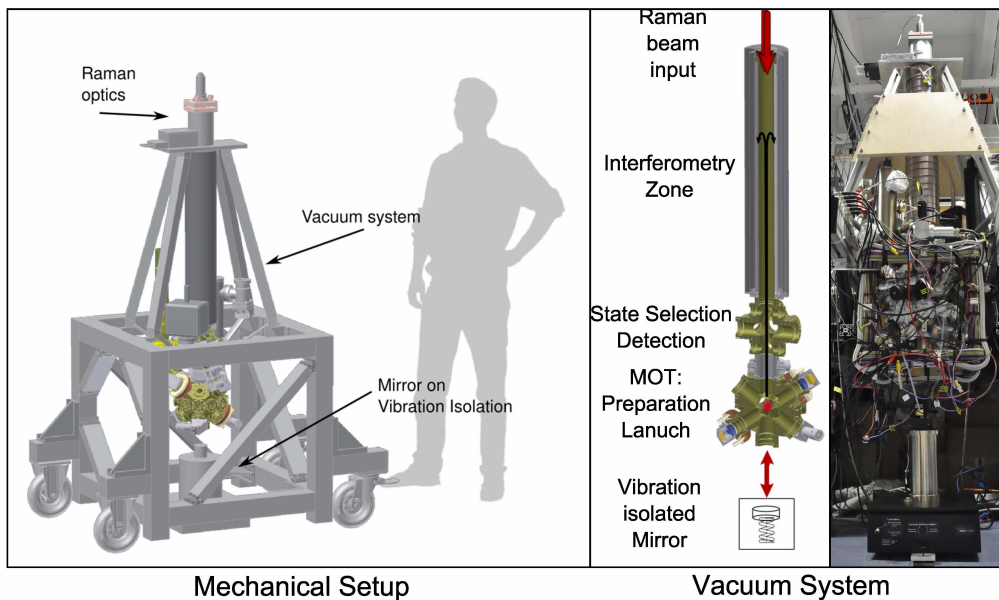


Figure 2.6: Overview over the setup. The completed vacuum system in a mobile cart with the vibration isolation in the bottom is shown on the left. The picture on the right shows the system just before it was moved into the cart.

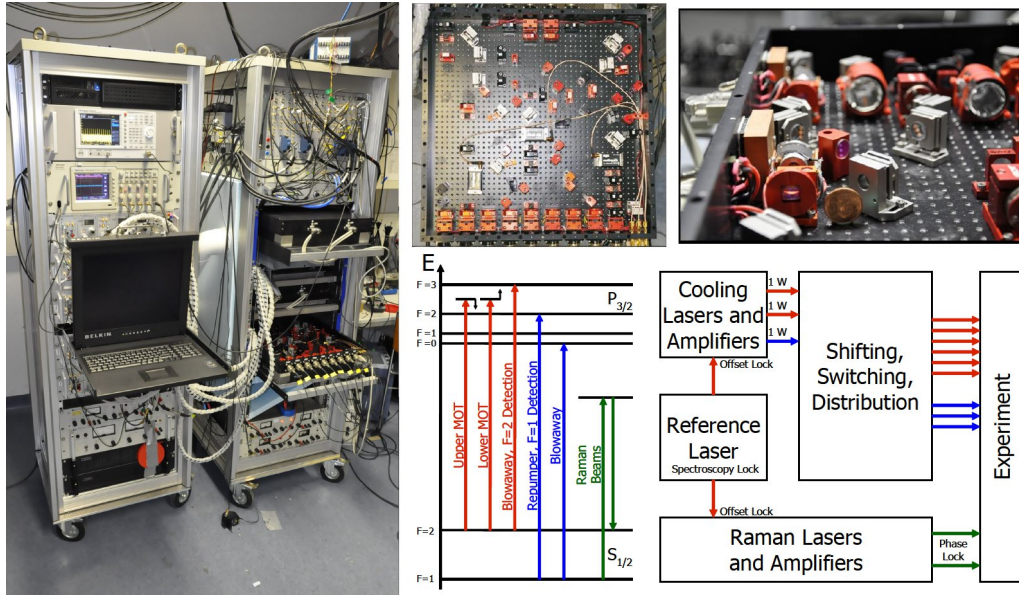


Figure 2.7: Overview of the electronics rack and the optics rack housing the laser system. All electronics and lasers necessary for atom interferometry is provided by the modules in the rack, including the Raman-, MOT- and repumper-laser and a spectroscopy locked reference. This was achieved by using custom designed micro-optics. For more information on the laser system, see [SPG⁺10]. Courtesy of M.Schmidt.

2.3 Vibration Noise in the Atom Interferometer

Many noise sources exist in the atom interferometer and decrease its sensitivity if not addressed. These noise sources have been studied extensively in other works [LMK⁺08] [Pet98]. Only vibrations of the retro-reflecting mirror are discussed here because they are the most relevant to this work and currently limit the sensitivity of the atom interferometer. Before the implementation of the active vibration isolation, phase noise due to vibration motions of the retro-reflecting mirror limited the sensitivity of the interferometer to $\Delta g = 2 \cdot 10^{-6}g$ for a single measurement. After implementation the sensitivity has improved by almost two orders of magnitude and is in the range of $\Delta g = 6 \cdot 10^{-8}g$. As the issues (discussed in chapter 3) in the current active vibration isolation system are rectifiable, we are confident that the sensitivity of the interferometer can be improved even further.

As mentioned in section 2.2 vibration induced displacements of most optical elements are common to both beams and cancel out. Only vertical vibrations of the retro-reflecting mirror underneath the vacuum chamber will translate into interferometer phase noise and lower the sensitivity of the instrument. We therefore investigated the effect of these vibrations on the interferometer phase and estimated the benefit of the active vibration isolator.

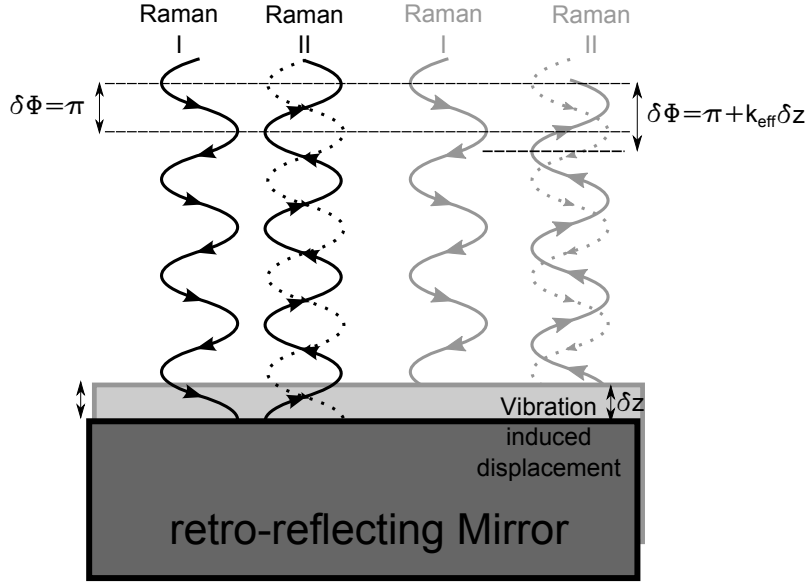


Figure 2.8: Vibration induced phase noise. The relative phase between Raman laser I and II changes depending on the displacement δz which are depicted by black/grey lines.

The effect of Raman phase noise on atom interferometer fringes has already been studied in [CCD⁺05] and [LMK⁺08]. A transfer function of the interferometer is introduced which relates the input Raman phase noise spectrum $S_\phi(\omega)$ to the interferometer phase standard deviation σ_Φ^{rms} :

$$(\sigma_\Phi^{rms})^2 = \int_0^\infty |H_\phi(\omega)|^2 S_\phi(\omega) d\omega \quad (2.12)$$

Here, $S_\phi(\omega)$ is the power spectral density of the Raman phase noise in rad^2/Hz . $H_\phi(\omega)$ is the transfer function of the Interferometer. It is given by the oscillating function:

$$H_\phi(\omega) = -4 \sin^2 \frac{\omega}{2} T \quad (2.13)$$

With T being the time between two interferometer Raman pulses. Equation 2.13 assumes infinitely short Raman pulses and large effective Rabi frequencies $\Omega_{eff} \gg \omega$. Since we are interested in large pulse separations of about $T = 150 \text{ ms}$ and short Raman pulses with a duration of $\tau = 100 \mu\text{s}$, the approximation is valid here. The effective Rabi frequency Ω_{eff} is given by:

$$\Omega_{eff} = \frac{\pi}{2\tau} \approx 5000 \times \pi$$

The influence of ground vibrations on the interferometer phase decreases quickly for higher frequencies as can be seen in figure 2.10. Effectively, only frequencies with $\omega \leq 60 \text{ rad/s}$ contribute to the interferometer phase noise. The second assumption in equation 2.13 is, therefore, also valid.

As illustrated in figure 2.8, vertical displacements δz of the retro-reflecting mirror correspond to a phase shift $\delta\phi/k_{eff}$ between the two Raman beams. The vibration induced Raman phase noise is therefore:

$$S_\phi(\omega) = k_{eff}^2 S_z(\omega) = \frac{k_{eff}^2}{\omega^4} S_a(\omega) \quad (2.14)$$

$S_a(\omega)$ is the power spectral density of vertical mirror vibrations in units of $(\text{m/s}^2)^2/\text{Hz}$. The corresponding Interferometer phase noise is then given by:

$$(\sigma_\Phi^{rms})^2 = \int_0^\infty |H_\phi(\omega)|^2 \frac{k_{eff}^2}{\omega^4} S_a(\omega) d\omega \quad (2.15)$$

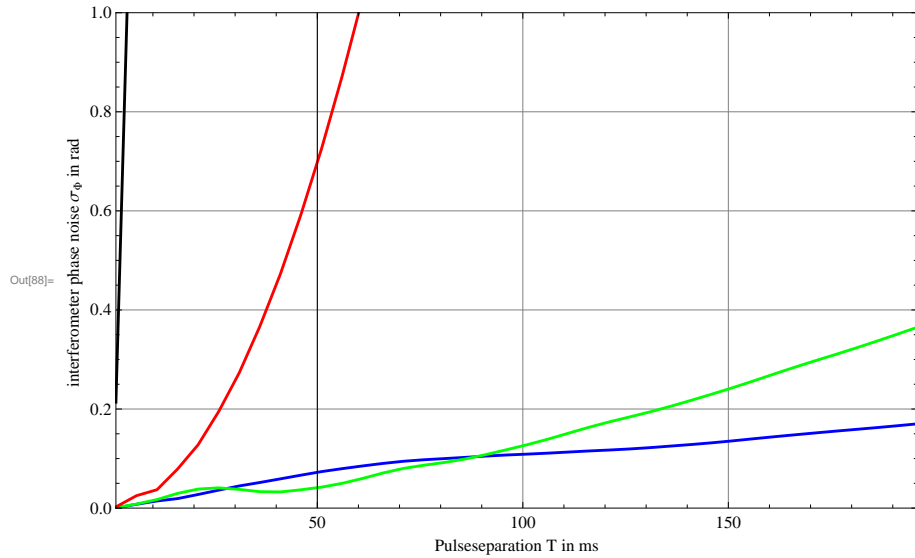


Figure 2.9: Interferometer phase noise versus pulse separation T , derived from vibration noise spectra taken in our laboratory. The blue and green line show the improved phase noise after the implementation of the active vibration isolator as measured using the feedbackloop error signal or a direct measurement using a 2nd sensor. All measurements were made in a typical lab environment in a busy university building.

Figure 2.9 shows a plot of σ_Φ^{rms} from equation 2.15 versus the interferometer pulse spacing T . The phase noise obviously increases as T is increased. Without vibration isolation, the resulting phase noise completely washes out the interferometer fringes for pulse spacings of more than a few microseconds. The passive vibration isolator allows for pulse spacings smaller than approximately 40 ms. Only the active system, however, is capable of controlling the phase noise well enough to see fringes at $T = 100$ ms and more.

The error in g is related to the interferometer phase noise using formula 2.3:

$$\sigma_g^{rms} = \frac{\sigma_\Phi^{rms}}{k_{eff} T^2} \quad (2.16)$$

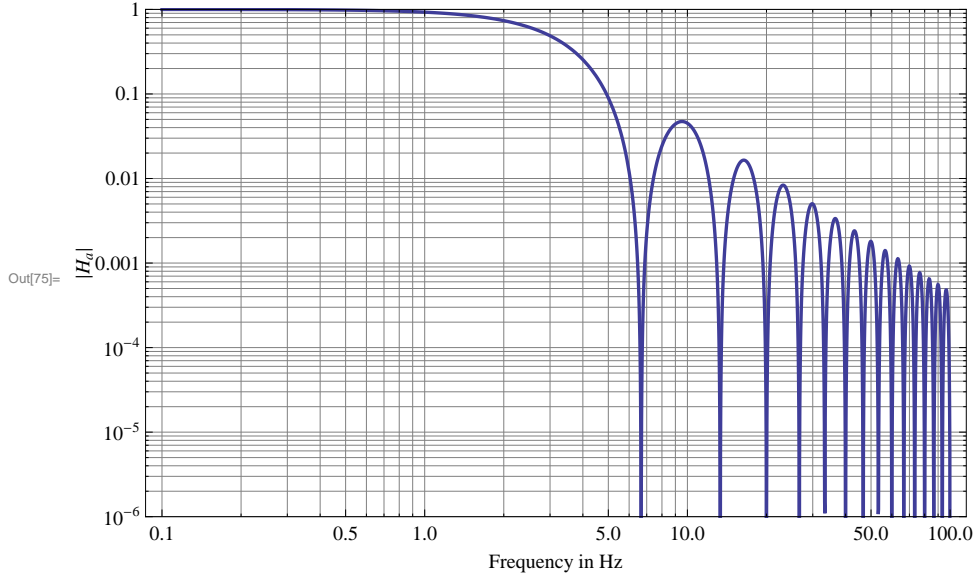


Figure 2.10: Vibration sensitivity function of the atom interferometer with a pulse separation $T = 150\text{ms}$. Frequencies below 10 Hz clearly have the strongest influence whereas at higher frequencies the amplitude decreases proportional to ω^{-2} . Note that the corner frequency depends on T .

Combining equations 2.14, 2.15 and 2.16, we find the standard deviation of g and define a second transfer function H_a which relates it to the input vibration spectrum and is shown in figure 2.10:

$$(\sigma_g^{rms})^2 = \left(\frac{\sigma_\Phi^{rms}}{k_{eff}T^2}\right)^2 = \int_0^\infty \underbrace{|H_\phi(\omega)|^2 \frac{1}{T^4\omega^4}}_{=: |H_a(\omega)|^2} S_a(\omega) d\omega \quad (2.17)$$

As shown in figure 2.10, the magnitude of the transfer function decreases for higher frequencies. The interferometer therefore works as a second order low-pass filter and is most sensitive to low frequency vibrations below 10 Hz.

This effect is shown in figure 2.11. It plots the residual vibration noise on the active vibration isolator shown in yellow. The red line shows the same spectrum weighted by the interferometer transfer function for $T = 150\text{ ms}$. The third line in blue displays the accumulated measurement error from low to high frequencies and shows in which frequencies the noise spectrum contribute most to the error. Vibrations with frequencies above approximately 10 Hz are negligible for the atom interferometer due to its decreased sensitivity at higher frequencies. Between 1 Hz and 10 Hz residual vibrations add about $3 \times 10^{-8}\text{ g}$ of measurement noise to the signal. Note that without active vibration isolation, the resonance peak of the passive platform at 0.5 Hz would add more than ten times as much noise to the system. Lower frequencies in the sub-Hertz range account for the rest of the measurement noise.

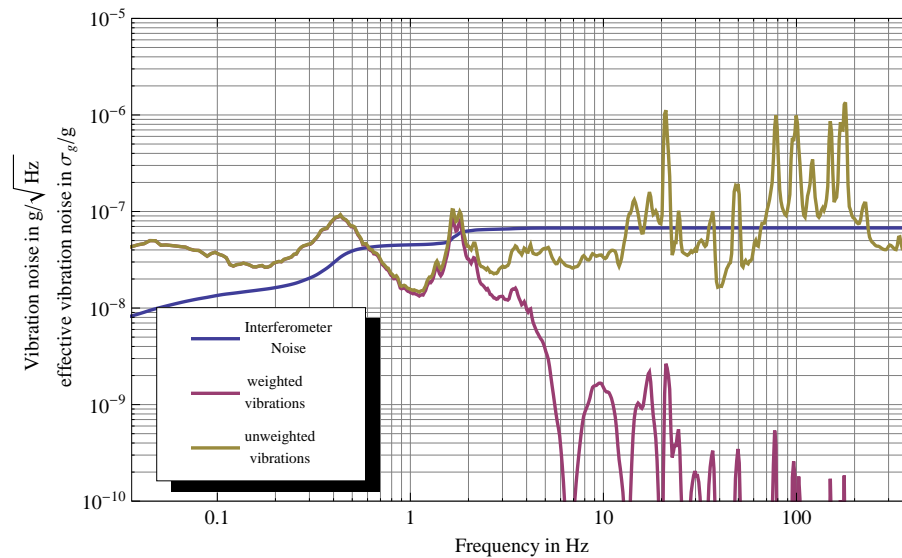


Figure 2.11: Vibration noise spectrum raw and weighted by the interferometer transfer function on the active vibration isolator. Shown in blue is the accumulated error in g due to the vibration noise.

Using equation 2.17 we predict the sensitivity limits of our gravimeter given the vibration noise measured in our lab and on the vibration isolator and compare it to the measured phase noise. Table 2.1 shows the improvement introduced by the passive and active vibration isolator and shows that the theoretical values are in agreement with the measured shot to shot noise level of the interferometer.

2.4 Prediction of tidal Gravity Variations

Tidal variations of g reach an amplitude of up to $200 \mu\text{gal}$ or $2 \times 10^{-7} g$ as shown in table 1.1. Since the sensitivity of most gravimeters is better than that, the tidal fluctuations are usually subtracted from gravimeter data to obtain one stable gravity value for a given site. Accurate prediction of these fluctuations is a field of research in itself and geophysical tide models for this purpose are available. We will give a short insight into these models and then present the obtained corrections for our location in central Berlin.

Tidal accelerations result from the dynamics of the celestial bodies in the solar system. The earth and the moon, for example, rotate around their common center mass in about one month's period. Only in their common center of mass, which is located inside the earth's body due to its bigger mass, the attracting gravitational force and the repelling centripetal force cancel each other out. Every other site like the earth's surface is subject to residual gravitational or centripetal forces called tidal forces. The same holds true for the sun and on a much smaller magnitude for the other planets in the solar system. For

Spectrum	T in ms	predicted σ_g/g	measured σ_g/g
lab floor	1	1×10^{-3}	1×10^{-4}
passive vibration isolator	30	3.3×10^{-7}	4.5×10^{-7}
passive vibration isolator	40	3.1×10^{-7}	4×10^{-7}
active isolator feedback loop output	100	1.3×10^{-8}	2×10^{-8}
active isolator feedback loop output	150	0.7×10^{-8}	1.65×10^{-8}
active isolator, measured with 2nd sensor	100	1.4×10^{-8}	2×10^{-8}
active isolator, measured with 2nd sensor	150	1.3×10^{-8}	1.65×10^{-8}

Table 2.1: Theoretical sensitivity improvements achieved by improving the vibration isolation system. The measured noise levels were obtained by scanning through an interferometer fringe within 65 measurements and fitting the phase of the fringe. Predicted and measured values are in good agreement, residual differences can be due to measurement artifacts or differences in the fit errors used for determining the experimental values. The values also show that residual vibrations are still limiting the sensitivity of the sensor.

a perfectly rigid earth without oceans, liquid core etc., the resulting acceleration \vec{a}_t is usually described in terms of the tidal potential V_t :

$$\vec{a}_t = \nabla V_t$$

A derivation for the tidal potential can be found in [Tor03]. It can be calculated directly using the positions of the celestial bodies, also called ephemerids. For practical purposes, however, it is usually expanded into a quickly converging series, more details can be found in [Tor03]. The spectral components of this expansion are called tidal waves and are classified by their period into long semi-diurnal, diurnal and long-period waves. Some tidal waves can also be referred to a certain celestial body and have an according name. The semi-diurnal wave which is created by the moon is called “M2”, the diurnal wave by the sun “S0” etc. A more exhaustive list of tidal waves can also be found in [Tor03]. They vary in amplitude and phase for different sites on earth.

The rigid earth model is a crude approach, however, and many deviations from the resulting tide predictions are present in real measurements. More sophisticated earth models consider a rotating, elastic, isotropic and elliptic earth with a liquid outer core. Oceanic tides, which are very different from earth tides, have also been modeled. This includes an effect called ocean tide loading, which induces a height change off the continents due to shifting water masses caused by oceanic tides. The water literally pushes the continents down.

To include these more realistic models into the tidal potential, the tidal waves are modified by the amplitude factors δ and phase factors $\Delta\phi$, called tidal parameters. These

tidal parameters are obviously site dependent and can be determined for a given position by fitting gravimeter data to the tidal waves [Tor03] or by synthetic models. Since we did not have the means yet to gather enough gravimetric data to determine these parameters at our location, we calculated synthetic tidal parameters.

Global earth and ocean tide models are available to predict the tidal parameters for a given station [TW94] and are often distributed in a 1° by 1° grid. Synthetic tide parameters can then be calculated by interpolation from the grid for a given site. It was shown that these values usually deviate from the measured tidal parameters by less than one percent [Tor03], [ZJS05] and provide a very good approximation of the measured tidal parameters.

Figure 2.12 shows two sets of tidal corrections data for the same period. The set in the black line uses tidal parameters measured for the Geodätisches Observatorium Wettzell in southern Germany, the blue line represents synthetic parameters calculated for Berlin. The resulting predictions differ by about $10 \mu\text{gal}$ at some points, but agree very well in the general appearance and timing. In fact our current gravimetric data does not yet allow us to determine which tide predictions fit our measured data better.

All tidal corrections presented in this work were calculated using the “predict” from the earth tide data processing package “Eterna 3.3”. The suite bundles various DOS programs to take and process gravimeter data, fit tidal parameters to the data and to predict future tidal corrections. The synthetic tidal parameters were interpolated using the program “wparex”, which is also part of the Eterna package.

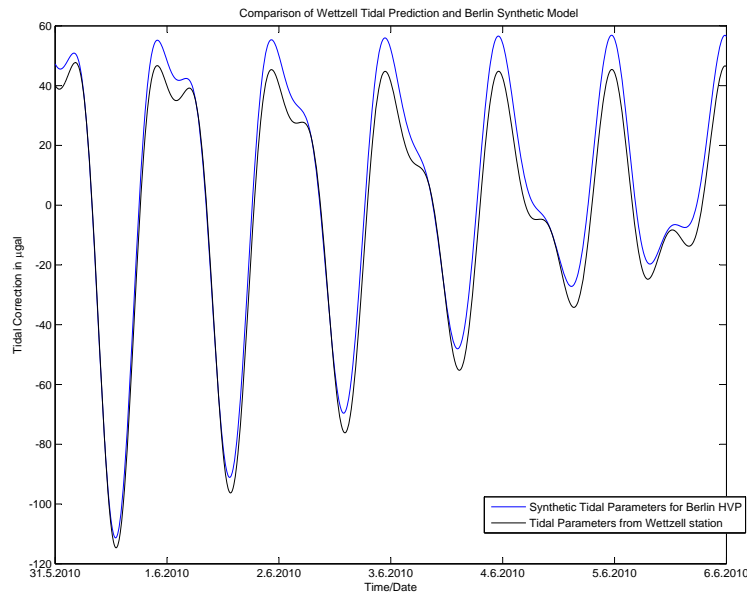


Figure 2.12: Comparison of Wettzell tide predictions and the synthetic tide model for central Berlin

2.5 Measurement of Tidal Gravity Variations

Figure 2.13 shows a plot of three gravity measurements in our laboratory in central Berlin taken between May 31st and June 5th 2010.

The gravity values were obtained by adjusting the Raman laser phase from equation 2.10 to scan through an interferometer fringe within 65 consecutive measurements. The interferometer phase $\Delta\Phi$ was then determined by fitting the phase of the obtained fringe to equation 2.11. Equation 2.10 was used to determine a corresponding gravity value. The blue data points in figure 2.13 represent averages of 5 individually obtained gravity values. Therefore, $5 * 65 = 325$ interferometer sequences created one measurement point. An offset of several hundred μgal had to be added to the obtained gravity values to bring them to agreement with the calculated tidal predictions. This is necessary because the tidal corrections do not include an absolute gravity value and only represent a relative correction. Apart from the offset the predicted tidal gravity variations are in good agreement with our measured data. The tidal model used is based on synthetic parameters calculated for Berlin and should be in very good agreement with the actual tides. This shows that our interferometer actually reached the predicted sensitivity of 7×10^{-8} g per single measurement and approximately 1.65 g when averaging over 65 measurements.

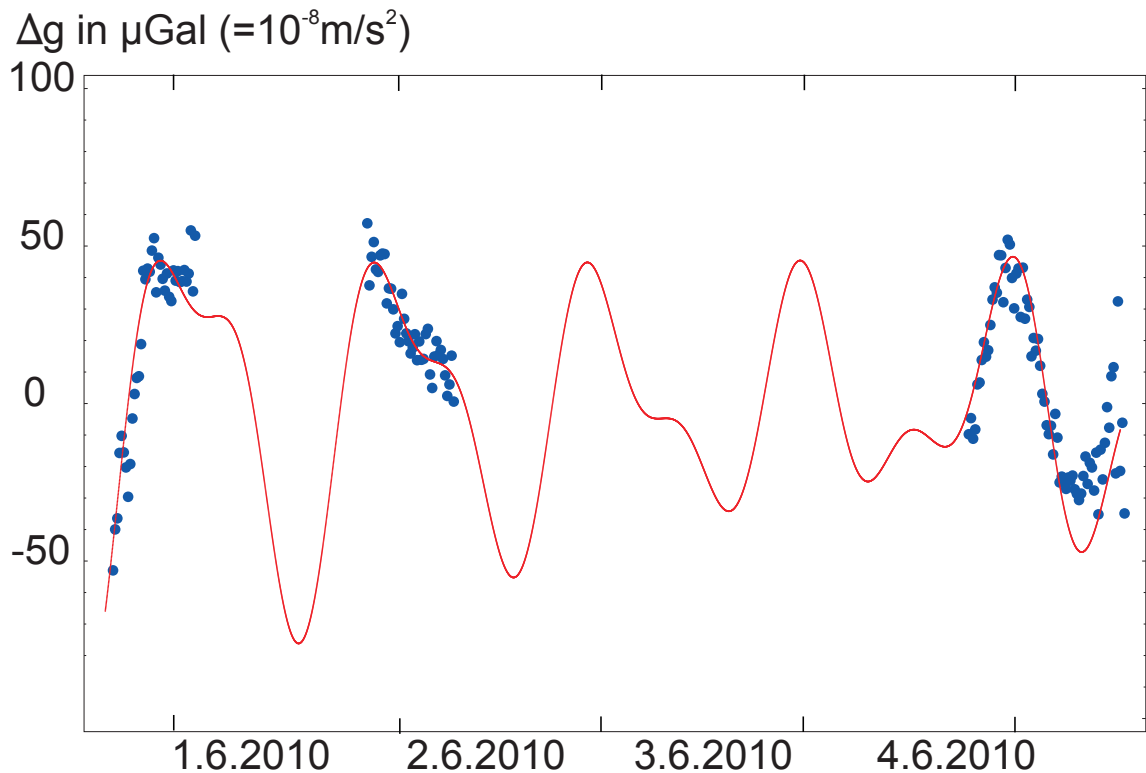


Figure 2.13: Long term gravity measurements taken over a period of six days showing tidal gravity variations. The blue dots are the measured gravity value, the calculated tidal corrections are shown in red. Note that the prior to implementing active vibration isolation, the measurement error was twice as large as the displayed y-axis range.

The offset of the data changed for the three measurement periods taken on different days shown in figure 2.13 which indicates that changing systematic effects influence the measured gravity value. The most likely cause of this deviation is misalignment. The instrument had been realigned between these measurements and the tilt possibly deviates by several hundred μrad in the current setup.

Several other systematic effects also exist in our setup and will have to be controlled in the future to obtain reliable absolute gravity measurements. An extensive treatment of these numerous effects can be found in [Pet98].

2.6 Conclusion and Outlook

The principle of atom interferometry has been described and an introduction of our experimental setup has been given. Vibrations of the retro-reflecting Raman-mirror have been identified as the main source of measurement noise. Their influence has been theoretically described and estimated using measured vibration spectra. As shown in table 2.1, the

estimated noise levels compare well to the observed measurement noise which shows that the atom interferometer is currently still limited by residual vibration.

The implementation of an active vibration isolation system throughout this work has significantly increased the resolution of the measured gravity data. It is now possible to observe tidal gravity variations. A multi-day measurement of tidal gravity data has been presented and shown to be in agreement with geological tidal models.

Further improvements of the active vibration isolator are on their way to increasing the sensitivity of the atom interferometer. To obtain a reliable absolute gravity value, the control of systematic effects will have to be improved. Improvement of the vertical alignment of the interferometer is the first step. Many other systematic effects which are described extensively in [Pet98] also have to be considered.

Chapter 3

Very Low Frequency Vibration Isolation

As derived in chapter 2.3, appropriate vibration isolation of the retro-reflecting mirror is crucial for achieving clean atom interferometer fringes at long pulse separations. In addition our mobile setup requires that the vibration isolator used to achieve this goal has a small enough footprint to be easily transportable. As a starting point for such a system we chose a high performance passive vibration isolator which meets these mobility requirements. Since the performance of this isolator was still not good enough, it was modified and extended to an active system in the course of this work.

3.1 Passive Vibration Isolator

We used a passive vibration isolator 50BM-10 fabricated by MinusK Technology Inc. as the starting point for our vibration isolation system. It has a net payload of 16 kg to 25 kg and is easily transportable with dimensions of approx. $30 \times 30 \times 12$ cm and a weight of 16 kg. By employing a patented mechanism using negative stiffness elements, it provides vibration isolation in 3 spatial directions with a low vertical resonance frequency of 0.5 Hz and a horizontal resonance frequency of 1.5 Hz. The platform works with mechanical springs and does not require electrical power. To gain deeper insight into the performance and limitations of the isolator, we modelled the system as single degree-of-freedom oscillator with viscous damping.

A mass m can be decoupled from ground motions by suspending it on a spring with stiffness k and damping β as seen in figure 3.1. By analyzing the system we get a well known linear 2nd order dynamic equation with constant coefficients:

$$\ddot{z} + 2m\omega_0\zeta_0(\dot{z} - \dot{z}_g) + \omega_0^2(z - z_g) = 0 \quad (3.1)$$

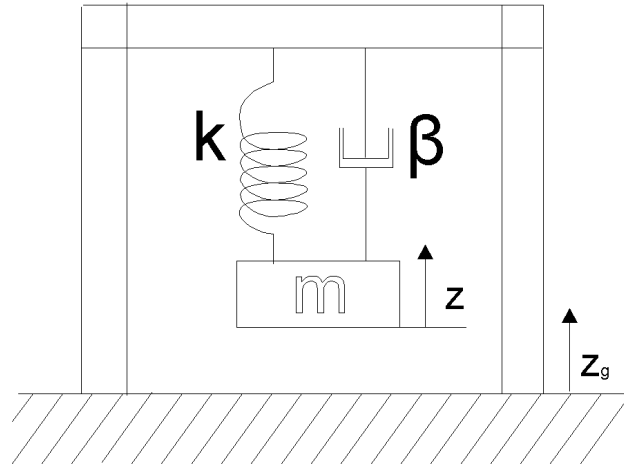


Figure 3.1: Damped spring mass system. Vibrations travel through a rigid support structure and the spring. The system is characterized by the natural resonance frequency $\omega_0 = \sqrt{\frac{k}{m}}$ and the damping ratio $\zeta_0 = \frac{\beta}{2m\omega_0}$

z is the position of the mass, z_g the ground position, $\omega_0 = \sqrt{\frac{k}{m}}$ is the undamped natural frequency and $\zeta_0 = \frac{\beta}{2m\omega_0}$ is the damping ratio. $\zeta_0 = 1$ denotes a critically damped system, $\zeta_0 = 0$ corresponds to zero damping.

Note that the floor does not act as a reference point to the coordinate system but is actually an active moving element in the dynamic system. The coordinate system is rather defined as an inertial frame fixed to the laboratory. This is an important difference in comparison to, for example, the harmonic oscillator hinged to a fixed reference point which changes the solution of the system.

3.1.1 Absolute Transmissibility

We transform equation 3.1 into the frequency domain. By writing the the Fourier transform of mass and ground motion as \tilde{z} and \tilde{z}_g we end up with the result:

$$G_{passive} = \frac{\tilde{z}}{\tilde{z}_g} = \frac{2(i\omega)\zeta_0\omega_0 + \omega_0^2}{-\omega^2 + 2(i\omega)\zeta_0\omega_0 + \omega_0^2} \quad (3.2)$$

This is the transfer function of the system. The absolute value of this function is often denoted as absolute transmissibility in the context of vibration isolation. Figure 3.2 shows the measured transmissibility of the MinusK passive vibration isolation platform. It shows the following general features:

- Frequencies lower than the natural frequency will pass through the isolator unchanged.
- At the natural resonance frequency, the transmissibility shows a resonance peak at which the isolator will amplify the vibrations. The resonance peak will be very

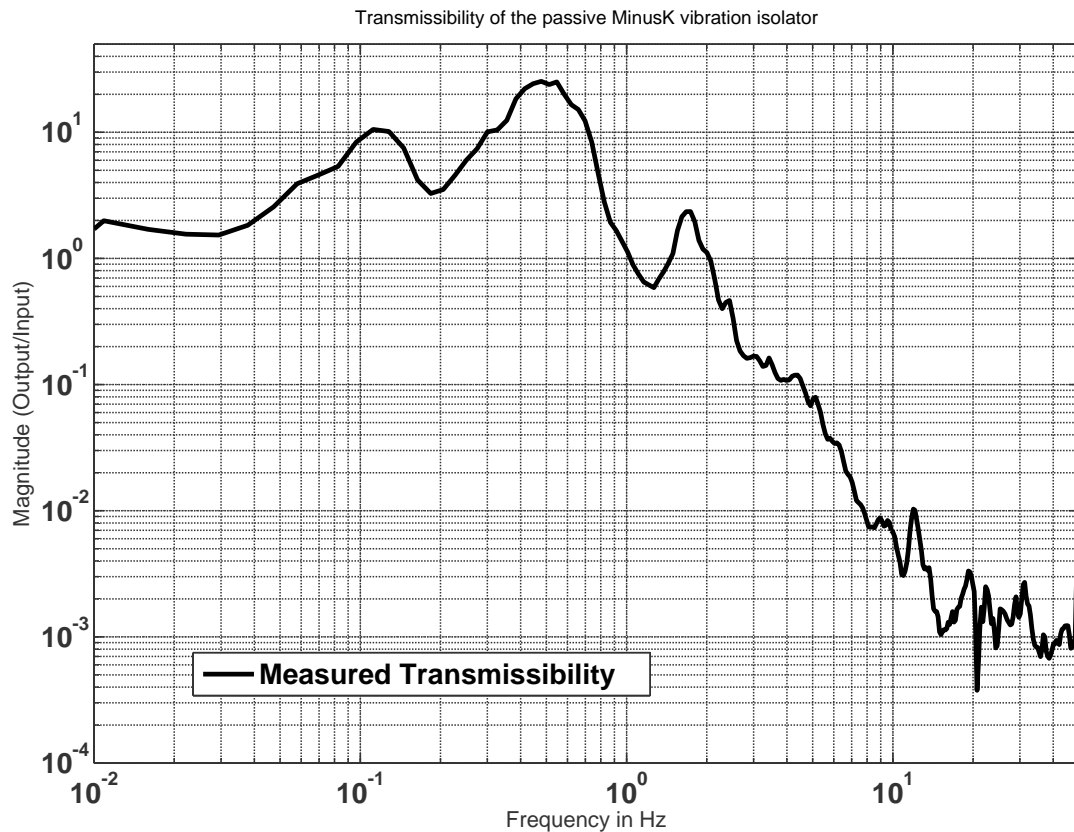


Figure 3.2: Measured performance of our spring-mass passive vibration isolator. Due to the small damping ratio the transmissibility declines proportionally to ω^{-2} as described in the text. The minor peaks at 0.15 Hz and 1.7 Hz are spurious and due to cross-coupling in the platform and the sensor.

sharp for systems with very little damping and becomes smaller and broader as the damping increases.

- For higher frequencies the system, will attenuate vibrations with a factor of ω^{-2} directly behind the resonance peak and with ω^{-1} further away from the resonance. The weaker the damping ratio, the further the ω^{-2} slope extends.

This simple model describes our vibration isolator reasonably well and resembles the measured and specified performance of the isolator. Figure 3.2 does not, however, correspond exactly to a plot of equation 3.2. The reason is that it was deduced by taking the ratio of the spectral densities on and off the platform. The input excitations are not normalized and can vary during the day e.g. due to changing activity in the laboratory. Tilt modes excited on the platform also couple into the spectrum, see section 3.1.3. For a reliable transmissibility measurement, a controlled ground base excitation in a well-defined direc-

tion has to be used. A similar measurement using voice coil actuators will be presented in section 3.4.1 and yields the expected results.

Since the presented model does not consider internal structural modes and hysteretic damping, minor deviation could be expected. They only play a role at higher frequencies, however, whereas the main concern of this work is isolation of low-frequency vibrations.

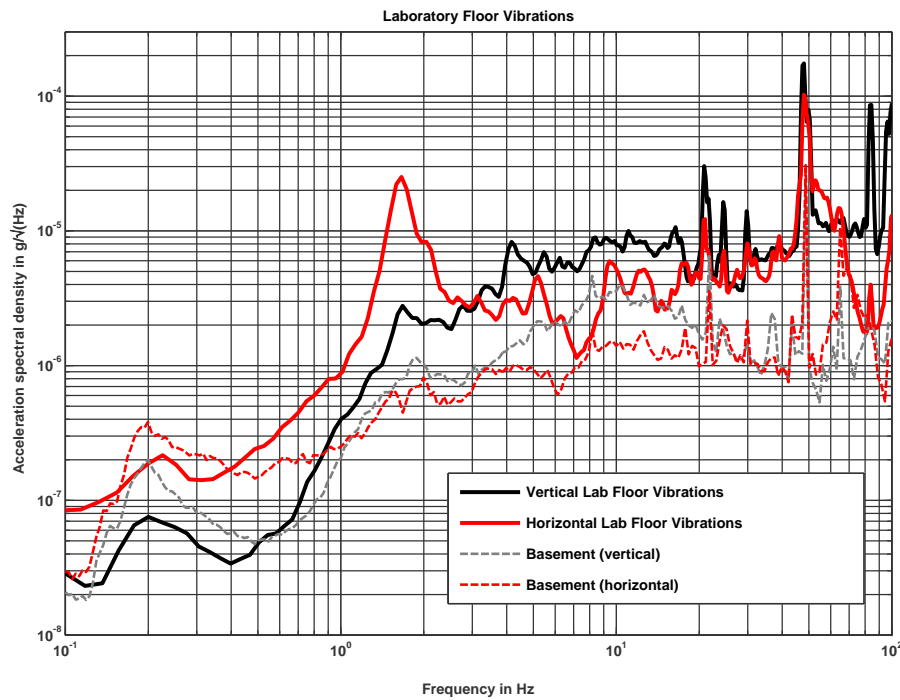


Figure 3.3: Vibration spectrum measured in the 8th floor of our building at Humboldt University in central Berlin. The dotted lines are spectra taken in the basement of the building. See table 3.1 for a list of known excitations visible in the spectrum

Source	Direction	Frequency
Micro-Seisms	Vertical and Horizontal	0.1 Hz to 0.5 Hz
Building Eigenmodes	Horizontal	1.7 Hz
Laboratory Floor	Vertical	approx. 20 Hz
Air Conditioning	Vertical and Horizontal	48 Hz

Table 3.1: Typical Vibration Sources in our Laboratory

When looking at the transmissibility, it is clear that passive vibration isolators can only isolate against ground motions at frequencies above their internal resonance frequency. To get an overview of the vibrations present in our laboratory, table 3.1 enlists some vibration sources we have identified in our lab. A plot of the acceleration spectral density measured on our lab floor at Humboldt University can be seen in figure 3.3. The most prominent

part of the spectrum ranges from frequencies of about 10 mHz to the mid-acoustic range at several hundreds of Hertz. Micro-seisms which are generated by ocean waves striking the continental plates typically occur at around 0.07 Hz and constitute the lowest frequency contribution [HPCI99]. Buildings typically have eigenmodes at frequencies ranging from 0.1 Hz to 2 Hz. In the eighth floor of the physics building the frequency is around 1.7 Hz and has been identified by taking vibration spectra at different places. A measurement from the basement, for example, has not been found to show any horizontal excitation at 1.7 Hz. The lab floor in this building oscillates at a frequency of about 20 Hz. Plenty of excitations also occur around 50 Hz. Our lab typically suffers vibrations at 48 Hz. We suspect they are induced by the air conditioning units since their DC motors typically oscillate at that frequency. Excitations from mechanical and electronic devices and human movements add a very broad contribution to the spectrum and can rarely be connected to a single frequency.

To isolate against all of these vibrations with a single passive vibration isolator, one would require a system with an internal resonance frequency of 0.07 Hz. A mechanical spring system with this resonance frequency would be prohibitively large, as it needs to support its payload against gravity. The natural resonance frequency is given by $f_0 = \frac{1}{2\pi} \sqrt{g/L}$. Here L is the extension of the spring and g is the acceleration due to gravity. A system with a 2 Hz resonance frequency would need a spring with about 6 cm. A system with a resonance frequency of 0.07 Hz, however, needs a prohibitively large spring with 50 m extension. The performance of a vertical vibration isolator is therefore limited by its dimension.

3.1.2 Tuning the Resonance Frequency with Negative Stiffness Elements

To improve the situation and provide a low natural frequency in a compact package, negative stiffness elements are part of the MinusK vibration isolator. Negative stiffness literally means that the stiffness k_n is a negative number. This has been realized using a horizontally loaded bar as illustrated in figure 3.4. The force exerted by this element according to Hooke's law $F = -k_z$ is therefore pointed in the direction of the extension of the element. If combined with a positive stiffness element k_p as shown in figure 3.4, the resulting system has an effective stiffness $k_{eff} = k_p + k_n$. Both contributions k_p and k_n can be tuned in the MinusK platform, which enables the isolator to reach a low total stiffness and a resulting resonance frequency of 0.5 Hz. When trying to lower the resonance frequency even further, the platform becomes unstable and drifts against its dynamic range limiters.

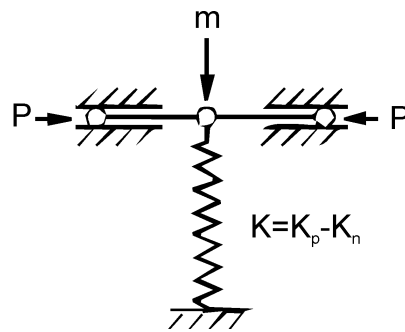


Figure 3.4: The principle of a negative stiffness vibration isolator. The payload with mass m is sitting on a conventional spring k_p . The negative stiffness is achieved by the horizontal bars under the load P . From [Pla93]

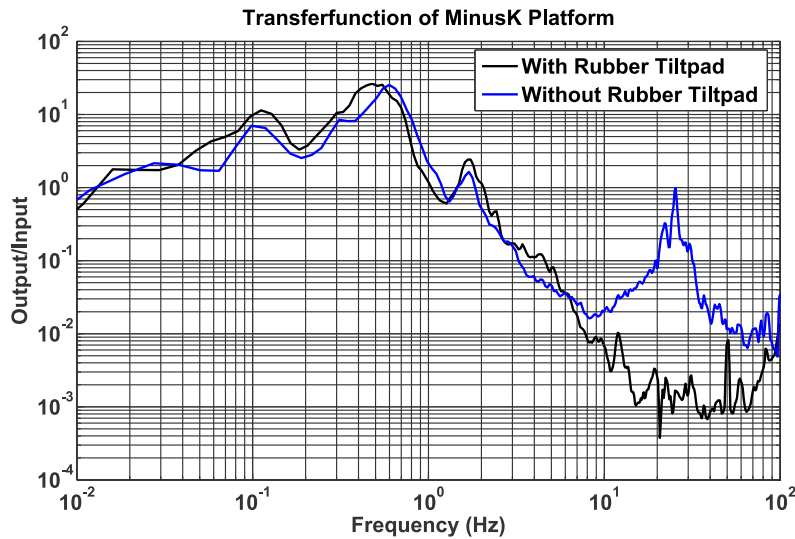


Figure 3.5: Tilt Mode at a frequency of 25 Hz with and without the compensating rubber tilt pad.

3.1.3 Isolator Tilt Motions

As shown in the blue line in figure 3.5, the platform shows an internal resonance at 25 Hz. We suspect that this is caused by tilt modes existing in the complex internal structure of the isolator platform. When left unaddressed, they severely compromise vibration isolation performance at this frequency.

To filter out this tilt mode, a soft rubber pad is placed between the vertical vibration isolator and the top plate in a central position. Due to its elasticity and small size in comparison to the top plate, only low frequency tilts can travel through the pad which, is therefore called "tilt pad" by the manufacturer.

At the low frequencies relevant to our atom interferometer, however, the tiltpad actually enhances tilt motions due to its own resonance peak. These low frequency tilt

motions effectively enter the gravity measurements of the atom interferometer as a systematic effect by misaligning the measurement axis. Therefore, we removed the tiltpad from the platform at first. The vibration isolation performance around 25 Hz decreased so far, however, that it was put back in to decrease vibration induced interferometer phase noise.

3.1.4 Horizontal Vibration Isolator

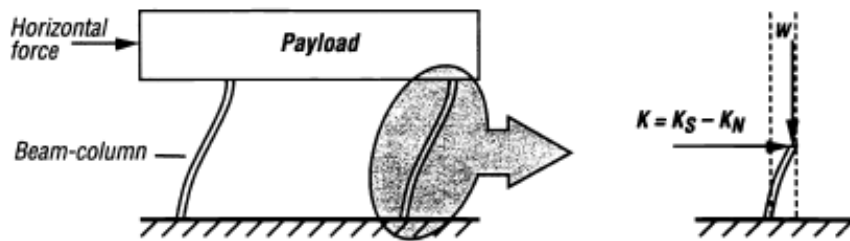


Figure 2 Horizontal-Motion Isolator

Figure 3.6: Inverted pendulum horizontal vibration isolator. from [Pla91]

Although the atom interferometer is mainly susceptible to vertical vibrations, the passive vibration isolator also features isolation against horizontal ground motions. The horizontal stage uses four columns in an inverted pendulum configuration as shown in figure 3.6. The horizontal resonance frequency can be tuned by adding or removing mass from the platform top plate. More weight on the platform will tune the system to lower the resonance frequency. Adding more and more weight eventually makes the isolator unstable which results in drifting towards the dynamic range limiters.

In the original configuration, the isolator could be tuned to a minimal horizontal resonance frequency of 1.5 Hz. As shown in figure 3.3, this coincides with a large excitation peak at 1.7 Hz in the horizontal spectrum taken in the 8th floor of our building. The coinciding resonance takes effect in a large horizontal excitation, which also coupled into vertical motions. To alleviate this undesirable effect, we requested weaker custom ground columns from the manufacturer, with a lower resonance frequency of 0.5 Hz. As shown in figure 3.7, the new columns greatly improve the situation and reach an attenuation of approximately a factor 6 at 1.7 Hz. The vertical spectrum no longer shows an excitation at this frequency, which indicates much smaller cross-coupling.

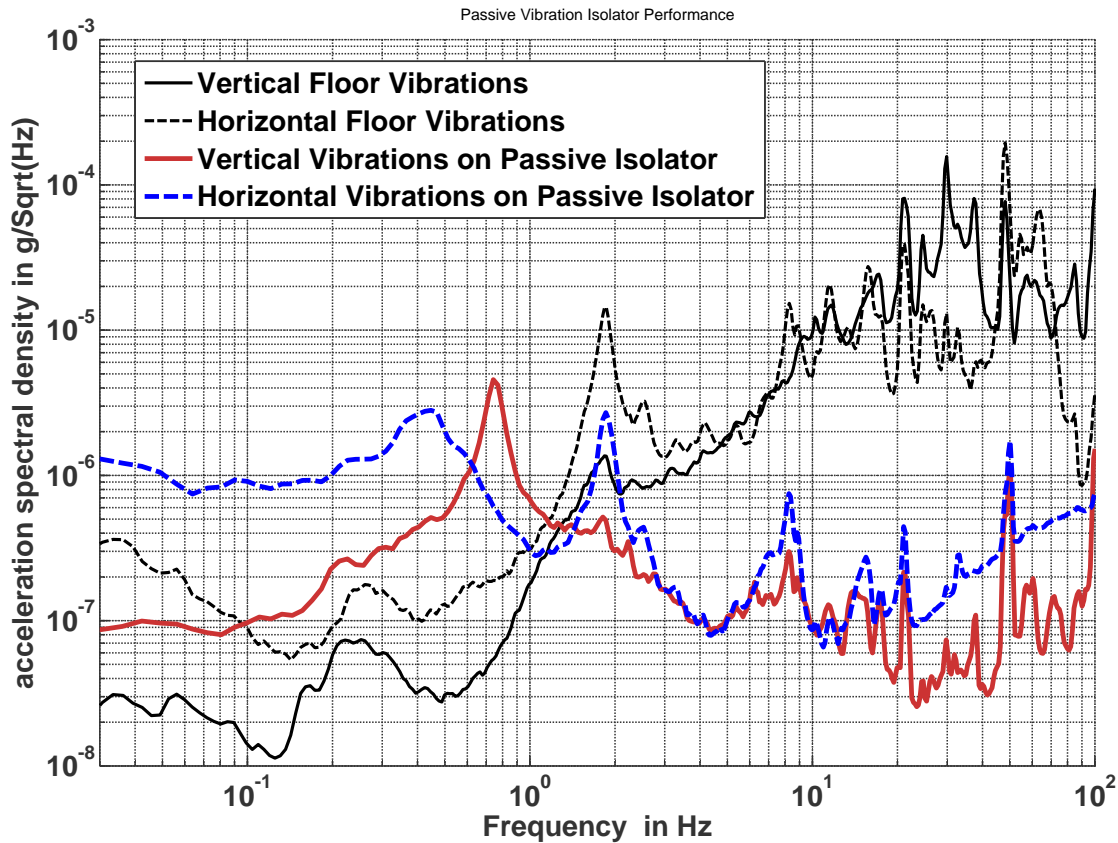


Figure 3.7: Performance of the passive vibration isolator in vertical (solid) and horizontal (dashed) directions. The vertical isolator is tuned to a resonance frequency of 0.75 Hz, the horizontal isolator to 0.45 Hz. The associated resonance peaks are clearly visible. Note the building wobble mode in horizontal peak direction at 1.7 Hz.

3.2 Theoretical Foundations of Active Vibration Isolation

As pointed out in section 3.1, the performance of the commercial passive vibration isolator is not sufficient to enable atom interferometry at long pulse separations. This limits the interferometer's sensitivity in measuring g . The active feedback system developed during this work eliminates this limitation and will be presented here. The performance gain is achieved by reducing the stiffness of the system and lowering the effective resonance frequency from 0.5 Hz to 0.025 Hz by exerting an additional force to the payload mass. The active system follows many ideas given in [HPCI99] and [Pet98] and adapts them to make the system fit into a smaller package and to be more easily usable. The feedback loop is implemented as shown in the block diagram 3.8. It measures the residual vibrations on the isolation platform, and feeds them back into the vibration isolator using voice coil actuators which exert a force between the platform base and its payload.

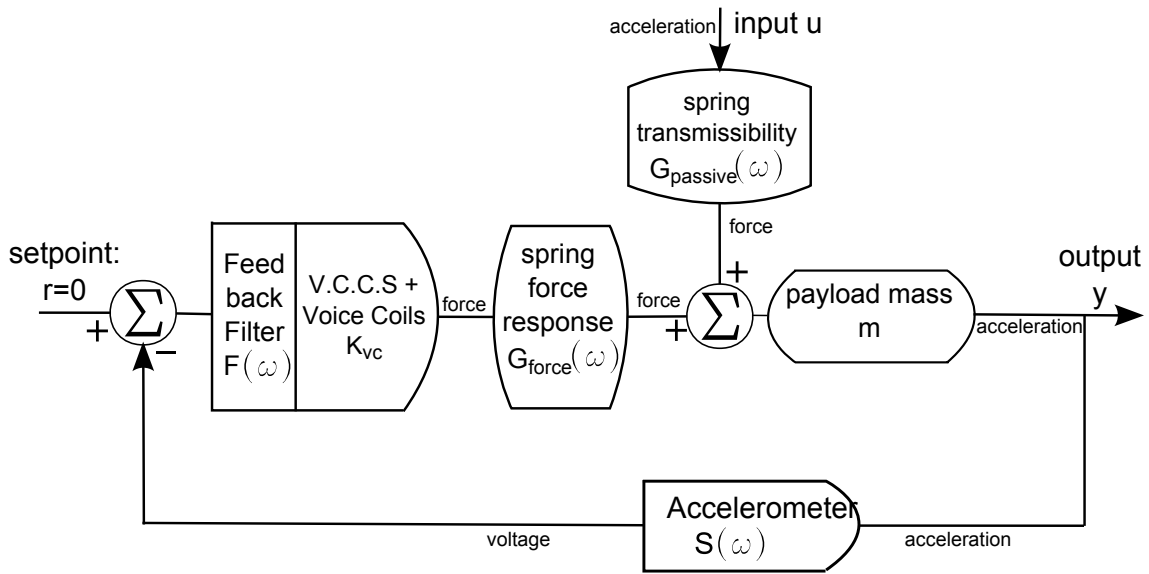


Figure 3.8: Feedbackloop for active vibration isolation. Mechanical components are shown in round boxes whereas electronic parts are squared

3.2.1 Open-Loop and Closed-Loop Transfer Function

To derive the effect of the feedback on the system, we reconsider the dynamic equation of the passive isolator. By adding a feedback force $F_a = -H\ddot{z}$ proportional to the residual acceleration on the isolator to the left side of equation 3.1, we end up with a slightly different transfer function:

$$G_{active}(\omega) = \frac{\ddot{z}}{\ddot{z}_g} = \frac{2(i\omega)\zeta_0\omega_0 + \omega_0^2}{-\omega^2(1 + H(\omega)) + 2(i\omega)\zeta_0\omega_0 + \omega_0^2} \quad (3.3)$$

This is the transfer function of the active system, also labeled closed-loop transfer function. It is shown in [HPCI99], that if the feedback gain H is a constant, the closed loop system will show a decreased resonance frequency but also less damping. To compensate for the loss of damping, a velocity term proportional to $1/\omega$ can be added to H . The resulting closed-loop system would show instabilities, however, due to the limited bandwidth of the accelerometer and other effects.

To fully understand the system and to make the feedback loop stable, stability criteria for $H(\omega)$ were derived by analyzing the frequency response of the open-loop transfer function. This has been coined “frequency response feedback design method”. We find the open-loop transfer function of the system by rearranging equation 3.3:

$$G_{active}(\omega) = \frac{\frac{2(i\omega)\zeta_0\omega_0 + \omega_0^2}{-\omega^2 + 2(i\omega)\zeta_0\omega_0 + \omega_0^2}}{1 + \frac{-\omega^2}{-\omega^2 + 2(i\omega)\zeta_0\omega_0 + \omega_0^2} H(\omega)} \quad (3.4)$$

$$G_{active}(\omega) = \frac{G_{passive}(\omega)}{1 + G_{force}(\omega)H(\omega)} \quad (3.5)$$

Several parts of equation 3.5 can be identified with independent parts of the feedback loop, and the same result could also have been derived using the block diagram shown in figure 3.8. $G_{passive}$ is the well-known transfer function of the passive vibration isolator as derived and measured in section 3.1. G_{force} is the transfer function from the voice-coil excitation to acceleration on the platform. Note that this is different from the platform transfer function from ground vibrations to isolator vibrations. It is derived and verified by a measurement in section 3.4.1. The feedback function $H(\omega)$ corresponds to the product of the various elements in the feedback path shown in the block diagram:

$$H(\omega) = mS(\omega)F(\omega)K_{vc} \quad (3.6)$$

m is the moving mass of the vibration isolator, $S(\omega)$ and $F(\omega)$ are the frequency responses of the accelerometer and feedback filter, and K_{vc} is the constant gain of the current source and voice coils. We can now write down the open-loop transfer function G_{ol} by looking at equation 3.5. A complete list of elements contributing to G_{ol} is shown in table 3.2.

$$G_{ol}(\omega) = G_{force}H(\omega) \quad (3.7)$$

Symbol	Element
$S(\omega)$	accelerometer gain and frequency response
$G_{force}(\omega)$	platform frequency response to voice coil excitation
K_{vc}	frequency response/gain of the voice coil actuator and its current source
$F(\omega)$	adjustable frequency response of the feedback filter

Table 3.2: Functional elements of the open-loop transfer function of the system shown in the block diagram 3.8

3.2.2 Frequency Response Design

As already pointed out, the frequency response design method provides criteria for the open-loop transfer function G_{ol} to provide a stable closed-loop system. An extensive treatment of this subject is given in [FPEN01]. Here, we will discuss the use of the Bode Plot to determine the gain- and phase margin by using an example. Bode plots generally show the magnitude versus frequency on a double logarithmic scale, and the phase response versus frequency on a simple logarithmic scale. Figure 3.9 shows the Bode Plot of an active vibration isolation with simple proportional feedback. In this case, the feedback force is proportional to the measured acceleration on the isolator, and the gain of the feedback filter $F(\omega)$ is constant. The open-loop magnitude response therefore resembles the platform excitation response $G_{force}(\omega)$ for most frequencies. It increases from low towards medium frequencies, shows a resonance peak at the platform resonance frequency, and then stays

at a constant value. The measurement bandwidth of the accelerometer extends from 0.0027 Hz to 100 Hz, outside of this bandwidth the open-loop response decreases due to filter elements internal to the sensor. The unity gain points, the points at which the

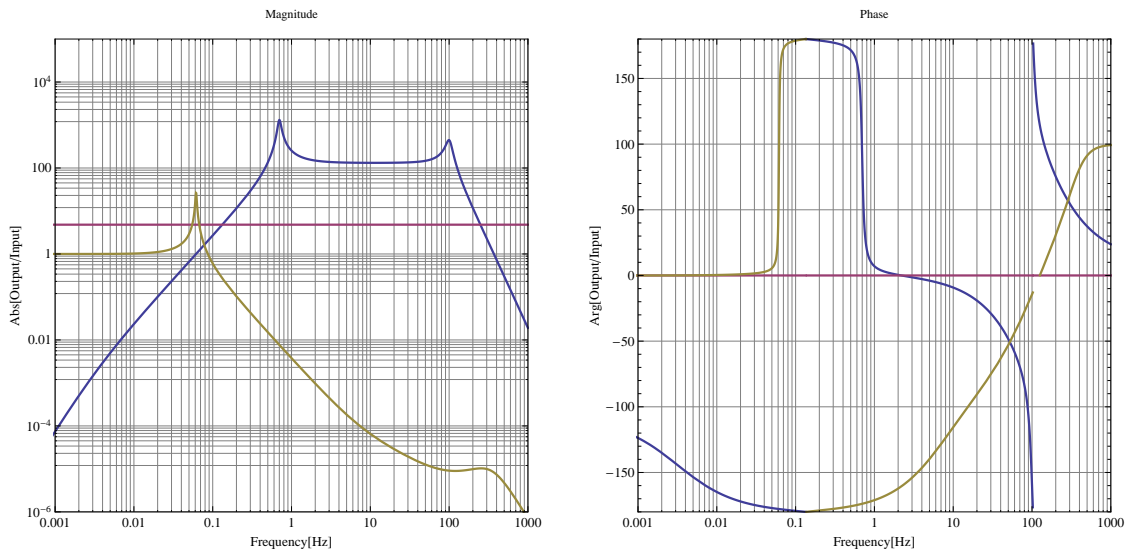


Figure 3.9: Instable active vibration isolation system shown as an exemplary Bode Plot. The feedback is flat and proportional to input acceleration. a) the blue line shows the open-loop transfer function $G_{ol}(f)$ b) the red line shows the constant feedback gain F c) The brown line shows the corresponding closed-loop frequency response $G_{active}(f)$. It indicates an under-damped system with a resonance frequency of 0.05 Hz. This system would NOT be stable in closed-loop operation due to the missing phase margin at the lower and upper unity gain point.

open-loop magnitude response crosses unity gain, are 0.1 Hz and 1000 Hz for the given feedback gain factor. The phase response at the unity gain points minus 180° gives the phase margin of the active system. The phase margin states how out of phase the feedback signal is with respect to the disturbance that is to be compensated for frequencies ω with $G_{ol} \geq 1$. A phase of 180° , or a phase margin of zero, states that the feedback signal is in phase with the disturbance which is then amplified. The phase margins in the Bode Plot shown in figure 3.9 are both smaller than 45° which means that this closed-loop system would be unstable.

3.2.3 Design of the Stable Feedback Filter

To increase the phase margin and ensure a stable closed-loop system, the feedback filter response $F(\omega)$ was customized through a choice of several additional filter elements. The goal of the design process is to make the proportional feedback as high as possible to lower the effective resonance frequency of the closed loop system without making the

system unstable. In addition, integral gain has to be provided to raise the damping ratio of the closed-loop system. Finally, to ensure stability the feedback path has to suppress frequencies outside of the sensor bandwidth and maintain a sufficient phase margin. These goals were achieved by using a high-pass filter and three lag-compensators as functional elements in the feedback filter.

To remove any residual offsets from the signal which survived the internal high-pass in the accelerometer, a high-pass element was also added to the filter. Its transfer-function is given by

$$H_{HP}(\omega) = K_{HP} \frac{i(\omega/\omega_{HP})}{i(\omega/\omega_{HP}) + 1} \quad (3.8)$$

with the corner frequency ω_{HP} and Gain K_{HP} . Its frequency response is flat for frequencies above ω_{HP} and decreases as $1/\omega$ for lower frequencies. A corner frequency of 1 mHz was chosen to eliminate residual signal offsets without reducing the feedback gain at low frequencies.

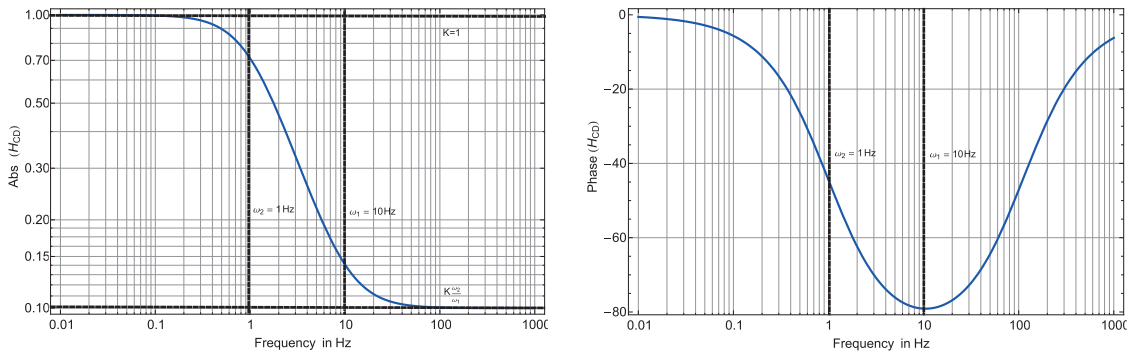


Figure 3.10: Transfer function of a Lag Compensator with parameters $K = 1$, $\omega_2 = 1Hz$, $\omega_1 = 10Hz$. Between ω_1 and ω_2 the gain decreases proportional to $1/\omega$ which is equivalent to an integrator. The phase dip around ω_1 has to be watched as it can decrease the phase margin and create instability of the closed loop system if ω_1 is too large.

Lag-compensators act as integrators in a limited frequency range and have a flat frequency response outside of this range. Their frequency response is shown in figure 3.10; it is given by:

$$H_{CD}(\omega) = K_{CD} \frac{i(\omega/\omega_1) + 1}{i(\omega/\omega_2) + 1} \quad (\omega_1 > \omega_2) \quad (3.9)$$

Their gain approaches a constant value of K_{CD} for $\omega \ll \omega_2$ and $K_{CD} \frac{\omega_2}{\omega_1}$ for $\omega \gg \omega_1$. Between ω_2 and ω_1 the slope is proportional to ω^{-1} , so the lag compensator there acts as an integrator.

To limit the system response at its resonance frequency and prevent it from running out of dynamic range, additional damping has to be applied to the active system. The lag compensator “lag1” has been added to the low-frequency part of the feedback loop for this

purpose. The integrator between its breakpoints creates a velocity dependent feedback force which provides additional viscous damping.

At higher frequencies beyond the resonance peak of the passive isolator, the open-loop frequency response has to fall off quickly enough to go below unity gain before the accelerometer runs out of bandwidth. This occurs at approximately 100 Hz. Two additional lag-compensators "Lag2" and Lag3" starting just beyond the resonance peak and extending to high frequencies have been added for this purpose. To reduce the associated phase dip (see figure 3.10) and conserve the phase margin, ω_1 of one lag compensator should end before the unity gain point. Based on the ideas described above and suggestions made

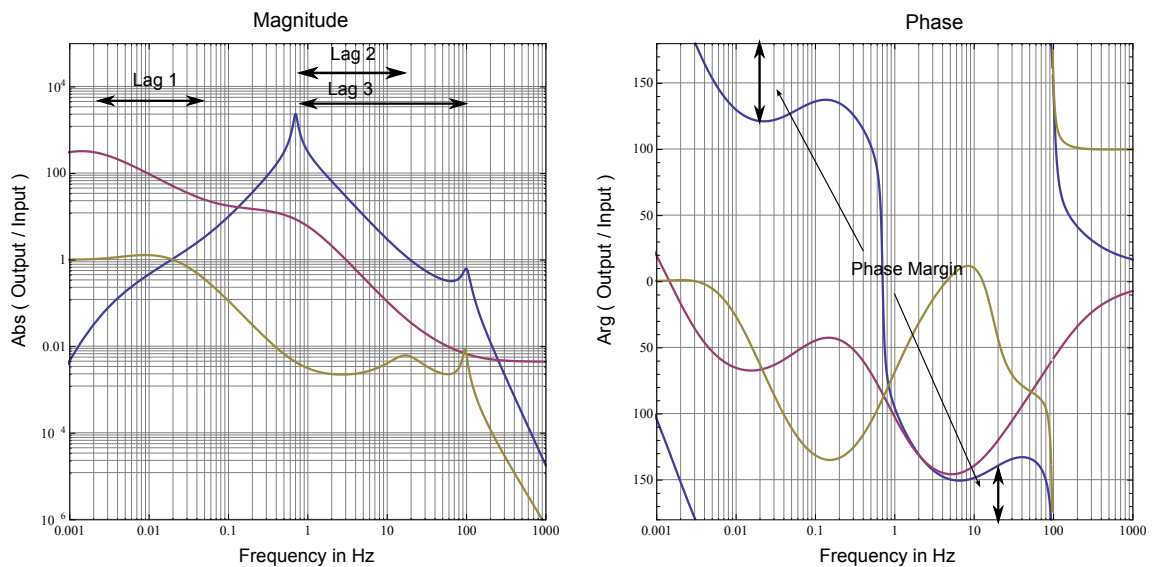


Figure 3.11: Predicted closed-loop and open-loop response with the customized feedback filter. a) Red: Frequency response of the feedback filter alone b) Blue: Open-loop frequency response including the platform response, the accelerometer, voice coil actuators and the feedback filter. c) Brown: Resulting closed loop frequency response. The filter element Lag 1 provides additional damping at low frequencies. Lag 2 and 3 ensure stability by bringing the unity gain point to lower frequencies and a phase margin large enough for a stable system.

in [HPCI99] we chose an initial set of parameters for the functional elements described above. To test the resulting open- and closed-loop response, the frequency response of the other elements in the feedback loop, listed in 3.2, was determined as described in section 3.3. The parameters were then optimized using the predicted closed-loop response. The result of that optimization is plotted in figure 3.11, the used parameter set is shown in table 3.3.

Element	Gain	f_1 in Hz	f_2 in Hz
Highpass	0.1	0.001	
Lag1	32	0.064	0.002
Lag2	50	20	0.8
Lag3	3	110	0.8

Table 3.3: Parameter Sets used for the feedback filter as shown in figure 3.11.

3.3 Implementation of the Active Vibration Isolation Setup

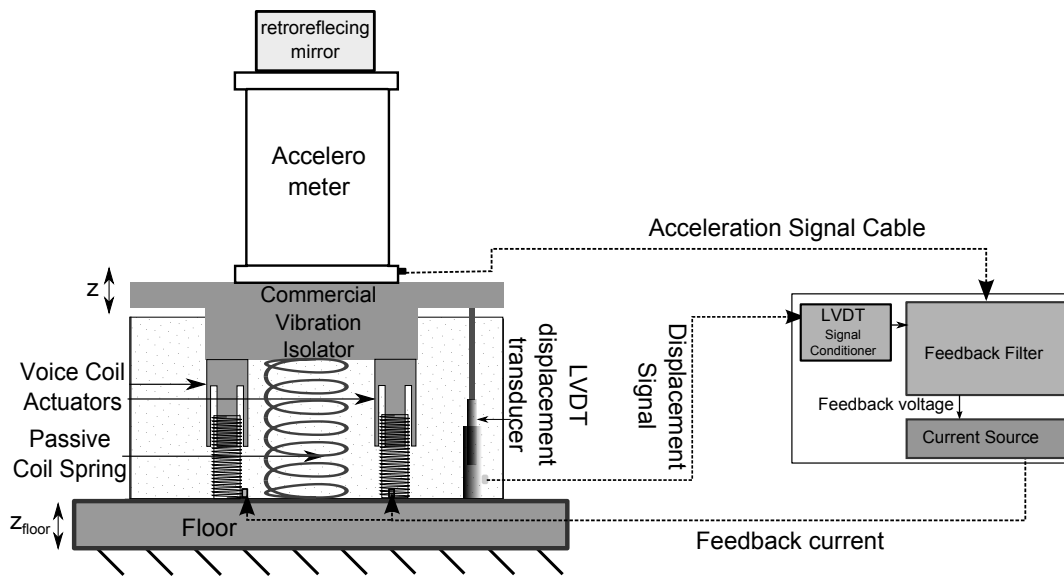


Figure 3.12: Active vibration isolator setup. Residual vibrations on the commercial vibration isolator are measured by the accelerometer and given to a digital feedback filter. The filters' voltage output is transformed to a proportional current and then output to two voice coil actuators which implement the feedback force.

Several modifications of the existing passive vibration isolation platform were performed, and new components were added to implement the active vibration isolation system. A schematic overview of the completed system is shown in figure 3.12. A detailed description of the performed modifications and the installed components will be given in this section.

3.3.1 Integrating the Voice Coil Actuators and LVDT Displacement Transducer

Implementing the feedback transducers into the passive isolator was challenging due to the compact design of the commercial platform. It was engineered to provide high-performance

Voice Coil Actuators

Voice coil actuators create a force by running a current through a solenoid, embedded in a magnetic field which is created by a permanent magnet. Due to an air gap between the moving coil and the magnet, the actuators do not create physical contact between the platform base and top plate in our bearing-less version. The bearing of the actuators is done by the passive vertical isolator system alone.

Due to size restrictions inside the vertical vibration isolator, small actuators manufactured by PBA with a diameter of 16 mm and a mid-stroke length of 31 mm were chosen. For symmetry reasons, and to avoid tilt excitation, the two actuators were arranged diagonally around the passive isolator's central coil spring. The maximum force required for active vibration isolation was also considered. The residual RMS acceleration in the frequency band from 0 Hz to 100 Hz can be assumed to be lower than $10^{-3}g$, compare figure 3.3. To cancel out this residual acceleration of a mass of 20 kg, a net force of 0.2 N is needed. The two voice coils chosen for our setup are capable of exerting a force of 6 N when given a current of 1.5 A, which is a force more than one order larger than needed.

LVDT Displacement Transducer

In addition to the voice coil actuators, an LVDT displacement transducer Solartron OP6 was integrated into the small space inside vertical isolator stage. It measures the current elongation of the vertical isolator within its dynamic range. It was originally intended to use the displacement signal to keep the active isolator from running out of dynamic range and reduce the effect of transient responses when switching on. Transients could become a problem since the active system has much less stiffness than the passive system. A very small force or acceleration can therefore lead to very large displacements of the isolator. This can be a problem when closing the feedback loop with an initial acceleration. The resulting transient response can make it very hard to switch on the system as reported in [HPCI99]. Our initial approach to tackle this problem was to reduce the feedback gain progressively when the isolator approaches the end of its dynamic range as indicated by the LVDT displacement transducer.

The LVDT functions using three solenoids. One central sending coil is excited by a 5 kHz AC voltage, two receiving coils at top and bottom of the sensor pick up the flux from the sending coil. A ferromagnetic core is connected to the moving mass and slides up and down through the sensor case. More of the magnetic flux reaches the top or bottom receiving coil, depending on the core position. A signal analyzer unit provides the excitation AC signal and determines the current sensor displacement analyzing the signal of the receiving coils.

Like the voice coil actuators, the sensor does not have any bearing and is only guided by the vertical isolator stage. An approximately 1 mm air gap between the transducer casing

and the moving core avoids friction and guarantees that the sensor does not decrease the performance of the vibration isolator.

After implementing the feedback loop it turned out, however, that transients were not a problem with our active system. This might be due to the negative stiffness mechanism, which shows strongly non-linear behavior as shown in a measurement in figure 3.17. The passive isolator on its own effectively makes the active system stiffer when it approaches its dynamic range limiters. For this reason, we do not use the displacement signal except for monitoring purposes. It could, however, still be useful for future improvement of the feedback loop design.

3.3.2 Accelerometer

The residual vibrations on the isolator platform are measured by an accelerometer. Since isolation of low frequency vibrations is particularly important for the atom interferometer, the measurement bandwidth of the sensor has to prolong to low frequencies in the order of 10 mHz. In order not to be limited by sensor noise, its self noise level must be well below the residual vibrations expected, considering the modeled closed-loop transfer function. Since active stabilization will only be implemented in the vertical direction, careful alignment and high rejection of cross talk from horizontal directions is required to keep them from coupling into the system.

We decided to purchase a customized force-feedback seismometer to meet all of the above mentioned requirements. This type of sensor is usually used to monitor weak seismological motions as part of a seismological network. It works with test mass connected to a spring with a single degree of freedom. The position of the test mass in the sensor is measure with a capacitative position sensor. A feedback loop with high gain counteracts deviations of the test mass from the center position by applying a force through a transducer coil. The test mass effectively does not move due to the high feedback gain. The current through the feedback transducer is proportional to the force necessary for compensating the acceleration and thereby proportional to the acceleration itself.

Our sensor is a Guralp CMG-3VL uni-axial force-feedback accelerometer. It features very little sensor noise, specified to be below the seismological signal observed at the quietest geological sites known. A specification of the sensor noise floor can be found in the appendix. The produced output is proportional to acceleration with a flat bandwidth extending from 0.0028 Hz to 100 Hz which covers all frequencies that are interesting for our application. The cross-coupling rejection is specified to be better than -65 dB.

We ordered a customized compact version, specialized for use in a laboratory environment, with the feedback electronics housed in a separate control unit to keep the sensor small. The sensor itself is housed in a cylindric mild steel casing.

3.3.3 Voltage Controlled Voltage Source and Voice Coil Actuators

The solenoids of the voice coil actuators possess an inductance L , which creates an additional frequency dependent term in the open-loop transfer function. The relationship between the voltage $u_{exc}(t)$ connected to the two poles of a solenoid and the solenoid current i_{sol} gives the result:

$$u_{exc}(t) = L \frac{di_{sol}(t)}{d(t)} \quad (3.10)$$

$$\Leftrightarrow I_{sol}(\omega) = \frac{1}{\omega L} U_{exc}(\omega) \quad (3.11)$$

The force exerted by the actuators will therefore decrease proportional to $1/\omega$. To avoid an additional compensating element in the feedback filter, the voice coil actuators are driven through a voltage controlled current source, denoted as V.C.C.S.. As its name suggests it drives a current proportional to the input voltage through the solenoid, corresponding to a flat response. It has a gain of 0.1 A/V in the current configuration which corresponds to a current of 1 A for the maximum output voltage of the D/A card. The bandwidth of the V.C.C.S. has been limited by an internal low-pass filter with a corner frequency of 1 kHz. This is still at least one order of magnitude faster than the fastest element of the feedback loop. The response can therefore be considered flat for the feedback design process.

A picture of the circuitry and a measurement of the V.C.C.S. transfer function is shown in the appendix.

3.3.4 Feedback Filter Electronics

The feedback filter described and modeled in section 3.2.3 was implemented as a digital filter to provide the required flexibility to tune the feedback parameters and to carry out additional tasks, e.g. logging. A National Instruments compactRIO Real-Time Computer System with an FPGA backplane was purchased for this purpose. All programs were written in NI Labview 2009, including the digital filter itself and a program for control- and logging purposes. The system is controlled remotely via Labview which allows easy access from the main control computer of the atom interferometer.

The program consists of the digital filter running on the FPGA chip and a control and monitoring program implemented on a 400 Mhz CPU which is also part of the cRIO system. To fit the system seamlessly into the rest of the atom interferometer setup, the cRIO system together with the V.C.C.S and the LVDT signal conditioner were mounted in a 19" subrack shown in figure 3.14.

Implementation of the IIR Filters

To implement the transfer functions of the high-pass and the lag-compensator from equation 3.8 and 3.9, they were transferred to the discrete z-plane by means of the Tustin

transformation. It is carried out using the substitution:

$$s = \frac{2z - 1}{Tz + 1} \quad (3.12)$$

T is the sample period, $s = i\omega$ is the position on the imaginary axis of the continuous s -plane and z is the position on the z -plane. See [FPEN01] for more information on the discretization of continuous system, the Z -Plane and the Tustin transformation. The resulting transformed version of the high-pass transfer function from equation 3.8 on page 34 is:

$$H_{HP}(z) = k_{HP} \frac{1 - z^{-1}}{(1 + \frac{T}{2}f_{HP}) + z^{-1}(\frac{T}{2}f_{HP} - 1)} \quad (3.13)$$

$$= k_{HP}a_{HP} \frac{1 - z^{-1}}{1 + b_{HP}z^{-1}} \quad (3.14)$$

With $a_{HP} = \frac{1}{1 + Tf_{HP}/2}$ and $b_{HP} = \frac{Tf_{HP}/2 - 1}{Tf_{HP}/2 + 1}$. The discrete lag compensator transfer function is:

$$H_{Lag}(z) = k \frac{f_2 \frac{Tf_1 + 2}{Tf_2 + 2} + z^{-1} \frac{Tf_1 - 2}{Tf_2 + 2}}{f_1 (1 + z^{-1} \frac{Tf_2 - 2}{Tf_2 + 2})} \quad (3.15)$$

$$=: g \frac{a + bz^{-1}}{1 + cz^{-1}} \quad (3.16)$$

These discrete transfer function can now be transformed to linear constant-coefficient difference equations in the discrete time domain by using the inverse z -transformation [FPEN01]. The results for the high-pass and the lag-compensator are:

$$u_{HP}(n) = K_{HP}a_{HP}(e(n) - e(n - 1)) - b_{HP}u(n - 1) \quad (3.17)$$

$$u(n)_{Lag} = gae(n) + gbe(n - 1) - cu(n - 1) \quad (3.18)$$

With the output $u(n)$ and input $e(n)$. The coefficients in equations 3.17 and 3.18 corresponding to the frequency response parameters from table 3.3 on page 36 are displayed in table 3.4. The resulting implementations have an infinite impulse response (IIR) due to their dependance on former output values $u(n - 1)$. These difference equations were implemented in Labview, corresponding to filter structure "the Direct-Form I". Since this filter-structure is prone to numerical instability due to rounding effects and because the FPGA only supports fixed-point arithmetics, care had to be taken to perform the filter operations with sufficient precision. This was achieved through close examination of the necessary fixed-point variable size at each point in the program.

Data Sampling and Logging

The FPGA samples the accelerometer signal with a rate of 1000 samples per second and a precision of 24 bits, and feeds this rate to the filter elements. The filter signal is then given

Element	Gain	a	b	c
Highpass	0.1	0.999997	-0.999994	
Lag1	1	1.00019	-0.999793	-0.999987
Lag2	2	1.06017	-0.934819	-0.994986
Lag3	0.02	1.3422	-0.652784	-0.994986

Table 3.4: IIR filter parameters used for the IIR filter as derived in equations 3.17 and 3.18 for the feedback filter configuration shown in table 3.3

out by an 16 bits analog output card at the same samplerate. For monitoring and logging purposes the FPGA also sends a down-sampled version with 100sps of the input and output channels to the cRIO controller CPU, which transmits the signal over an Ethernet connection to an SQL server. The data is stored on the server together with the rest of the information taken during an atom interferometer sequence. To avoid aliasing effects in the downsampled signal, it is first filtered by an FIR filter with a passband edge frequency of 40 Hz, a stop-band edge of 60 Hz and a stop-band attenuation of -80 dB. The data is then transferred into the controller's main memory via Direct Memory Access in order to be accessible by the CPU. The cRIO processor uses a datasocket connection to the main interferometer control computer which then saves the vibration data into the database together with the rest of the interferometer sequence measurements.

3.4 System Validation and Adjustment

After completing the modification of the commercial vibration isolator and implementing the rest of the feedback loop, the performance of the individual components was verified experimentally. This includes measurements of:

- the frequency response of the passive vibration isolator to a voice coil excitation using a network analyzer to validated the harmonic oscillator model.
- the frequency response of the digital feedback filter
- nonlinearities and hysteresis effects of the passive isolator due to the negative stiffness elements.
- the cross-coupling rejection of the accelerometer

3.4.1 Platform Excitation Response Measurement

In contrary to what might be expected at first glance, the frequency response $F_{force}(\omega)$ of the passive isolator to a force exerted by the actuators is different from its transmission

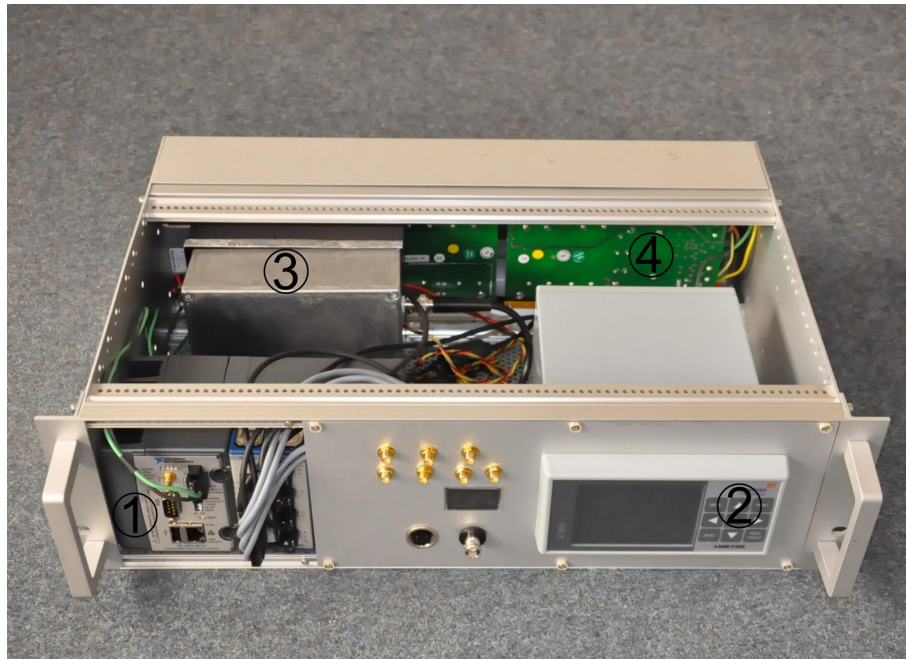


Figure 3.14: A 19" Subrack houses all external components of the active vibration isolation. The components are 1) the cRIO controller with analog input and output channels, 2) the LVDT signal conditioning unit, 3) V.C.C.S. to feed the voice coils 4) one $\pm 15V$ and one $+24V$ power source for all components of the feedback loop. See figure 3.12 for a schematic overview of the internal connections.

of ground base accelerations. It was deduced in section 3.2.1, equation 3.5. The transfer function from voice coil force \tilde{F}_{vc} to acceleration \tilde{a} on the platform is given by:

$$G_{force}(\omega) = \frac{-\omega^2}{-\omega^2 + 2\omega_0\zeta(i\omega) + \omega_0^2} \quad (3.19)$$

The predicted frequency response was measured in a sine sweep measurement. A HP3562A spectrum analyzer outputs a varying frequency to the V.C.C.S. and takes accelerometer signal as input. A plot of the predicted and measured frequency response is shown in figure 3.15. They agree very well up to a frequency of about 50 Hz. At higher frequencies, the rubber tilt pad in the passive isolator shows a second resonance peak at roughly 100 Hz. The purpose of the measurement was to verify the response of the negative-stiffness isolator. Therefore, the tilt-pad was not included in the model and its resonance is not predicted in the model. It was verified, however, that it vanished as expected when taking the tilt-pad out of the isolator.

The good agreement at low frequencies shows that the simple model of an oscillator with viscous damping is justified for the passive isolator.

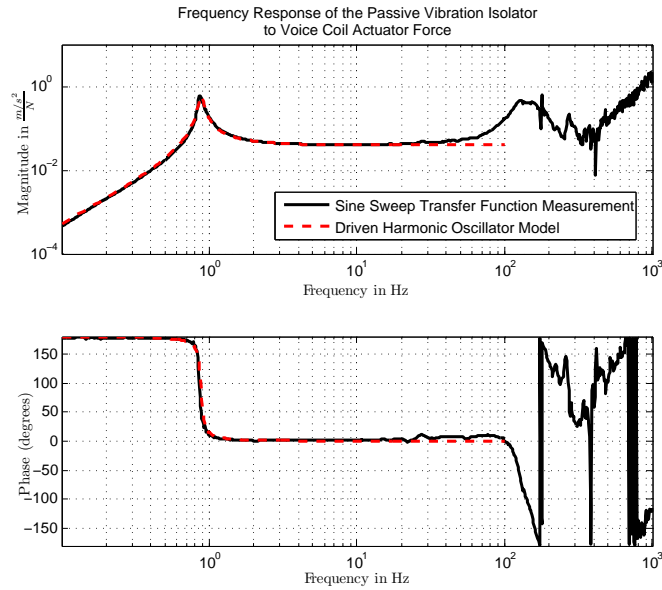


Figure 3.15: Frequency Response of the passive vibration isolator to a force exerted by the voice coil actuators as described in Equation 3.19. The fitted values of the damping ratio and resonance frequency were $\zeta = 0.03$ and $f_0 = 0.88$

3.4.2 Frequency Response of the Digital Feedback Filter

To verify that the intended frequency response is indeed realized by the feedback filter, its response has also been measured using the sine-sweep measurement mode of a HP spectrum analyzer. A Bode plot of the filter has been obtained whose magnitude part is shown in figure 3.16. As expected, the measured magnitude response resembles the desired frequency response very well.

3.4.3 Nonlinearities and Hysteresis Effects

Stability criteria for feedback control are only valid if the underlying dynamic system is linear and time-invariant. The negative-stiffness element of the passive vibration isolator, however, potentially contributes significant nonlinearities to the system. These nonlinearities were studied to check the feasibility of a stable closed-loop system.

Due to the nonlinear behavior of the negative stiffness element, the stiffness of the platform increases as it travels away from the central position towards its dynamic range limiters. In passive operation, the platform only moves a couple of micrometers and the effect is negligible. With the feedback loop closed, however, the stiffness of the system is greatly reduced. The platform then travels away from its middle position by 1 mm or more in normal operation, which is significant compared to the dynamic range of about 6 mm. We measured the stiffness change by deflecting the platform from its middle position using the voice coil actuators.

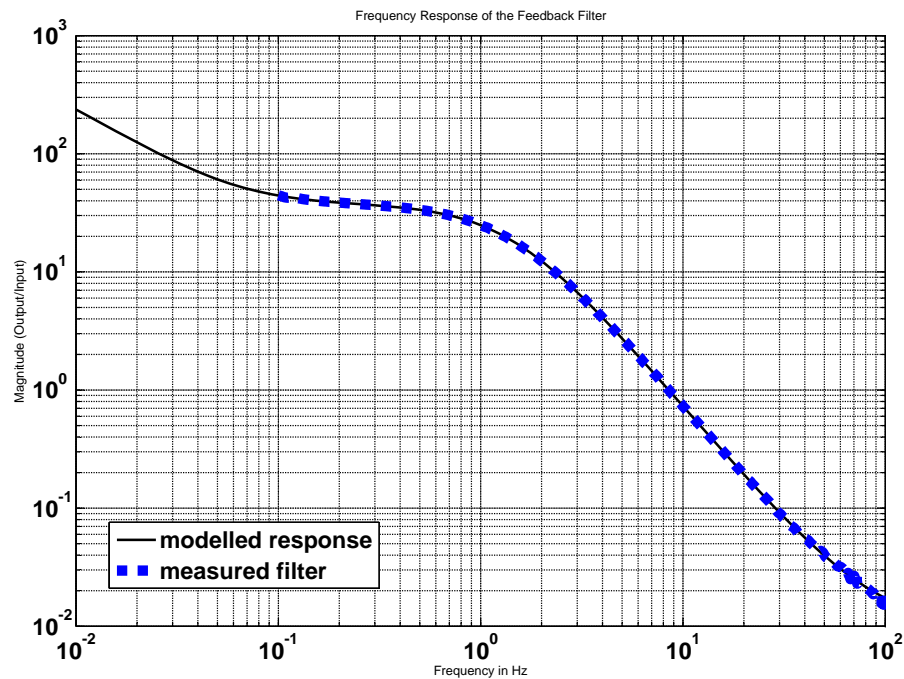


Figure 3.16: Frequency response of the feedback filter. The blue dashed line shows the measured response and agrees very well with the underlying model.

The result of the measurement is shown in figure 3.17. It shows the physical extension of the platform from its middle position plotted versus the external force exerted by the voice coils. When tuned to the lowest possible resonance frequency of 0.5 Hz, the platform shows a progressive stiffness increase and significant hysteresis effects. The strength of the nonlinearity decreases when the passive platform is tuned to higher resonance frequencies than 0.5 Hz and is almost completely eliminated at 0.9 Hz. To find a compromise between good passive vibration isolation performance and small nonlinear effects, we tuned the passive isolator to a frequency of 0.7 Hz when using the active vibration isolation.

3.4.4 Position and Alignment of the Accelerometer

Correct alignment of the accelerometer axis is a critical issue for a one axis feedback loop like in our system since it introduces cross coupling between the vibration axes. The sensor's internal cross coupling rejection is specified as -65 dB. The measurement axis perpendicular to which the rejection takes place, however, does not necessarily coincide to the physical axis of the sensor casing, as illustrated in figure 3.18. It is therefore not sufficient to align the sensor body with enough precision. We tackled the problem by determining the exact orientation of the sensor axis. Two possible methods were used to perform this measurement.

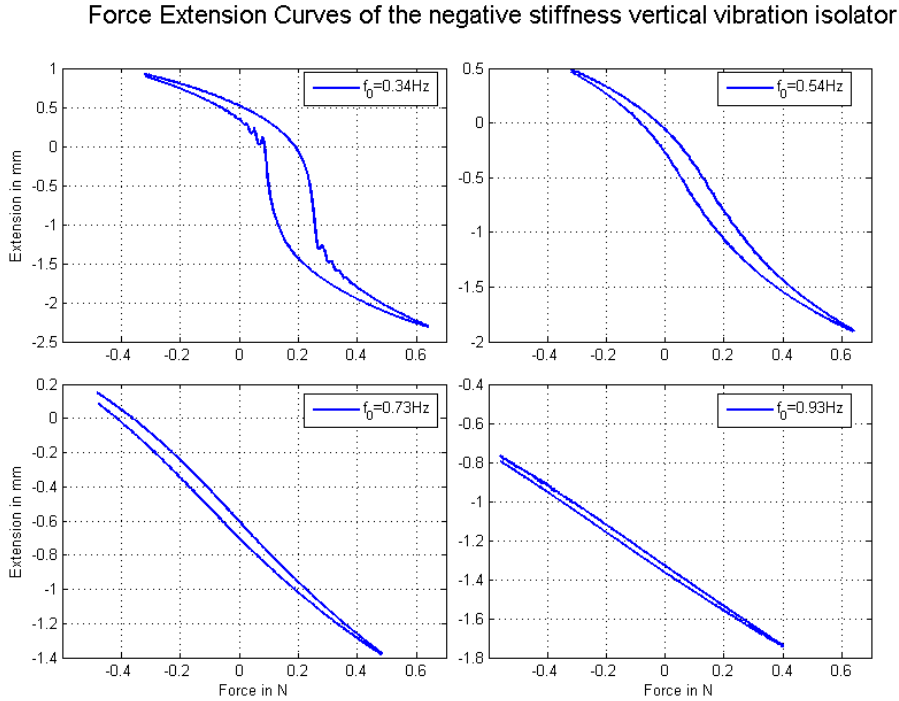


Figure 3.17: Force extension curve of the negative stiffness mechanism vertical vibration isolator. If the isolator is tuned to a resonance frequency lower than $f_0 = 0.7Hz$, it shows a strongly nonlinear behavior due to the negative stiffness element and hysteresis effects. Tuning to higher resonance frequencies diminishes the effect off the negative stiffness elements and yields a more predictable behavior.

Sensor Alignment Measurement by Vertical DC Acceleration

To determine and verify correct sensor alignment, we first made use of an auxiliary output of the accelerometer called mass position. This output is proportional to acceleration at very low frequencies and DC. To determine the correct measuring axis, the sensor was tilted and the DC output was monitored. As the angle α between gravity axis and sensor axis increases, the sensor output decreases with:

$$\cos \alpha \cong 1 - \alpha^2 \quad (3.20)$$

The alignment can therefore be optimized by maximizing the mass position output. The result of this measurement is shown in figure 3.19. It shows the DC output of the accelerometer versus the tilt shown on the x-axis. The tilt was measured using an electronic tilt sensor. Due to a possible offset of the tilt-sensor casing, the origin of the x-axis could be shifted by as much as 5 mrad.

The offset parallel to the x-axis has a value of 6 mrad which could be explained by measurement noise and a tilt sensor offset. The parabola on the y-axis has a tilt offset of 18 mrad, which is very large considering that the sensor is specified to provide excellent

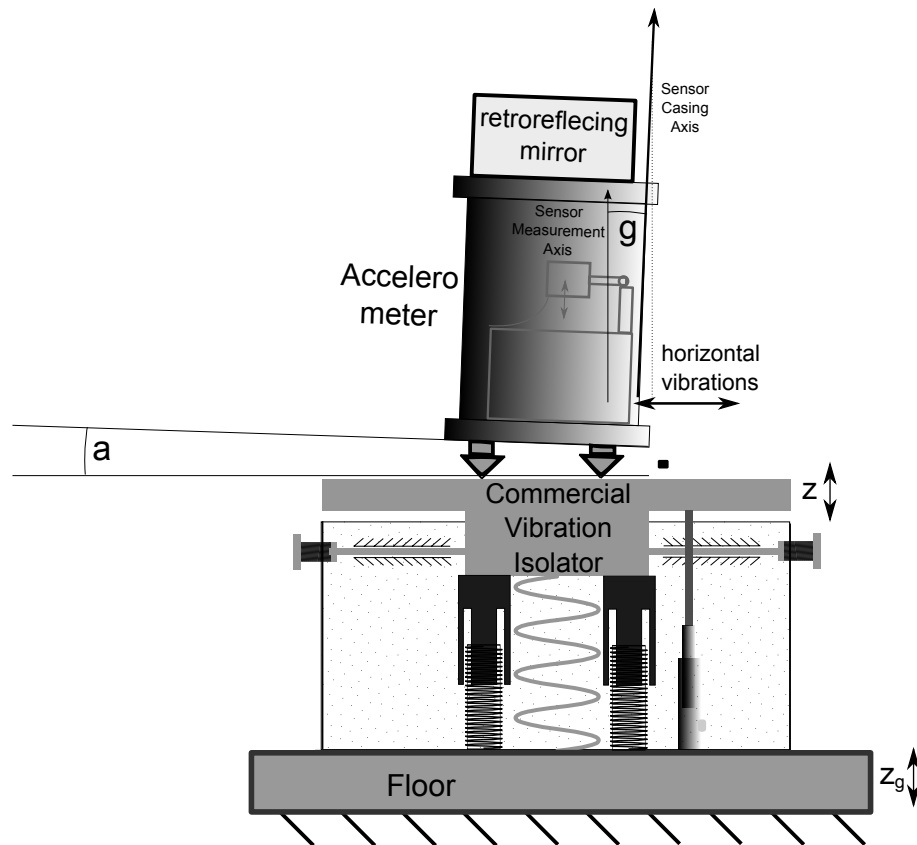


Figure 3.18: Cross coupling between vibration directions can occur due to misalignment of the accelerometer. Note that the sensitive axis of the sensor does not necessarily coincide with the outer axis of the instrument.

alignment properties and cross-coupling rejection. This can only be explained by either a flaw of the mass position output or an internal defect inside the sensor.

Sensor Alignment Measurement by Direct Horizontal Excitation

To exclude the possibility that the mass position output did not indicate the sensor alignment correctly, we measured the sensor cross-coupling in a second measurement. It was performed by directly creating horizontal acceleration in a controlled manner and monitoring the resulting cross-talk in the vertical sensor. If correct alignment was performed, any signal arriving in the vertical measuring axis should vanish within the limits of the sensor's cross coupling rejection.

For this idea to work, it is crucial that the movement is friction-less and purely horizontal. This was ensured by using a high precision air-floated turntable which has been used for a modern modern Michelson-Morley experiment in our research group [HSM⁺09]. The axis of rotation of the table is aligned with gravity to better than 100 μrad . This implies a cross-talk between horizontal and vertical movement of 10^{-4} , well below the specified

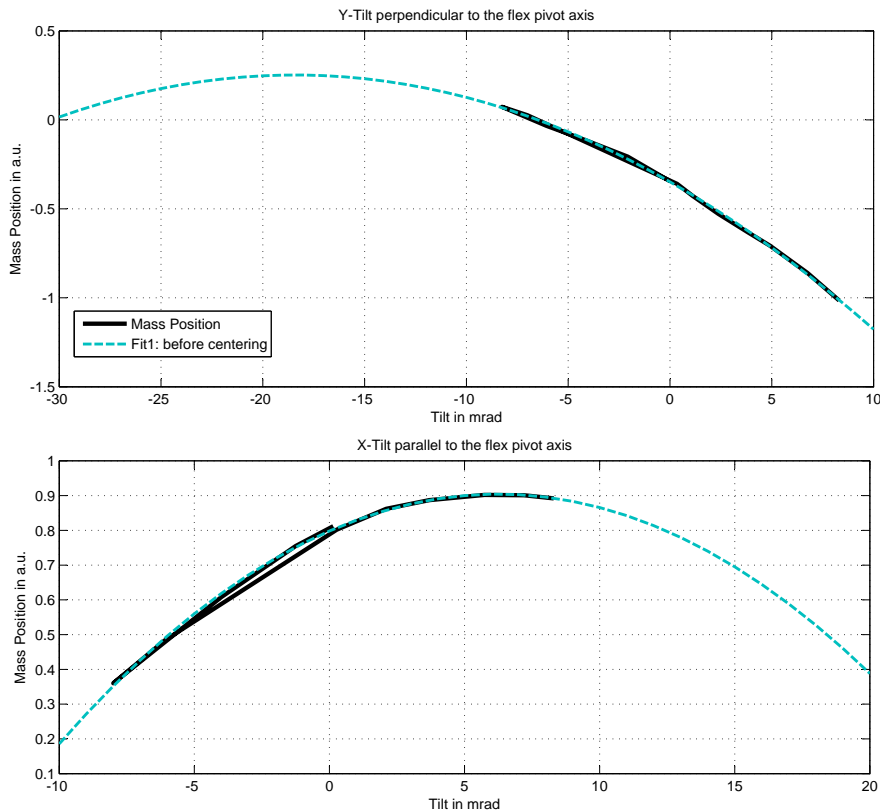


Figure 3.19: DC acceleration signal versus sensor tilt in two dimensions. The maximum value occurs at a x-axis tilt of 6 mrad and a y-tilt of -18 mrad . The offset on the y-axis is very large and can only be explained by an internal sensor misalignment or error. The flex-pivot mentioned in the plot titles is the internal joint of the acceleration sensor and is mentioned to be able to assign the axis to the sensor.

cross-talk of our sensor. A well-defined acceleration was created using springs connected to the laboratory walls. After an initial excitation, the turn-table swung back and forth with a period of $T_0 = 3.4$ s. The movement was monitored using a signal provided by the table. Using this setup, the cross-coupling coefficient was determined in terms of the transfer-function magnitude between table acceleration and sensor signal at the oscillation frequency T_0 .

The result is shown in figure 3.20. As in the previous measurement the sensor showed significant cross-coupling on the y-axis direction when standing upright. As the red line indicates, the measurement axis is tilted by -18 mrad with respect to the sensor case. This confirms that the sensor has either been assembled without appropriate precision or that a defect exists inside the sensor. The manufacturer of the instrument was therefore contacted and a sensor defect was confirmed. The sensor has been shipped back was not available for final measurements at the end of this work. Several improvements such as

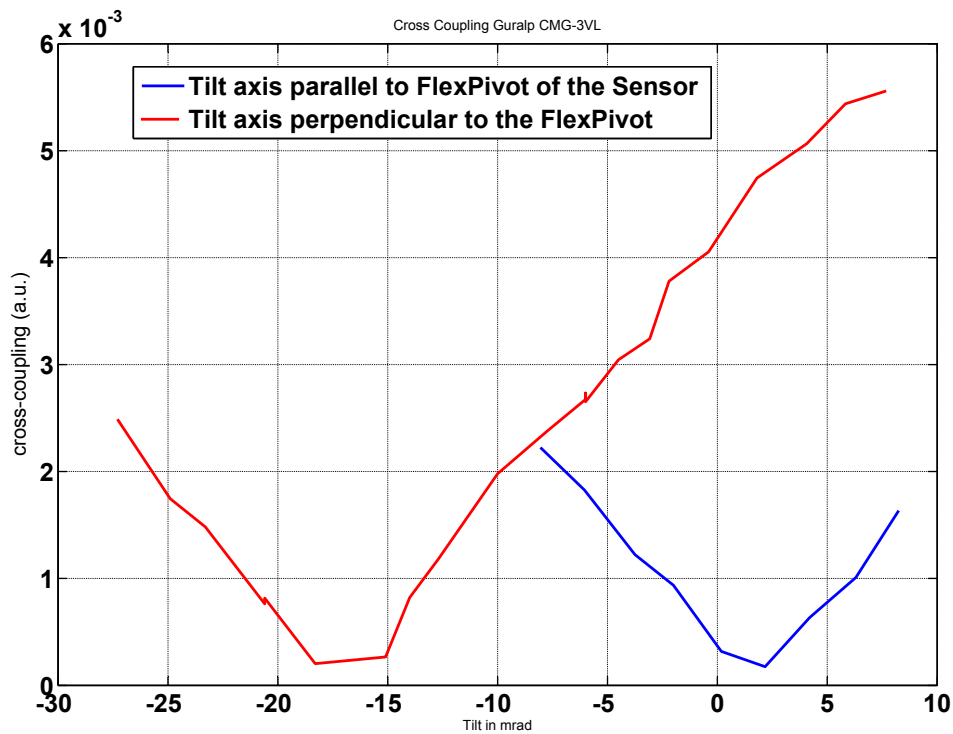


Figure 3.20: Cross coupling efficiency of the CMG-3 accelerometer versus sensor housing tilt.

the correction of an error in the feedback filter response can therefore not be presented here.

Accelerometer Position and Tilt Coupling

The absolute position of the accelerometer on the vibration isolator also plays an important role for the performance of the active vibration isolator because of tilt modes. If the accelerometer has a horizontal offset from the tilt axis, it will register a spurious signal and couple it into unwanted vertical motion. It is therefore crucial to position the internal sensor of the accelerometer directly above the tilt axis. To determine the optimal position of accelerometer on the vibration isolator platform, the exact position of the sensor inside the accelerometer was measured. This was done by putting the sensor on a rocker board and tilting it back and forth around a well-defined axis. The vertical sensor signal then shows a linear relation to the distance between sensor and tilt axis and can be minimized. Concluding from this measurement, the cross-coupling turns out to be lowest if the sensor casing sits centrally above the center of the vibration isolator platform. The most balanced and symmetric position is, therefore, also the best in terms of cross-coupling.

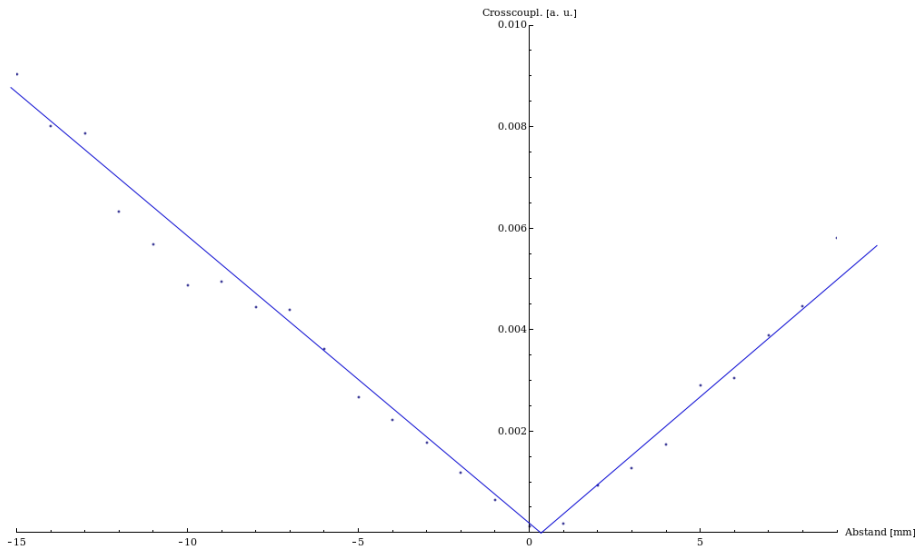


Figure 3.21: Cross coupling of tilt motions into vertical acceleration depending on the sensor position on the rocker board.

3.5 Results and Discussion

Figure 3.22 shows the spectrum of residual vertical vibrations on top of the active vibration isolation platform and figure 3.23 shows the corresponding transmissibility of the active platform. Two separate measurements are displayed, one taken using the error signal of the sensor inside the feedback loop and the second measurement taken by an additional independent sensor. Since both show significant differences and are subject to different disturbances, they will be discussed separately in this chapter.

3.5.1 Feedback Sensor Error Signal

The feedback sensor spectrum in figure 3.22 indicates a slightly under-damped system with a resonance frequency of about 0.03 Hz, which was confirmed by the transient response of the system. Behind the resonance peak the spectrum falls off sharply until it reaches the sensor noise floor at about $4 \times 10^{-9} \text{ g}/\sqrt{\text{Hz}}$. Between 0.8 Hz and 8 Hz the spectrum rises again to approx. $1 \times 10^{-7} \text{ g}/\sqrt{\text{Hz}}$ with the same slope as the floor spectrum. This is probably due to the decreasing suppression efficiency also shown in figure 3.11. Due to the anti-aliasing low-pass filter with 10 Hz corner frequency built into the data-logger as described in section 3.3.4, the spectrum rapidly decreases for higher frequencies.

If the preliminary model presented in section 3.2.3 holds true, the transmissibility measured by the feedback sensor should resemble the modeled closed-loop transfer function shown in figure 3.11. Due to an error in the implementation of the feedback filter response, the actual closed-loop response of the system changed. The black dotted line in figure

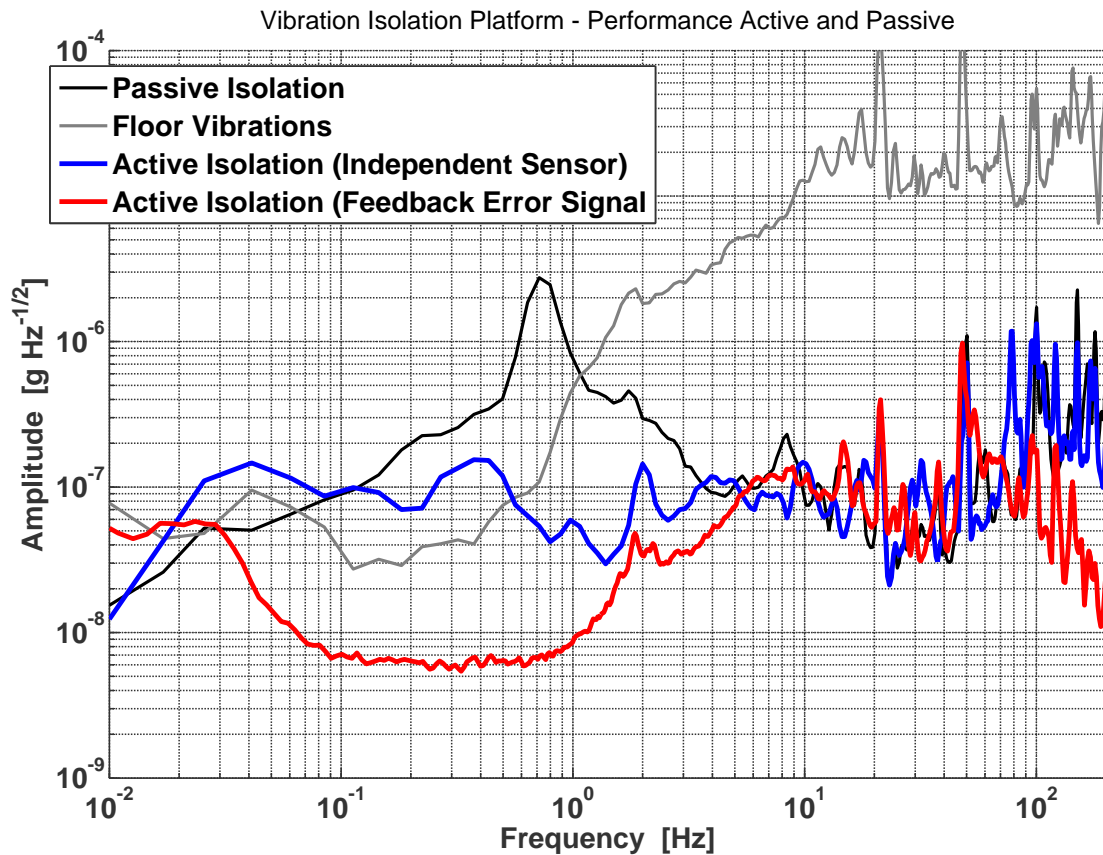


Figure 3.22: Residual vibrations measured on the active vibration isolator platform. The black and grey lines show the vibrations present on the passive isolator and the floor for comparison. The red and blue lines show residual vibrations on the active platform and show that the system significantly decreases residual vibration between 0.03 Hz and 20 Hz.

3.23 shows the expected closed-loop response when taking the implementation error into account.

The measured system shows the expected resonance frequency of about 0.02 Hz which is in agreement with the model. It also shows a small resonance peak which indicates a slightly under-damped system, which was confirmed by the system's transient response. The slope behind the resonance peak is also in agreement with the model, except of a frequency range between 0.1 Hz and 1 Hz where the measured transfer function is about one order of magnitude larger. This is probably due to the relatively broad resonance of the horizontal vibration isolator at 0.5 Hz. Due to the cross-coupling of the faulty feedback sensor, it is coupled into the vertical spectrum and therefore appears in the transfer function. Between 1 Hz and 10 Hz, the measured transfer function agrees with the model again.

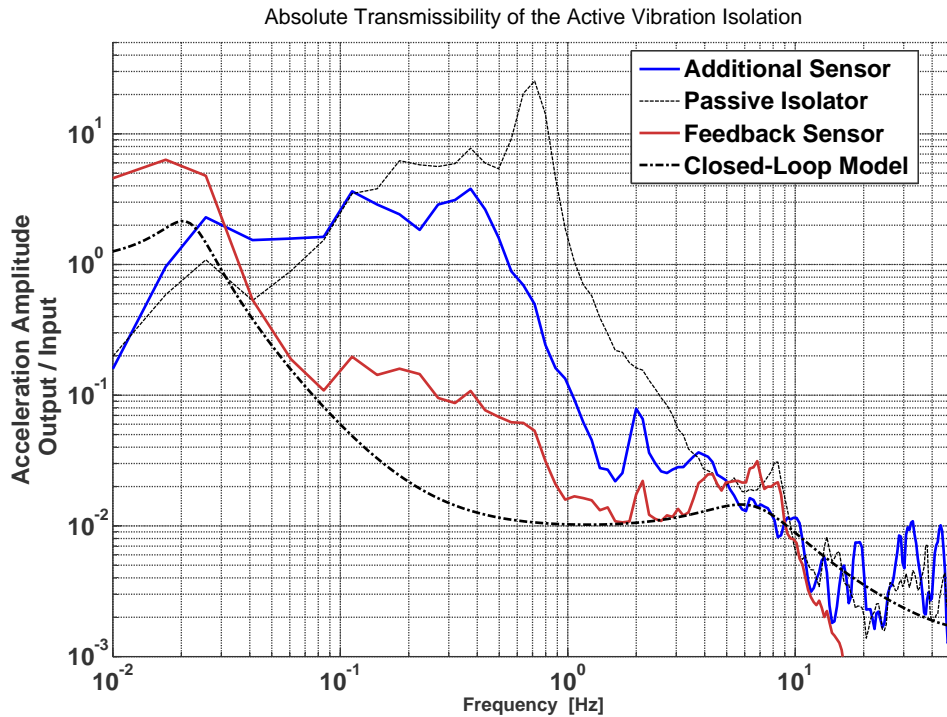


Figure 3.23: Transmissibility of the active vibration isolator measured with the feedback sensor error signal (red) and with an additional independent sensor (blue). The black line shows the measured transmissibility of the passive vibration isolation platform.

Since the input and output data of the shown transfer function were taken at a different time and the measured vibration spectra are not constant due to changing activities in the immediate surroundings, the shown measurement is subject to deviations. Additionally, the input spectra had to be taken with a different sensor subject to considerable directional cross-coupling. This makes it difficult to identify single features of the transfer function measurement. The general shape of the closed-loop transfer function should, however, be in agreement with this measurement. This shows that the active vibration isolator works as expected despite showing internal cross-coupling.

3.5.2 Measurements by the Additional Sensor

Sensor cross-coupling due to misalignment and tilt motions are not visible in the feedback sensor error signal shown in figure 3.22, and are only partly identifiable in figure 3.23. Therefore we measured the residual vibrations on the active isolator platform with a second independent sensor. The results are shown by the blue line in figures 3.22 and 3.23.

The resulting spectrum looks very different from the internal sensor spectrum which indicates that cross-coupling is indeed present in the system. The spectrum stays on a roughly constant value of $1 \times 10^{-7} \text{ g}/\sqrt{\text{Hz}}$ between 0.03 Hz and 0.5 Hz. This is more than one order of magnitude higher than the feedback sensor spectrum. Between 0.5 Hz and 1.5 Hz it shortly dips to $3 \times 10^{-8} \text{ g}/\sqrt{\text{Hz}}$ and then shows a peak again at 2 Hz. Between 2 Hz and 8 Hz the spectrum approaches the spectrum taken on the passive vibration isolator and is practically identical to it above 10 Hz.

The measurement shows that the feedback control bandwidth ends around 10 Hz which is in agreement with our theoretical model. The peaks in the spectrum at 2 Hz and 0.4 Hz correspond to typical horizontal excitations caused by the building and the horizontal vibration isolation. We therefore assume that crosstalk from the horizontal directions takes place either inside the independent second sensor or in the feedback loop. If the latter is the case this obviously decreases the performance of the active vibration isolator. Since we found significant crosstalk in the Guralp CMG-3 feedback sensor as described in chapter 3.4.4, we assume that at least some of the crosstalk happens inside the feedback loop. It should be noted, however, that the second sensor used for the independent measurement is very prone to cross-coupling between the horizontal and vertical directions as well. The shown measurement is therefore not entirely reliable. A third sensor with low internal cross-coupling would be required for this purpose. Although we do not have access to a third accelerometer featuring low internal cross-coupling, the increase in sensitivity of the atom interferometer is a strong indicator that the performance of the system is significantly better than represented by the blue line in figure 3.22.

3.5.3 Conclusion and Outlook

Figures 3.22 and 3.11 indicate that an active vibration isolation system was successfully implemented. This is supported by the greatly improved atom interferometer fringes at long pulse separations T . Consequently the sensitivity of the interferometer gravity measurements was improved by two orders of magnitude from $7 \times 10^{-6} \text{ g}$ to $7 \times 10^{-8} \text{ g}$ for a single measurement. This increase agrees with the expected theoretical improvements calculated using the atom interferometer sensitivity function and vibration spectra taken by an additional sensor.

The presented measurements, however, also show that cross-coupling from horizontal to vertical vibrations is present in the system. We found the accelerometer in the feedback loop to be the source for this cross-coupling. The sensor is currently being repaired by the manufacturer. Due to the long duration, however, no measurements can be presented in this work with the improved instrument.

In the future, the crosstalk between the vibration axes will be decreased. After eliminating the implementation error in the feedback design filter, it should be possible to

extend the feedback bandwidth on both the high and low frequency sides to values of 10 mHz and 60 Hz. If stability problems caused by the tilt-pad in the vibration isolator and by an internal mechanical resonance of the feedback sensor can be solved, this bandwidth could be increased even beyond that.

The system will then provide similar isolation to other high-performance low-frequency vibration isolators like the one discussed in [HPCI99]. This system currently provides higher performance due to the slightly lower resonance frequency of about 0.01 Hz and assumable reduced cross-coupling. Major advantages of the system presented here are that the same potential performance is provided in a small transportable package. Additionally, transient responses are much less of a problem in our system which greatly increases the usability of the system.

Chapter 4

Detection System Development

As pointed out in chapter 2, the phase shift $\Delta\phi$ of the interferometer is determined by the number of the atoms in the upper fine structure after the interferometer sequence. This is stated by the formula 2.11:

$$P_{|2\rangle} = \frac{1}{2}(1 + \cos \Delta\phi)$$

The detection system, which measures $P_{|2\rangle}$, is an important subsystem of the interferometer as measurement noise directly introduces noise in the interferometer signal. This potentially lowers the sensitivity in measuring g . Since the atomic states are projected from a superposition state onto a single state during detection, the accuracy of the detection is limited by the quantum mechanical uncertainty of this projection. The goal in designing a good detection system is to keep other technical noise sources small enough so that the measurement is limited by the quantum mechanical projection noise.

This chapter will give an overview over two different detection schemes, fluorescence and absorption detection. The benefits and shortcomings of these two principles will be described briefly. Various noise sources which have to be considered to design a high sensitivity detection system will be discussed. A new absorption detection system which overcomes several traditional limitations will then be introduced. An optical setup implementing this approach on our atom interferometer has been designed during this work and will then be presented.

4.1 Overview of common Detection Schemes

The basic idea of all common detection schemes is to illuminate the atom sample to be detected with a laser beam driving an atomic transition. The atoms absorb light from the laser beam and emit light caused by spontaneous emission. Fluorescence detection is based on measuring the intensity of the emitted light, absorption detection on measuring how much intensity is missing in the detection beam due to absorption.

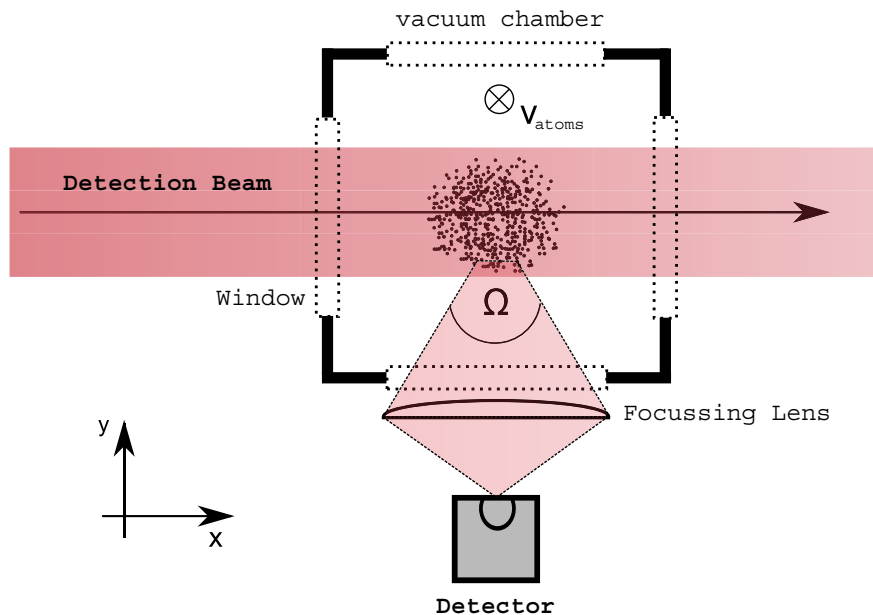


Figure 4.1: Principle of fluorescence detection. By courtesy of S. Grede

Our current atom interferometer setup uses a fluorescence detection scheme which is illustrated in figure 4.1. As described in section 2.2 on page 10, the detection happens after the interferometer sequence when the atoms are on their way back down to the MOT chamber.

At the time of detection the atoms are moving downwards perpendicularly to the plane of projection in the drawing. A detection laser beam is then switched on and illuminates the atoms from the window on the left, driving the ^{87}Rb D2 transition from $F = 1$ to $F = 2$. A detector is situated perpendicular to the laser beam and is carefully screened off so that practically no light reaches the detector directly. It then measures only the isotropically emitted fluorescent light of the atoms. The number of emitted photons is directly proportional to the number of atoms.

Several limitations to this scheme exist. Due to geometrical limitations of the vacuum chamber in most atomic fountain experiments, only light from a small solid angle around the atoms can be focused on the detector. This ratio is typically in the range of 0.25% to 1%. The measured signal level is therefore a priori attenuated by about 40 dB which causes problems due to low signal levels.

One atom emits about 2.5 fW of light when driven with saturation intensity on the described transition. With about 10^6 atoms being detected, a very small optical power in the order of Picowatts results. Detecting this is practically unachievable with usual photo diodes. Instead avalanche photo diodes or photo multiplier tubes, PMTs, have to be used. These devices create secondary electrons from photo electrons to amplify the

signal. Due to their high amplification, they are subject to a variety of nonlinear effects such as temperature dependent amplification factors, hysteresis effects etc. These limit the signal-to-noise ratio of the measurements.

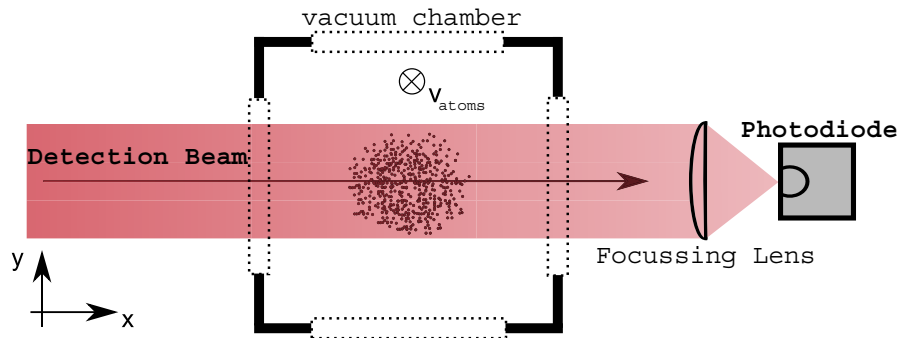


Figure 4.2: Principle of absorption detection. By courtesy of S. Grede

Absorption detection is an alternative detection principle. Instead of measuring fluorescent light, one measures the number of atoms in $F = 2$ by monitoring how much light is taken out of the detection beam by absorption. The scheme is illustrated in figure 4.2. In this simple form, however, it is not a very sensitive detection method. The absorption signal is very small compared to other intensity modulations due to technical noise in the detection beam, also called excess laser noise. In this simple form absorption detection can not deliver the high performance required to enable quantum limited detection measurements. Several improvements of this principle exist which and make it possible to perform very accurate measurements. They will be thoroughly discussed in section 4.3.

The next chapter will give a more complete discussion of the relevant noise sources which have to be considered during detection measurements.

4.2 Detection Noise Sources

Noise inherent to the detection system limits the minimum optical power and therefore the minimum number of atoms which can be detected. It is therefore important to develop an understanding of the most important noise sources.

While some noise sources have technical causes like imperfect electronic or optical components, others have more fundamental sources. The most common noise sources to be discussed in this chapter are listed below:

- quantum projection noise
- photon shot noise of the laser

- excess noise in the laser caused by i.e. temperature fluctuations, input current instabilities or mechanical vibration of the laser cavity
- electronic noise introduced by the detector
- scattered light, e.g. from atoms in thermal background of the vacuum chamber or light reflected off the vacuum chamber walls.

4.2.1 Quantum Projection Noise

After the last interferometer pulse, the atomic wave functions are in a superposition of the lower and upper state used for interferometry:

$$|\Psi\rangle = a|1\rangle + b|2\rangle \quad (4.1)$$

Here $|1\rangle$ denotes the ground and $|2\rangle$ the excited state. We also have $|a|^2 + |b|^2 = 1$ due to the normalization of the wave function.

The fundamental laws of quantum mechanics state that the probability of finding an atom in state $|F=1\rangle$ is given by $|a|^2$, the probability of finding it in $|F=2\rangle$ by $|b|^2$. The outcome of the measurement is therefore uncertain due to the random projection onto one of the states. This results in a fluctuation of the atom numbers measured for each state and thereby induces measurement noise, usually called quantum projection noise or atomic shot noise. This was first experimentally confirmed by W.M.Itano [IBB⁺93]. He also shows that for N atoms in a thermal cloud with the same state, the variance due to the projection noise is given by:

$$\sigma_{atom}^2 = N|a|^2|b|^2 \quad (4.2)$$

The standard deviation of the measurement is hence proportional to $\propto \sqrt{N}$.

The projection noise is a fundamental limit to the sensitivity of the atom interferometer. The goal of the detection system is therefore to be limited by quantum projection noise. Note that it would be possible to push the sensitivity beyond this point by using entangled atoms or squeezed states. Up to this point this has not been an issue, however, as other noise sources limit the sensitivity of the interferometer.

4.2.2 Laser Noise

An ideal laser in single-mode operation creates a coherent light field corresponding to a plane wave:

$$\vec{E}(\vec{r}, t) = \vec{E}_0 \sin(\vec{k} \cdot \vec{r} - \omega t + \phi) \quad (4.3)$$

with an intensity $I \propto |\vec{E}_0|^2$, which shall be constant during the detection. When counting the photons in the light field with a detector, the probability of measuring n photons

within a certain period is given by a Poisson distribution:

$$P(n) = \frac{\bar{n}^n}{n!} e^{-\bar{n}} \quad (4.4)$$

with \bar{n} being the average number of photons. The variance of the probability distribution 4.4 is given by

$$\sigma_n^2 = \bar{n} \quad (4.5)$$

The standard deviation of the number of photons counted on a detector within a certain period is therefore proportional to $\sqrt{\bar{n}}$. Since the variance is constant and does not depend on the frequency, the resulting noise spectrum will be flat in the frequency domain. This is also called white noise. The above described noise due to the Poisson statistics is often referred to as photon shot noise in the literature. The flat part in the spectrum, shown in figure 4.3, is a good example of its appearance in a measurement. Figure 4.3

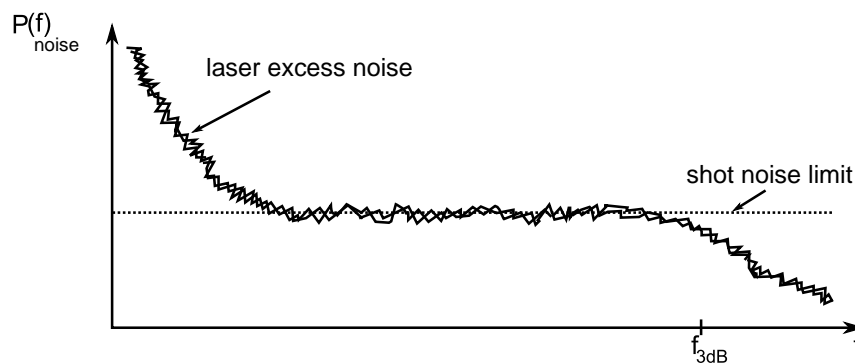


Figure 4.3: Typical noise spectrum of a real world laser.

shows the noise spectrum of a real laser with significantly increased noise levels at low frequencies. This additional low frequency noise is often denoted as laser excess noise σ_{exc} and can be caused by many sources such as mechanical vibrations of the laser cavities or power supply instabilities. Towards higher frequencies the noise level decreases and reaches the shot noise limit at a frequencies of typically several kilohertz. At the edge of the measurement bandwidth the signal then decreases below the shot noise limit due to the decreasing detector response.

When performing absorption detection, the laser excess and shot noise needs to be kept below the quantum projection noise caused by the atoms to keep it from limiting the performance of the detection system:

$$\sigma_{atoms} > \sigma_n + \sigma_{exc}$$

4.3 Double-Beam Absorption Spectroscopy

Traditional absorption spectroscopy systems are usually limited by laser excess noise in the detection beam which effectively introduces an intensity modulation of the beam. This can not be distinguished from the atomic absorption signal. A simple absorption detector is therefore typically incapable of performing a projection noise limited measurement without additional measures to alleviate the excess noise.

Several approaches exist to improve this situation. The first is to lower the laser excess noise below the photon shot noise limit by implementing a feedback loop to control the laser source current. Due to the nonlinear system response of the laser to a changing input current, however, this is difficult to implement. Additionally, the high cancellation required for reaching the photon shot noise can usually only be realized for a very narrow bandwidth.

An alternative approach is to modulate the frequency of the laser signal in order to perform the detection measurement at higher frequencies where laser excess noise becomes negligible. A drawback of this approach is that frequency modulations are translated to amplitude modulation by some optical elements. This effect is also called etalon effect and is caused by optical cavities between elements with parallel optical surfaces. These etalon effects can be large compared to the measured signal, and make it unfeasible to reach the photon shot-noise limit.

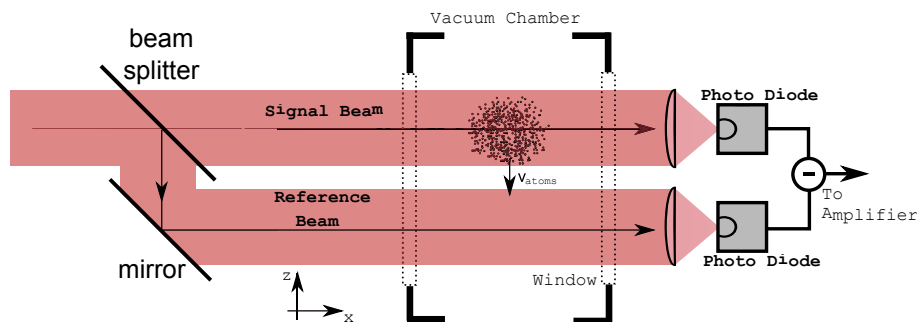


Figure 4.4: Principle of double-beam absorption detection.

A third approach reducing laser excess noise is to perform a differential measurement by using two detection beams to subtract the excess noise from the measured signal. The principle of the measurement is shown in figure 4.4. The detection beam coming from the laser is split by a 50/50 beam splitter into a signal and a reference beam. The signal beam traverses the detection zone and gets partially absorbed by the atom sample before being detected. The reference beam follows a similar path but is not subject to absorption before being detected. By subtracting the photo current of the two photo-diodes, the expected resulting current is close to zero. The large signal background is therefore removed from the measurement which is beneficial for detecting weak absorption signals. Additionally,

the excess noise of the laser can be removed from the signal since it effectively acts as an intensity modulation and is the same in both beams. Note, however, that this is not the case for the photon shot noise. The beam-sampler distributes the photons randomly between both beam paths, making the photon shot noise is uncorrelated and impossible to cancel out.

One problem with this method is that the intensity between both beams has to be balanced very carefully to achieve an effective cancellation. As calculated in [Gre09], the detection laser used in our setup needs a cancellation performance of -50 dB to reach the photon shot noise limit. To achieve this performance by subtracting the photo current of both beams, the intensity has to match within a 0.03% margin, which is impractical. The cancellation performance using this simple method is therefore limited to approximately 20 dB in real world measurements [HH91].

An improved detector introduced in [HH91] and [Hob97] alleviates the beam-balancing problems and achieves a cancellation performance of up to 65 dB. It works by internally adjusting the balance between the two photo currents with an internal feedback loop before subtraction. All deviations between the two beams are therefore canceled out within the bandwidth of this feedback loop which extends up to frequencies where excess noise becomes negligible.

Such a noise-canceling detector was built and characterized in another recently carried out work [Gre09]. Measurements in a test setup confirm that the detector is indeed limited by quantum projection noise within a certain range of measurement parameters. The detection system designed in this work is based on this detector. It will therefore be discussed in great detail in the following section.

4.4 Predicted Performance of the Noise-canceling Absorption Detector

The performance of an absorption measurement with the detector described in [Gre09] depends on numerous system parameters, including the detection beam intensity, the number of atoms to be detected and the detection time.

In order to estimate the expected atom projection and detection noise, we introduce the signal-to-noise ratio (SNR):

$$SNR = \frac{P_{signal}}{P_{noise}} \quad (4.6)$$

with the noise power P_{noise} and the signal power P_{signal} . We will now deduce the signal-to-noise ratio resulting quantum projection noise and the SNR introduced by the detection system in the absorption measurement.

We define the power absorbed from the detection beam by the atoms as P_a . The power absorbed by each atom is then given by P_a/N . As deduced in section 4.2.1, the deviation in

determining the atom number from the quantum projection error is given by $\sigma_{quant} = \sqrt{N}$. The resulting noise power is then given by $\frac{P_a}{N}\sqrt{N}$. The resulting signal-to-noise ratio will be denoted as SNR_{quant} and is given by:

$$SNR_{quant} = \frac{P_a}{P_a/\sqrt{N}} = \sqrt{N} \quad (4.7)$$

Since the noise-canceling detector effectively eliminates the laser excess noise, the signal-to-noise ratio of the detector alone is limited by photon shot noise. Note, however, that two laser beams are detected and contribute to the measured signal, which effectively doubles the shot noise in amplitude. The signal-to-noise ratio of the absorption measurement heavily depends on the detection beam intensity, the atom number and the measurement time over which the signal is integrated. In only a limited range of these parameters can quantum noise limited absorption detection be realized.

A brief assessment of these parameters will be carried out. We will assume, that laser shot noise is the only noise left in the detected signal and that additional excess noise has been canceled out by the detector.

The size of the detected signal depends on the optical power absorbed by the atoms which in turn depends on the intensity of the detection beam. As the intensity increases, the atoms will absorb more photons until a saturation takes place. The maximum absorption rate is given in the limit of infinitely large intensity where the the atoms are excited exactly half of the time. With increasing intensity, however, the photon shot noise also increases. We therefore expect a maximum at a signal-to-noise ratio of the detector at a certain intensity. As shown in [Gre09], this maximum is given by the saturation intensity of the atomic transition:

$$I_{sat} = \frac{\hbar\omega^3\gamma}{12\pi c^2} \quad (4.8)$$

with the spontaneous emission rate γ and the transition frequency ω .

Other parameters influencing the signal-to-noise ratio are the atom number and the measurement time over which the signal is integrated. A detailed simulation of signal-to-noise ratio of the detector has been performed in [Gre09]. The result is shown in figure 4.5 which shows the SNR_{quant} and the SNR of the detector for a set of measurement times t_m plotted versus the atom number. The projection noise limit is reached in a measurement when SNR_{quant} is lower than the SNR of the detector and crosses the respective line in the plot. For 10^6 atoms the minimum detection time is given by $t_m = 100\mu\text{s}$ whereas 10^5 atoms already need an integration time of $t_m = 2\text{ms}$ to reach this threshold. The red line in the plot corresponds to a measurement time of 2 ms and represents an improved version of the detector. This version reduces the increased shot noise introduced by the second laser beam [Gre09] and reaches the projection noise limit faster.

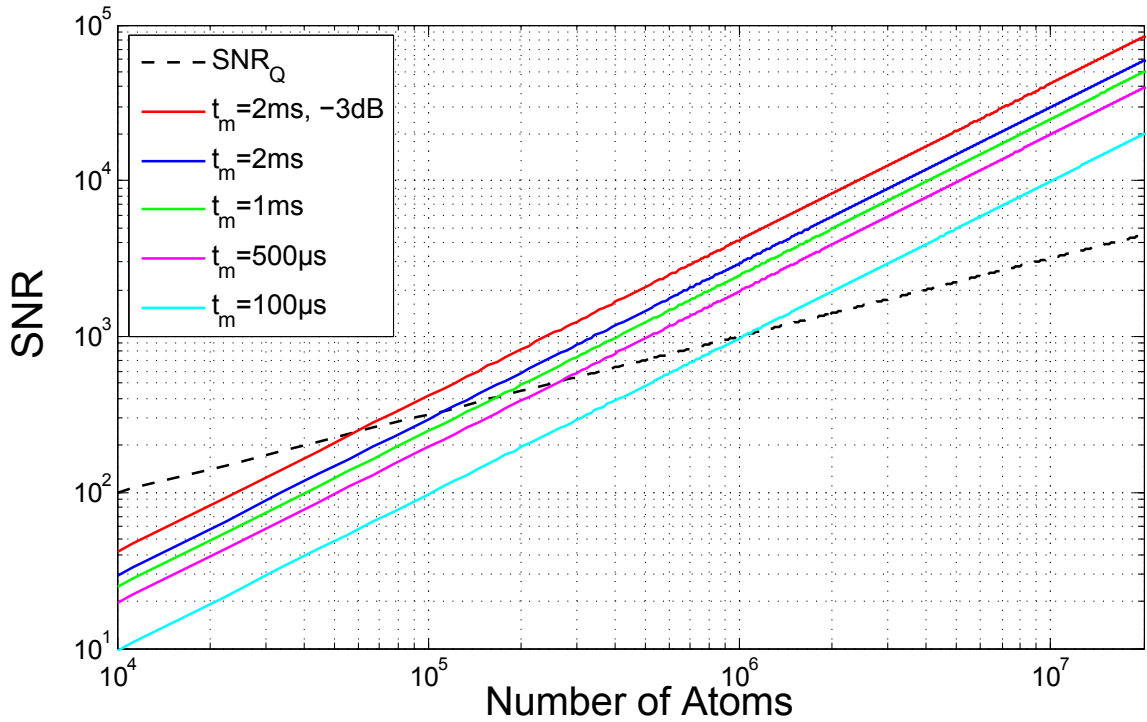


Figure 4.5: Signal to noise ratio of the balanced absorption detector versus the atom number to be detected. The colors represent different detection times, the intensity is assumed to be the saturation intensity. From [Gre09].

Since the atom number is determined by the atom interferometer, the detection system has to be designed in order to allow a for along enough detection time to reach the quantum projection noise limit.

4.5 Implementation of the Balanced Absorption Detector System

During the design process of the new absorption detection system for the atom interferometer, several limitations of the detector and the geometrical limitations of the vacuum chamber had to be taken into account. As short assessment of the resulting design decisions will be carried out here.

When performing a measurement with the balanced absorption detector presented in [Gre09], the absorption signal has to be detected at a frequency outside of the detector bandwidth in order to keep the feedback loop from canceling out the desired signal. In order to achieve this, the laser frequency is modulated during measurements and results in an amplitude modulation of the absorption signal from the laser being tuned in and out of the atomic line-width. Experiences from the test setup shown in [Gre09] made clear, however, that this frequency modulation induces an amplitude modulation caused

by etalon effects also described in 4.3. This significantly decreased the noise cancellation performance of the detector.

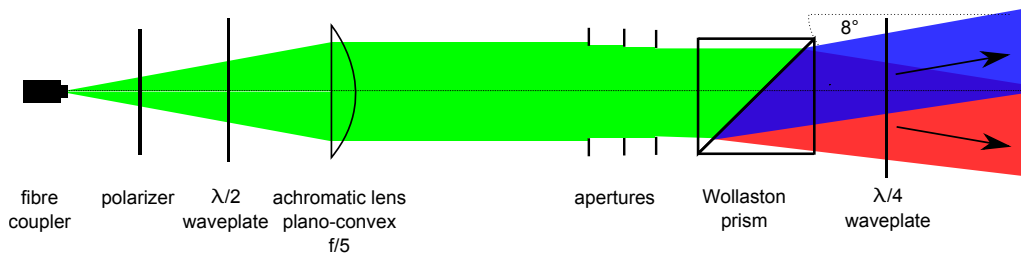


Figure 4.6: Beam collimation and separation using a Wollaston prism to avoid etalon effects

In order to avoid etalon effects in the detection system for the atom interferometer, parallel optical surfaces and normal incidents therefore had to be avoided in the optical design process. Since the windows of the vacuum chamber are such a parallel optical surface, we chose a tilted beam geometry to avoid normal incidence. The light traverses the vacuum chamber on an angle of 5° as shown in figure 4.7 and 4.10. This leaves a diamond shaped overlap region shown in figure 4.9(c) in which the detection can be performed.

The angle of the detection beams furthermore results in a vertical component of the k -vector which does not cancel out. The atoms then receive a net momentum pointing upwards during detection. A schematic overview of the resulting geometry is shown in figure 4.7.

Another measure to reduce etalon effects is to avoid optical elements with parallel optical surfaces. Instead of a beam splitter cube, a Wollaston prism is used in the detection system to separate the signal and reference beams. Although Wollaston prisms have two parallel surfaces where the beam enters and leaves the prism, the outgoing beams have an angle of 5° to 10° degrees with respect to the surface normal. This is sufficient to suppress the etalon effects. All other optical components behind the Wollaston prism have been carefully placed to avoid parallel surfaces and normal incidence wherever possible. Figure 4.6 gives an overview of the beam collimation and separation optics.

4.6 Detection Sequence

We currently have $F = 2$ to $F' = 3$ light available for detection in our setup, compare figure 2.7. In order to determine the ratio of atoms in $F = 2$, the population in $F = 2$ and the total atom number is being measured. The population ratio is then given by:

$$P_{|2\rangle} = \frac{N_2}{N_{total}} \quad (4.9)$$

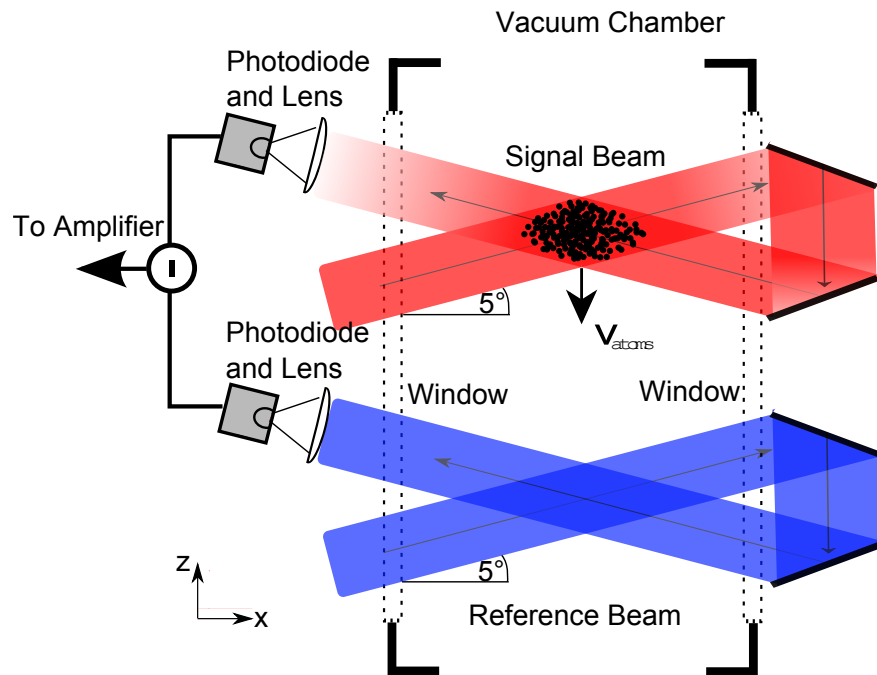


Figure 4.7: Modified double beam absorption detection setup to avoid etalon effects between the vacuum chamber windows. Note that in the real setup, the reference beams are placed on an orthogonal plane to save space, see figure 4.10

We first measure the number of atoms in $F = 1$. Afterwards the total atom number is determined by pumping the atoms in $F = 1$ to $F = 2$ by using MOT-repumper light and then doing another measurement.

As described in section 4.3, a net upward force acts on the atoms during detection by the new system. The size of net acceleration is about 6 km/s^2 and is derived in appendix A. The atoms enter the detection zone with an initial velocity of approximately 2 m/s . The acceleration due to the light force stops the atoms after approximately $300 \mu\text{s}$. If the detection beam is switched on for any longer they start moving upwards again and pass their initial position after $600 \mu\text{s}$. The detection time is therefore limited by the recoil force of the atoms

Since the signal-to noise ratio of the detected measurement increases with increasing measurement time, a compromise of a good signal-to-noise ratio and an acceptable recoil of the atoms has to be found. In a preliminary sequence designed for the new detection system we chose a detection time of 0.3 ms .

4.7 Description of the Optical and Mechanical Design

The optical and mechanical design was modeled using a computer aided design program. The program also supports basic geometric optics which was helpful to determine the

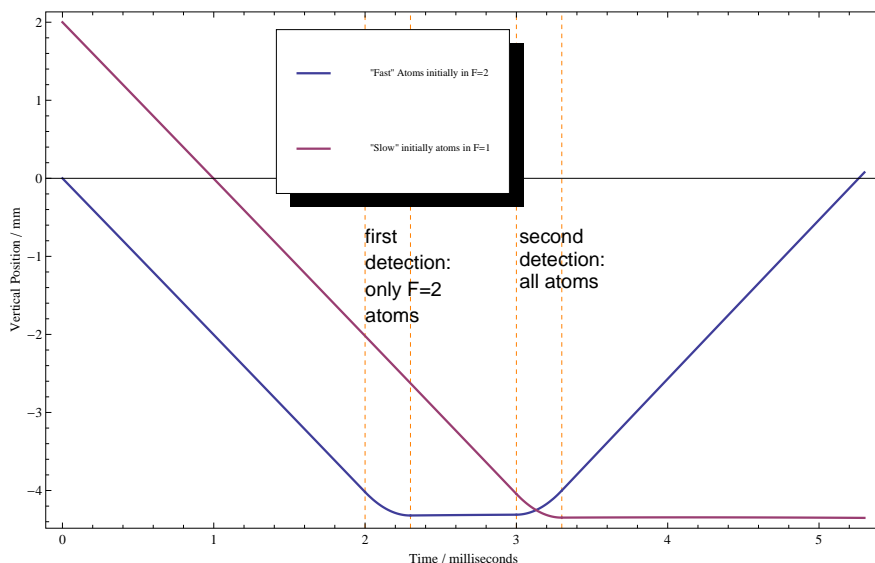


Figure 4.8: Space-time diagram of a preliminary detection sequence: The blue line represents the position of the first part of the atoms which arrives in $F = 2$ with an initial velocity of about 2 m/s. The atom number in this part is measured in the first 0.3 ms detection period which also gives the atoms a kick upwards and brings them to a halt. The second part of atoms in $F = 1$, displayed in red, is then transferred to $F = 2$ using the re-pumper. Once all atoms are inside the detection zone and in $F = 2$, a second 0.3 ms detection pulse measures the total number of atoms. This second detection gives the “fast” atoms another kick upwards with approx. 2 m/s. The slow atoms are simply stopped during the second detection sequence.

exact position and angle of the mirrors shaping the beam path. A rendered picture of the system is shown in figure 4.10.

4.7.1 General Remarks

The atom cloud contains between 4×10^4 and 10×10^6 atoms at the time of detection and has a $1/e$ size of about 30 mm in the xy-plane and a height of only 3 mm. Due to geometrical constraints set by the vacuum chamber and the restricted incident angles of the beams, the dimensions of the beam were chosen to be 13 mm times 6 mm. This only allows us to fit about 46% of the atoms into the detection beam. Despite losing half of the atoms, this actually creates a potential advantage for our gravimeter as the interferometer phase in the outer parts of the atom cloud are intrinsically more affected by rotations and Coriolis forces. By not detecting these atoms, we lower the effect of these systematic effects on our measurement. We chose circular polarization for the detection beams, despite the difficulties this induced regarding the preservation of the state during the course of multiple reflections. This drives the atoms into the magnetic sub-levels $|F = 2; m_F = 2 \rangle$ and $|F' = 3; m'_F = 3 \rangle$. By doing so we prevent them from decaying

into the $|F = 1\rangle$ state where they would be lost for the detection. The $F = 1$ ground state only has magnetic sub-levels with $|m_F| \leq 1$ which are not reachable via dipole transitions for atoms in the $|F' = 3; m'_F = 3\rangle$ excited state.

To alleviate polarization changes due to reflection, we use protected gold mirror throughout the system. All mirrors are mounted on stable miniature flexure mounts to ensure that the beam paths can be properly adjusted and remain stable.

4.7.2 Beam Paths

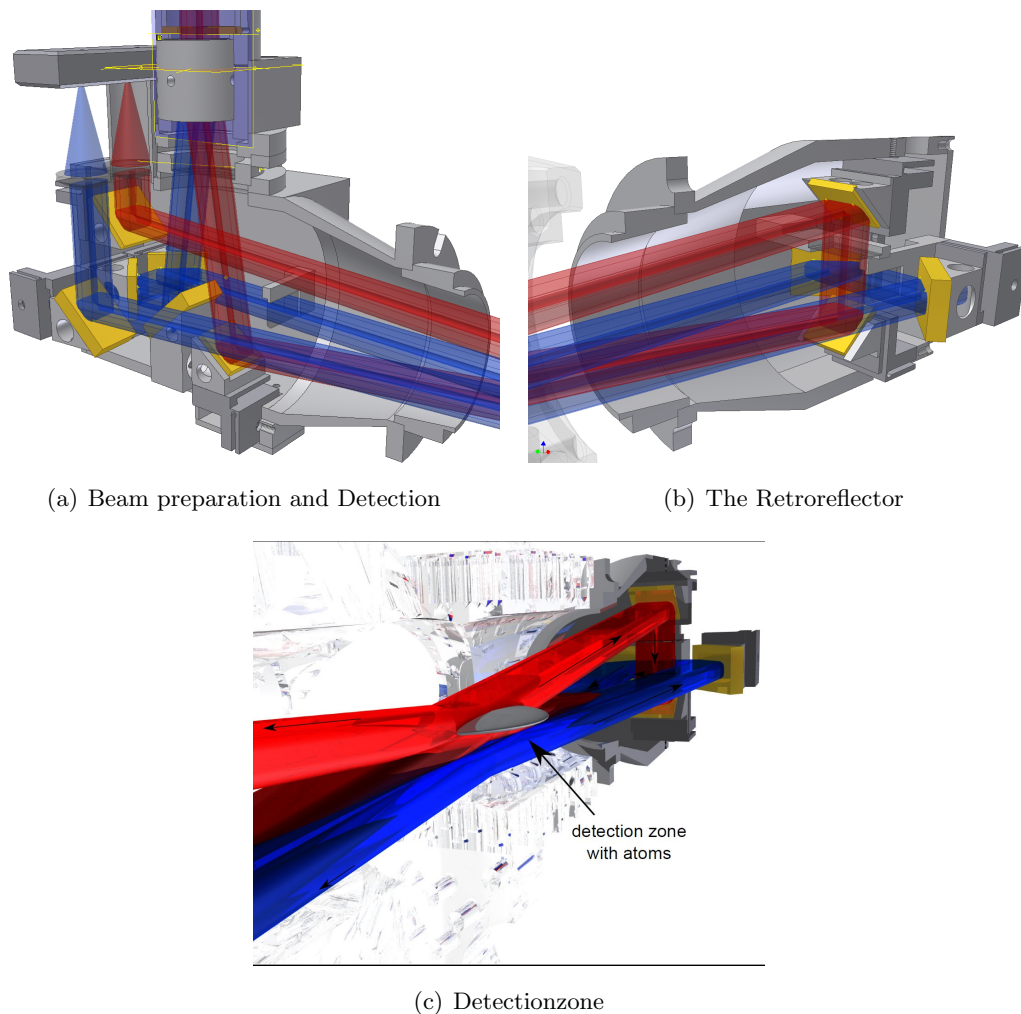


Figure 4.9: Detailed images of the detector optics, the retro-reflector and the detection zone. The black arrows depict the model beam directions. Red: signal beams; Blue: reference beam

The light enters the detection system behind a polarization-preserving single mode fiber. At first it passes a polarizer to ensure proper linear polarization and a rotatable $\lambda/2$ wave plate. This ensures a proper and adjustable linear polarization which serves

to adjust the intensity ratio between signal and reference beam later in the polarizing Wollaston prism. The diverging beam is then collimated using a single chromatic lens with a relative aperture of $f/4.8$. To ensure a similar intensity throughout the beam profile, only the middle of the beam with more than 20% of the maximum intensity is collimated. The beam is then stopped down to its intended size of 6 mm times 13 mm. This is done using three consecutive apertures to minimize diffraction. Behind the apertures, a Wollaston prism separates the beam into two beams according to its polarization. The intensity ratio between signal and reference beam can therefore be adjusted by the $\lambda/2$ wave-plate behind the fiber output. The two beams then pass a $\lambda/4$ wave-plate to get circularly polarized light.

The signal beam is then reflected into the vacuum chamber using a gold mirror. Its k-vector is entirely contained in the vertical xz-plane, the beam path can be seen in 4.10. After passing the detection zone the beam is focused on a photo-diode of the noise-canceling detector.

The reference beam is reflected onto a different path and passes the vacuum chamber on the horizontal plane, perpendicular to the signal beam. This plane is offset from the detection zone by about 1 cm in order to keep the reference beam from absorbing any atoms during detection. After retro-reflection and a second pass through the vacuum chamber it is focused on the second photo-diode of the detector.

The system has been set up on a test bench using a tube with the same optical length as the vacuum chamber. A picture is shown in figure 4.11

4.8 Conclusion and Outlook on the Detection System

This system provides a method for performing double-beam absorption detection of atoms in an atom interferometer setup by combining an optical setup that alleviates etalon effects and beam clipping with the sophisticated detector presented in [Gre09]. It therefore potentially provides a method for performing the atomic state detection in our atom interferometer setup limited by quantum projection noise. When using the optimum intensity for the signal beam, however, the net atomic recoil pointing upward limits the detection time to about 0.3 ms and somewhat reduces the detector efficiency. According to simulations carried out in [Gre09], this still allows us to perform projection noise limited detection for more than 6×10^5 atoms which is in the typical range for our setup. Internal improvements of the noise-canceling detector could further alleviate this problem by giving another 3 dB advantage in the detection noise which would lower the threshold atom number to approximately 3×10^5 [Gre09]. As an additional measure, the incident angle of the detection beams could be lowered from 5° to e.g. 2° . Despite possibly increasing the impact of etalon effects onto the measurement, this would reduce the net atomic recoil and

allow for a detection time of 0.8 ms. 9×10^4 atoms could then potentially be measured projection noise limited.

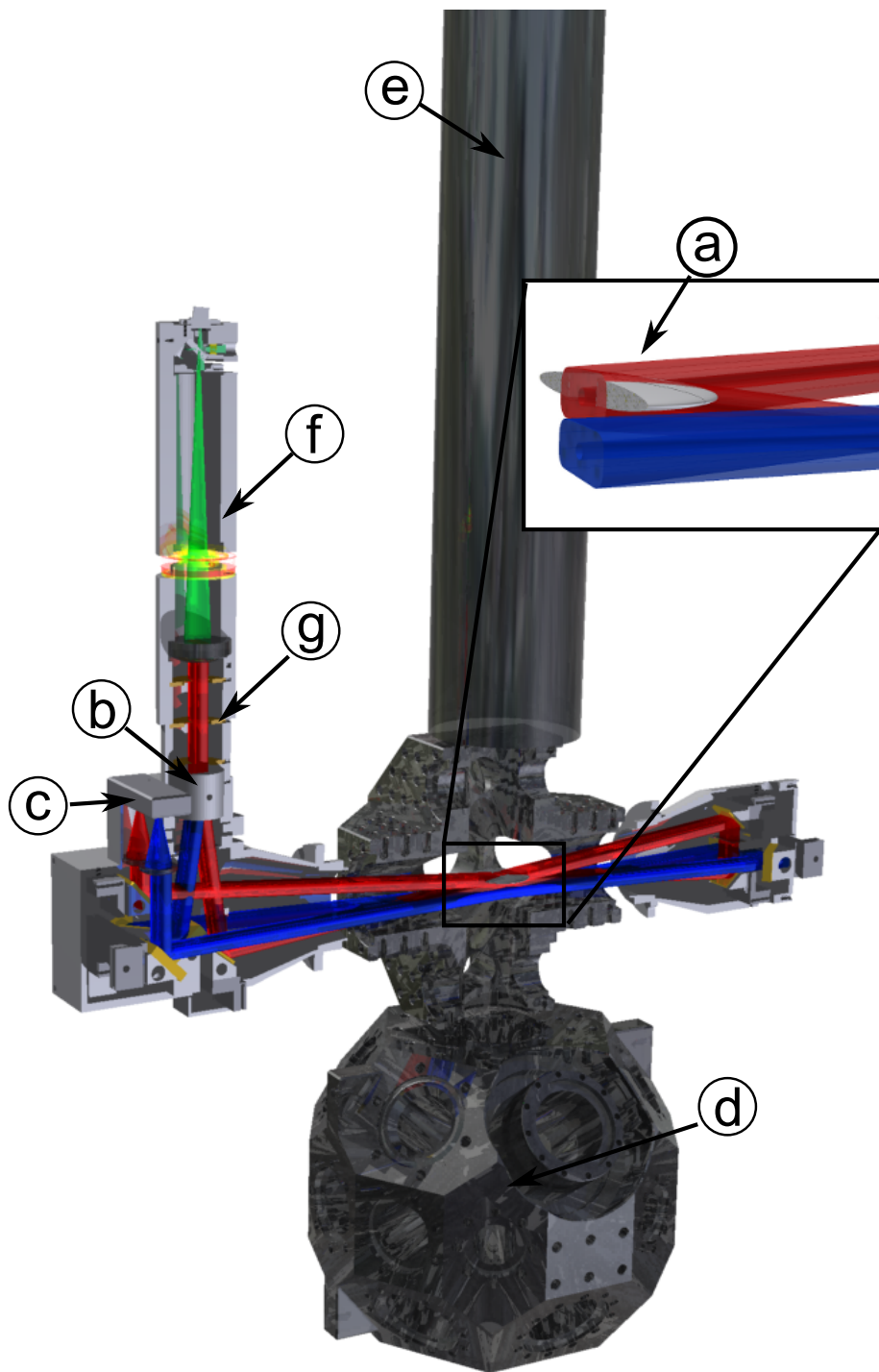


Figure 4.10: Sectional view of the completed double-beam absorption detector. The components shown are: a) the atom cloud on the way down in the vacuum chamber b) the Wollaston prism for separation into signal and reference beams c) the detector including 2 photo diodes and the electronics for common mode noise cancellation d) MOT chamber e) interferometer region f) beam collimator g) 3 aperture stops

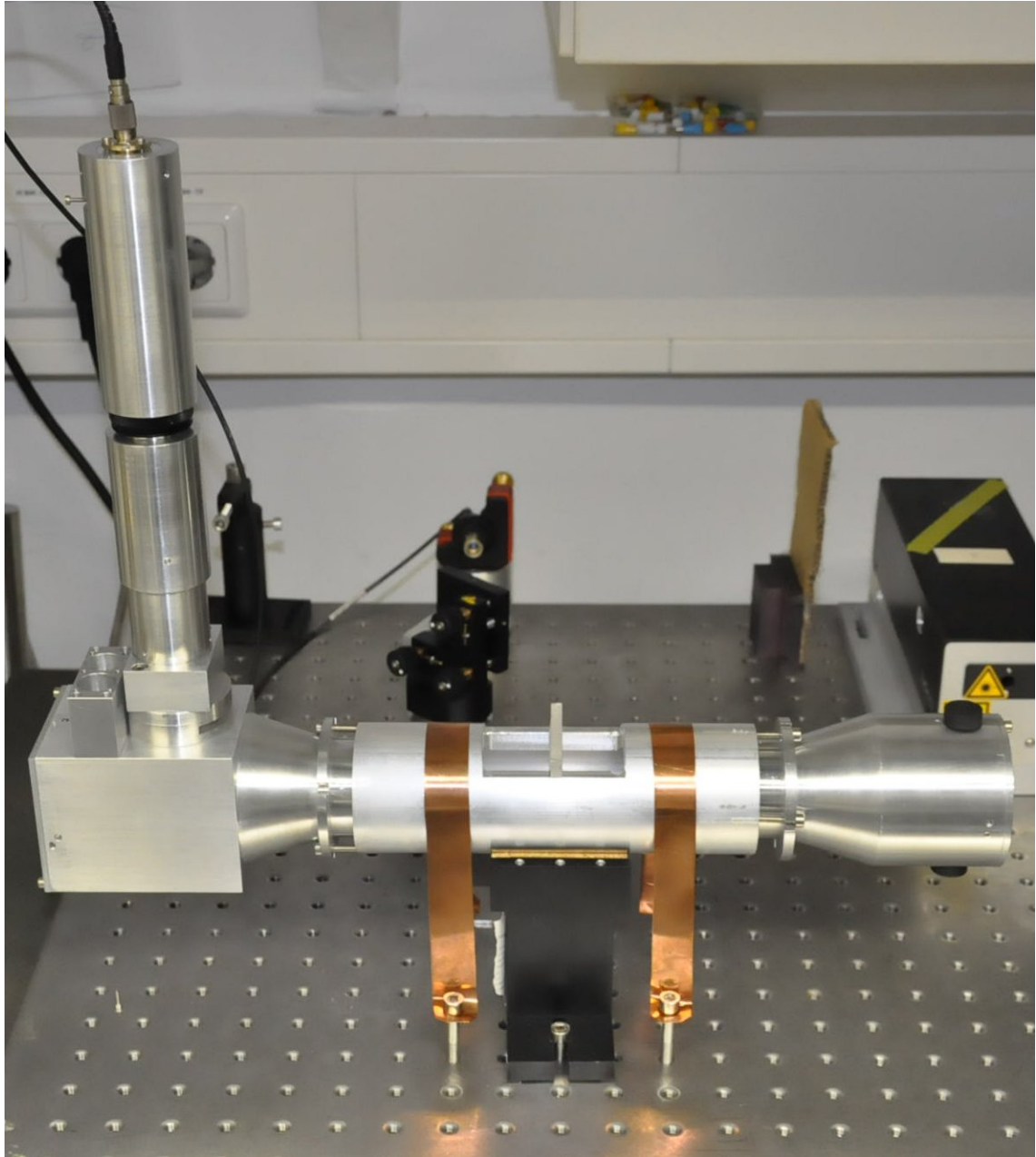


Figure 4.11: The absorption detection system designed during this work in a test setup.

Appendix A

Light Force

Due to the momentum recoil associated with photon absorption or emission, atoms acquire a net velocity when excited by light coming from a single direction. We will here derive how large the effective force on each atom is depending on the atomic transition and the light intensity. We will assume a plane wave with frequency ω and wave vector \vec{k} .

According to [Mes08] chapter 11.6, the resulting force on the atoms derived by the optical Bloch equations is given by:

$$\vec{F}^{light} = \hbar \vec{k} \frac{\gamma}{2} \frac{s_0}{1 + s_0 + (2\delta/\gamma)^2} \quad (\text{A.1})$$

Here s_0 is the intensity of the light field normalized to saturation intensity I_0 : $s_0 = I/I_0$. The detuning between the resonance frequency of the Bloch-oscillator ω_0 and the light frequency ω is given by $\delta = \omega - \omega_0$. The spontaneous emission rate of the atomic transition is given by γ . For small intensities the force increases linearly with s_0 and then saturates towards the saturation intensity $s_0 = 1$.

It was shown that the noise characteristics of the detection measurement is optimal if the atoms are illuminated with saturation intensity [Gre09]. Due to the detection scheme geometry with reflected beams, the beams pass the detection region twice and the detection intensity is twice as large as the beam intensity. We hence chose s_0 and $\gamma = 0$ for the detection beams. Due to the tilt α of the detection beams, the horizontal component of the light force cancels out between the incident and reflected detection beam. Only the vertical component given by $\sin \alpha$ exert a net force on the atoms.

Combining these parameters with equation A.1 yields the effective vertical acceleration of the atoms during detection by the constructed double-beam absorption detector:

$$a_z = \frac{F_z^{light}}{M_{atom}} = 2 \frac{\sin \alpha}{M_{atom}} \hbar k \frac{\gamma}{2} \frac{s_0}{s_0 + 1 + (2\delta/\gamma)^2} \quad (\text{A.2})$$

$$= \dots = 6791 m/s^2 \quad (\text{A.3})$$

Appendix B

Voltage Controlled Current Source

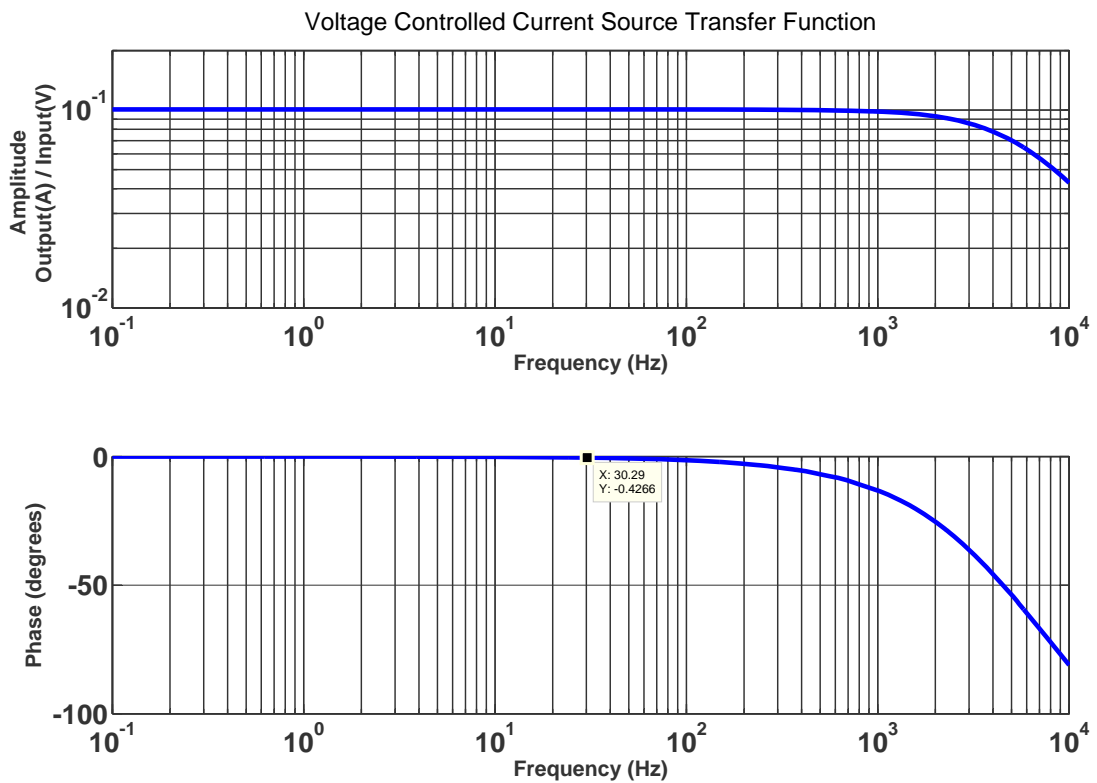


Figure B.1: Transfer function of the Voltage Controlled Current Source measured using a HP 3562A spectrum analyzer in sine-sweep mode

The voltage controlled current source driving the voice coil actuators was built in our electronics lab according to the circuitry shown in figure B.2. The central IC is a Burr-Brown OPA541 high power operational amplifier. It drives a current through the load on the output side which is proportional to the input voltage V_{in} . The load potential floats so neither of the load contacts can be connected to ground. The bandwidth reaches

Appendix C

Self Noise of the CMG3 Accelerometer

The self noise of the accelerometer potentially limits the performance of the active vibration isolation platform and is therefore of high interest. The following plot shows the specification of the Guralp CMG-3VL seismometer as specified by the manufacturer. The plot shows a double logarithmic plot of the power spectral density of the sensor self noise, the magnitude of various seismic events and various geological noise models.

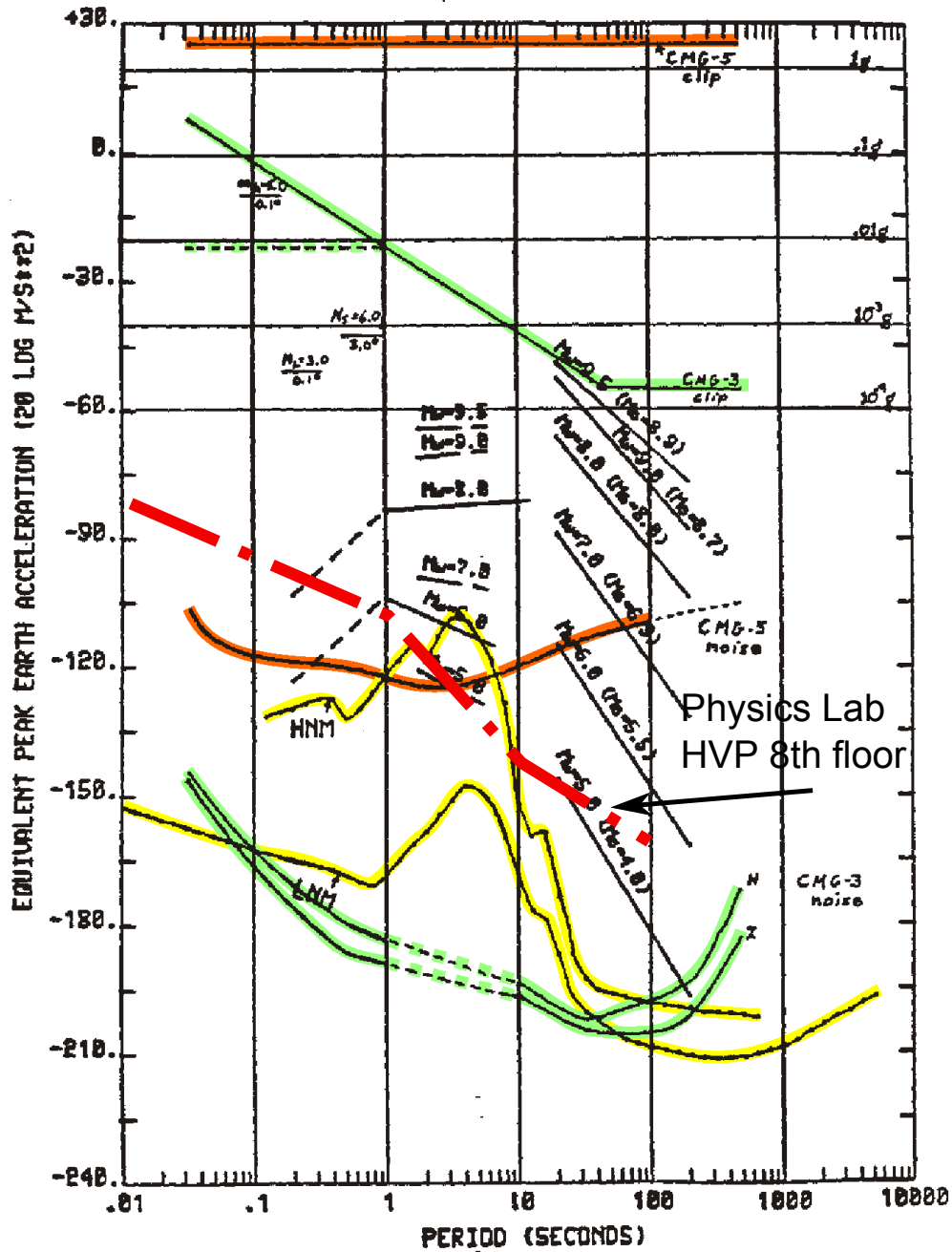


Figure C.1: Self noise of the Guralp CMG-3VL force feedback accelerometer. The green lines specify the noise and clip levels for our CMG3 accelerometer used for active vibration isolation. The yellow line specify vibration noise typically exhibited on seismological quiet and noisy sites, as specified in [Pet93]. The thick dashed red line shows the measured noise levels on the floor of our physics lab in central Berlin. The plot was taken from Guralp Limited Inc.

Bibliography

- [CCD⁺05] CHEINET, P ; CANUEL, B ; DOS SANTOS, F P. ; GAUGUET, A ; LEDUC, F ; LANDRAGIN, A: Measurement of the sensitivity function in time-domain atomic interferometer. In: *Arxiv* (2005)
- [DCQD91] D.W., Keith ; C.R., Ekstrom ; Q.A., Turchette ; D.E., Pritchard: An Interferometer for Atoms. In: *Physical Review Letters* 66 (1991), Nr. 21, S. 2693–2696
- [FFMK07] FIXLER, J B. ; FOSTER, G T. ; MCGUIRK, J M. ; KASEVICH, M A.: Atom interferometer measurement of the newtonian constant of gravity. In: *Science (New York, N.Y.)* 315 (2007), Januar, Nr. 5808, 74–77. <http://dx.doi.org/10.1126/science.1135459>. – DOI 10.1126/science.1135459. – ISSN 1095–9203
- [FPEN01] FRANKLIN, Gene F. ; POWELL, David J. ; EMAMI-NAEINI, Abbas: *Feedback Control of Dynamic Systems*. Upper Saddle River, NJ, USA : Prentice Hall PTR, 2001. – ISBN 0130323934
- [Gre09] GREDE, Sebastian: *Entwicklung und Charakterisierung von Teilkomponenten eines mobilen Atominterferometers*, Humboldt Universität zu Berlin, Diplomarbeit, 2009
- [HH91] HOBBS, Philip C D. ; HALLER, Kurt L.: Double beam laser absorption spectroscopy: shot-noise limited performance at baseband with a novel electronic noise canceller. In: B. L. FEAREY, Ed (Hrsg.) ; IBM Research Division, Thomas J Watson Research Center, P.O. Box 218, Yorktown Heights (Veranst.): *Optical Methods for Ultrasensitive Detection and Analysis: Techniques and Applications*. New York 10598 : Proc. SPIE 1435, 1991, S. 298–309
- [Hob97] HOBBS, Philip C D.: Ultrasensitive laser measurements without tears. In: *Applied Optics* 36 (1997), Nr. 4, S. 903–920

- [HPCI99] HENSLEY, Joel M. ; PETERS, Achim ; CHU, Steven ; INTRODUCTION, I: Active low frequency vertical vibration isolation. In: *Review of Scientific Instruments* 70 (1999), Nr. 6, S. 2735–2741
- [HSM⁺09] HERRMANN, S. ; SENGER, a. ; MÖHLE, K. ; NAGEL, M. ; KOVALCHUK, E. ; PETERS, a.: Rotating optical cavity experiment testing Lorentz invariance at the 10⁻¹⁷ level. In: *Physical Review D* 80 (2009), November, Nr. 10, 1–8. <http://dx.doi.org/10.1103/PhysRevD.80.105011>. – DOI 10.1103/PhysRevD.80.105011. – ISSN 1550–7998
- [IBB⁺93] ITANO, W. M. ; BERGQUIST, J.C. ; BOLLINGER, J.J. ; GILLIGAN, J.M. ; HEINZEN, D.J. ; MOORE, F. L. ; RAIZEN, M.G. ; WINELAND, D.J.: Quantum projection noise: Population fluctuations in two-level systems. In: *Physical Review A* 47 (1993), Nr. 5, S. 3554–3570
- [KC92] KASEVICH, M ; CHU, S: Measurement of the Gravitational Acceleration of an Atom with a Light-Pulse Atom Interferometer. In: *Applied Physics B* 54 (1992), S. 321–332
- [LMK⁺08] LE GOUËT, J. ; MEHLSTÄUBLER, T.E. ; KIM, J. ; MERLET, S. ; CLAIRON, A. ; LANDRAGIN, A. ; PEREIRA DOS SANTOS, F.: Limits to the sensitivity of a low noise compact atomic gravimeter. In: *Applied Physics B* 92 (2008), Nr. 2, 133–144. <http://dx.doi.org/10.1007/s00340-008-3088-1>. – DOI 10.1007/s00340-008-3088-1. – ISSN 0946–2171
- [Mah09] MAHADESWARASWAMY, Chetan: *Atom interferometric gravity gradiometer: Disturbance compensation and mobile gradiometry*, Stanford University, PhD, 2009. <http://proquest.umi.com/pqdlink?did=1836016281&Fmt=7&clientId=79356&RQT=309&VName=PQD>. – 133 S.
- [Mes08] MESCHÉDE, Dieter: *Optik, Licht und Laser*. 3., durchg. Vieweg+Teubner, 2008. – 568 S. – ISBN 978–3835101432
- [MGW⁺09] MÜLLER, T ; GILOWSKI, M ; WENDRICH, T ; ERTMER, W ; RASEL, E: A compact dual atom interferometer gyroscope based on laser-cooled rubidium. In: *Eur.Phys.J.D.* 53 (2009), S. 273–281
- [MPC10] MÜLLER, Holger ; PETERS, Achim ; CHU, Steven: A precision measurement of the gravitational redshift by the interference of matter waves. In: *Nature* 463 (2010), Februar, Nr. 7283, 926–9. <http://dx.doi.org/10.1038/nature08776>. – DOI 10.1038/nature08776. – ISSN 1476–4687
- [MWKC92] MOLÉ, K ; WEISS, D S. ; KASEVICH, M ; CHU, Steven: Theoretical Analysis of velocity-selective Raman transitions. 45 (1992), Nr. 1, S. 342

- [OJ91] O., Carnal ; J., Mlynek: Young's Double-Slit Experiment with Atoms: A Simple Atom Interferometer. In: *Physical Review Letters* 66 (1991), Nr. 21, S. 2689–2692
- [Pet93] PETERSON, Jon: *Observations and Modeling of Seismic Background Noise*. Albuquerque, New Mexico, 1993
- [Pet98] PETERS, Achim: *High Precision Gravity Measurements using Atom Interferometry*, Stanford University, Ph D, 1998. – 162 S.
- [Pet05] PETELSKI, Torsten: *Atom Interferometers for Precision Gravity Measurements*, European PhD School, Ph D, 2005. – 190 S.
- [Pla91] PLATUS, David L.: *Negative Stiffness Mechanism Vibration Isolation Systems*. 1991
- [Pla93] PLATUS, David L.: Smoothing Out Bad Vibes. In: *Machine Design* (1993), Nr. February 26, S. 123
- [PSWR07] PICARD, a. ; STOCK, M. ; WITT, T.J. ; REYMANN, D.: The BIPM Watt Balance. In: *IEEE Transactions on Instrumentation and Measurement* 56 (2007), April, Nr. 2, 538–542. <http://dx.doi.org/10.1109/TIM.2007.890783>. – DOI 10.1109/TIM.2007.890783. – ISSN 0018–9456
- [SCT94] STOREY, Pippa ; COHEN-TANNOUJJI, Claude: The Feynman path integral approach to atomic interferometry. A tutorial. In: *Journal of Physics II France* 4 (1994), Nr. November 1994, S. 1999–2027
- [SPG⁺10] SCHMIDT, Malte ; PREVEDELLI, Marco ; GIORGINI, Antonio ; TINO, Guglielmo M. ; PETERS, Achim: A portable laser system for high precision atom interferometry experiments. (2010), Juli, 7. <http://arxiv.org/abs/1007.0679>
- [Tor03] TORGE, Wolfgang: *Geodäsie*. 2. 10785 Berlin : Walter de Gruyter GmbH & Co. KG, 2003. – 370 S. – ISBN 3–11–017545–2
- [TW94] TIMMEN, L ; WENZEL, H G.: Worldwide synthetic gravity tide parameters. In: *Proceedings of Joint Meeting of the International Gravity Commission and the International Geoid Commission*, 1994, S. 92–101
- [WYC94] WEISS, D S. ; YOUNG, B C. ; CHU, Steven: Precision measurement of g / m Cs based on photon recoil using laser-cooled atoms and atomic interferometry. In: *Applied Physics B* 59 (1994), S. 217–253

- [ZJS05] ZAHNAN, K.H. ; JENTZSCH, G. ; SEEBER, G.: World-wide synthetic tide parameters for gravity and vertical and horizontal displacements. In: *Journal of Geodesy* 79 (2005), August, Nr. 6-7, 293–299. <http://dx.doi.org/10.1007/s00190-005-0460-3>. – DOI 10.1007/s00190-005-0460-3. – ISSN 0949–7714

Danksagung/Thanks

Als erstes möchte ich mich bei Professor Achim Peters dafür bedanken, dass er mir ermöglicht hat meine Diplomarbeit extern an der Humboldt Universität zu Berlin anzufertigen. Danke auch für die vielen guten Ratschläge und Ideen im Labor. Diese lehrreichen Aussagen und die resultierenden Diskussionen haben das Zustandekommen der Arbeit wesentlich mit beeinflusst.

Weiterhin möchte ich mich bei Professor Möller herzlich dafür bedanken, dass er sich unbürokratisch als Erstgutachter an der TU-Berlin zur Verfügung gestellt hat und damit die Durchführung dieser Diplomarbeit ermöglicht hat.

Mein spezieller Dank gilt auch Alexander Senger für die gute Betreuung während der Diplomarbeit und die vielen anregenden Diskussionen und Ratschläge von denen ich viel gelernt habe. Nicht zuletzt möchte ich ihm ganz herzlich für das schnelle und gründliche Korrekturlesen während der Schreibphase danken.

Danke an Malte Schmidt, Sebastian Grede und Matthias Hauth für die angenehme Arbeitsatmosphäre und die sehr gute Zusammenarbeit am GAIN Atominterferometer.

Evgeny Kovalchuk möchte ich für die Diskussionen über Vibrationsspektren und den endlosen Vorrat an Erfahrungen in allen möglichen Fragen der Physik danken.

Auch allen anderen QOMs und NANOs sei ein herzlicher Dank für die gute Zusammenarbeit ausgesprochen. Dies gilt insbesondere für Matthias Schoch für die schnelle und gute Arbeit im Elektroniklabor und für alle Büronachbarn, die wesentlich zum Spass an der Arbeit beigetragen haben.

Ein grosses special thank you geht an Trista, die die lange Phase meiner Diplomarbeit begleitete und immer die richtigen Worte fand um mir dabei zu helfen. Danke ausserdem für die guten Tips bezüglich der englischen Sprache. Meine Familie und insbesondere meine Eltern haben mein Studium und die abschliessende Diplomarbeit erst möglich gemacht. Vielen Dank für die immerdauernde Unterstützung.